A study of neutron pairing correlations using the ^{136}Ba(p, t) reaction

Jespere Calderone Nzobadila Ondze

UNIVERSITY *of the*
WESTERN CAPE

A thesis submitted in fulfillment of the requirements for the degree of Master of Sciences in Physics, Department of Physics and Astronomy, Faculty of Natural Sciences, University of the Western Cape

2019

To My parents

Declaration

I, Jespere Calderone Nzobadila Ondze, declare that a study of neutron pairing correlations using the ^{136}Ba(p,t) reaction is my own work and I confirm that this work has never been submitted for a degree or any other qualification at this university or any other institution. Where I have quoted from the work of others, the source is always given and I have acknowledged all main sources of help.

Signed by Jespere Calderone Nzobadila Ondze

Date: November 2019

Acknowledgements

As this work is a collective effort rather than individual, I would like to express my thanks to everyone who contributed so that this work be completed. First of all and foremost, I would like to express my biggest gratitude to my supervisor Professor Smarajit Triambak. Thank you for giving me a wonderful opportunity to work under this exciting project. Your expertise and immense knowledge helped me to successfully complete this assignment.

I am highly grateful and indebted to my respected co-supervisor Doctor Bernadette Maria Rebeiro for her excellent guidance and infinite assistance throughout this work. Bernadette you sacrificed your valuable time as a PhD student to look over my entire analysis, providing me with excellent techniques and suggestions. You gave me a necessary kick when things got tough, without you it wouldn't be the same. I really cannot thank you enough.

I would like also to thank Professor Robbie Lindsay for giving me such a great privilege to join the MANUS program and pursue my post-graduate studies at the University of of the Western Cape.

I cannot forget to thank my group mates, Justice Mukhwewho, Mohamed Kamil, Bhivek Singh, and Craig Vyfers with whom I have spent most of the time at the department. Thank you guys for your company.

I am thankful to the National Research Foundation (NRF) for financial support and the administrative staff of the Physics department at the University of the Western Cape.

I cannot terminate these lines of gratitude without thanking my family

(namely my parents, Simon Nzobadila and Ondze Marie Nicole, and my brothers, Espoir Keigerlain Nzobadila, Darius Rolick Nzobadila Ondze, Yoane Elvyr Nzobadila Ondze and Eden Mardoli Nzobadila Ondze) who have always showed their sincere love to me throughout my life.

I reserve a special place to Arden Simplicité Bissila “Le Patrimoine” for his friendship, and daily encouragements since my early days in Cape Town.

Finally, my truthful thanks to my fiancée Ilariat Joella Kokele Otonamoki for being a great source of support and encouragement to complete this work.

Abstract

Observation of neutrinoless double beta decay ($0\nu\beta\beta$) is currently the only means by which one could establish the Majorana nature of neutrinos. Additionally, such an observation would determine the absolute neutrino mass scale. However, this requires that the matrix element for a given $0\nu\beta\beta$ decay process is accurately calculated. The objective of this project is to provide useful nuclear structure information that aim to improve future theoretical calculations for the nuclear matrix element (NME) of ^{136}Xe $0\nu\beta\beta$ decay to ^{136}Ba. We studied neutron pairing correlations in ^{134}Ba using the ^{136}Ba(p,t) reaction to stringently test the Bardeen-Cooper-Schrieffer (BCS) approximation in the $A = 136$ mass region. This is because many theoretical calculations of the NME's for $0\nu\beta\beta$ decay are performed using the quasiparticle random phase approximation (QRPA), which uses the BCS approximation to describe the ground states of the even-even parent and daughter nuclei. Our results show a significant fragmentation of the neutron-pair transfer to excited 0^+ states, implying a breakdown of the BCS approximation in this mass region.

Contents

1 Introduction 2

1.1 Standard Model of Particle Physics 2

1.2 A brief history 4

1.3 Lepton number conservation 5

1.4 Parity violation in weak interactions 7

1.5 Massive neutrinos and $0\nu\beta\beta$ decays 12

1.5.1 Double beta decays in atomic nuclei 14

1.5.2 $0\nu\beta\beta$ Nuclear Matrix Elements 16

1.5.3 Current experimental status of ^{136}Xe$\longrightarrow$^{136}Ba $0\nu2\beta$ decay 24

2 Direct nuclear reactions 29

2.1 Scattering Theory 31

2.1.1 Differential Cross Section 31

2.1.2 Quantum mechanical theory of scattering 32

2.1.3 Elastic Scattering 35

2.2 The Distorted-Wave Born Approximation 37

2.3 Optical Model Potential 38

2.4 Two-Body Nuclear Reaction Kinematics 40
2.5 Two-nucleon transfer reactions 45

3 Experimental Setup and Data Analysis 48
3.1 Experimental Setup 48
3.1.1 Facility 48
3.1.2 Ion source 49
3.1.3 Tandem Van de Graff accelearator 50
3.1.4 Q3D Magnetic Spectrograph 52
3.1.5 Focal plane detector 53
3.2 Data Analysis 55
3.2.1 Particle identification 55
3.2.2 Peak fitting 55
3.2.3 Energy calibration 56
3.2.4 Uncertainties in excitation energy calculations 57
3.2.5 Cross section determination 58
3.2.6 Laboratory to centre-of-mass (CM) frame transformations 59
3.2.7 Elastic scattering 61
3.2.8 Beam particles 65
3.2.9 Dead time corrections 65
3.2.10 Solid angle determination 66
3.2.11 Uncertainties in Cross Section 67
3.3 DWBA calculation 68

4 Results and Conclusions 71

4.1 Results and discussion 71

4.1.1 Excitation energy levels in ^{134}Ba 72

4.1.2 Spin-parity assignments 75

4.1.3 Implications for neutron pairing correlations 86

4.2 Conclusions 88

A DWUCK4 code 90

A.1 General description of DWUCK4 90

A.2 DWUCK4 input file 91

B ^{136}Ba$(p, t)^{134}$Ba Angular distributions 96

List of Figures

1.1 Classification of elementary particles and their interactions according to the standard model. Figure taken from Ref.[2]. . 3

1.2 Energy distribution of electrons and positrons observed during beta decays. Figure taken from Ref. [4]. 4

1.3 Observed electron angular distributions when the nucleus is polarized along positive z-axis (left side), and when the nucleus is polarized in the negative z-axis (right side). Figure taken from Ref. [10] 10

1.4 Schematic representation of Goldhaber *et al.* experiment. . . 11

1.5 Mass parabola for A = 136 isobars. Although ^{136}Xe cannot β decay to ^{136}Cs, $\beta\beta$ decays to ^{136}Ba are allowed. Figure taken from Ref [17]. 14

1.6 Left panel: $2\nu\beta\beta$ decay. Right panel: $0\nu\beta\beta$ decay. 15

1.7 Calculated NMEs for several $0\nu\beta\beta$ decay candidates using different theoretical approaches. Figure taken from Ref [23]. . 17

1.8 Single-particle shell model potentials. Figure taken from Ref. [25]. 19

1.9 Single-particle levels obtained with the harmonic oscillator potential (HO), Woods-Saxon potential (WS) and Woods-Saxon plus spin-orbit coupling (WS+LS). Figure taken from Ref [26]. 22

1.10 Comparison of the expected signals for $0\nu\beta\beta$ and $2\nu\beta\beta$ decays, as shown in Ref. [37] 26

1.11 Schematic view of the EXO-200 detector. Figure taken from Ref. [38]. 27

1.12 Schematic of the kamLAND-ZEN detector. Figure taken from Ref. [39]. 28

2.1 Scattering of a beam of particles into a solid angle Ω. 32

2.2 A graphic representation of two-body kinematics for the reaction ^{136}Ba(p, t) in the laboratory coordinate system (left side) and the center-of-mass coordinate sytem (right side). 41

3.1 A photograph of the tandem hall at MLL, showing the tandem Van de Graaff accelerator (orange) and the 90° analyzing magnet (blue). 49

3.2 Scheme of the Stern-Gerlach ion source at MLL, figure taken from Ref. [47]. 50

3.3 Schematic picture of a tandem Van de Graaff accelerator. . . 51

3.4 The Q3D magnetic spectrograph, illustrating the trajectory of a light charged ejectile to the focal plane. 52

3.5 The Q3D vault at MLL. 53

3.6 Schematic diagram of the focal plane detector at the Q3D spectrograph as shown in Ref. [48]. 54

3.7 Left panel: particle identification, ΔE_1-ΔE_2 plot showing the partial energy loss of ejectiles in the two proportional counters. Right panel: ΔE_2-E plot showing the ejectiles' energy loss in the second proportional counter and total energy deposited on the plastic scintillator. 56

3.8 Comparison between experimental data and DWBA predictions of angular distributions for ^{136}Ba(p, p) elastic scattering. Proton OMPs were taken from Becchetti and Greenless (BG) [57], Koning and Delaroche (KD) [58], Varner *et al.* [56], Walter and Guss (WG) [11]. 64

3.9 Comparison between experimental data and DWBA predictions of angular distributions for ^{138}Ba(p, p) elastic scattering . Proton OMPs were taken from Becchetti and Greenless (BG) [57], Koning and Delaroche (KD) [58], Varner *et al.* [56], Walter and Guss (WG) [11] and Menet *et al.* [59]. 64

3.10 Acceptance slits at the Q3D spectrograph. 67

3.11 Triton angular distribution for the ground state in ^{134}Ba. The DWBA curves are obtained using two different triton OMPs, t + ^{134}Ba set by Li, Liang, and Cai [61] and t + ^{134}Ba set by Becchetti and Greenless [62]. 69

4.1 Triton spectra corresponding to excited states in ^{134}Ba obtained from this experiment. These data were collected with five magnetic field settings (momentum bites) and represent one angle at $\theta_{lab} = 25°$. The 0^+ states observed in this experiment and specific contaminants are labeled in this figure. . . . 72

4.2 Angular distributions of 0^+ states in ^{134}Ba, observed with the ^{136}Ba(p,t) reaction. 88

A.1 Input file sample for $L = 2$ transfer in ^{136}Ba$(p,t)^{134}$Ba reaction. 92

List of Tables

3.1 Polynomial fit parameters for the energy calibration in each momentum setting. 57

3.2 Optical model parameters used our analysis. The proton OMPs are from Varner *et al.* [56], triton OMPs from Li, Liang, and Cai [61] and neutron OMPs are from Ref. [57]. The triton parameters are given as a function of triton energy E_t, mass number $A = 134$, atomic number $Z = 56$, and neutron number $N = 78$. 70

4.1 Excitation energy levels in ^{134}Ba observed in this experiment compared to previously known information, taken from the Nuclear Data Sheets [63]. 73

4.2 Relative (p, t) strength calculations of all excited 0^+ states in ^{134}Ba observed in this experiment. The integrated strength calculations take into account all the 0^+ states relate to the ground state.N is the DWBA to data normalization. 87

Chapter 1

Introduction

1.1 Standard Model of Particle Physics

The standard model (SM) of particle physics describes the constituents of matter at the most fundamental level [1]. It unifies the electromagnetic, strong and weak interactions, and classifies elementary particles in three fermion generations of quarks and leptons as shown in Fig. 1.1 and below:

$$\begin{pmatrix} u \\ d \end{pmatrix}, \quad \begin{pmatrix} c \\ s \end{pmatrix}, \quad \begin{pmatrix} t \\ b \end{pmatrix} \quad \textit{quarks} \tag{1.1}$$

$$\begin{pmatrix} \nu_e \\ e \end{pmatrix}, \quad \begin{pmatrix} \nu_\mu \\ \mu \end{pmatrix}, \quad \begin{pmatrix} \nu_\tau \\ \tau \end{pmatrix} \quad \textit{leptons} \tag{1.2}$$

The quarks interact through the strong, electromagnetic and weak interactions, whereas the leptons interact through the electromagnetic and weak interactions. These interactions are mediated by spin-1 bosons, which are photons for the electromagnetic interaction, the $W^{\pm}$ and Z^0 bosons for weak

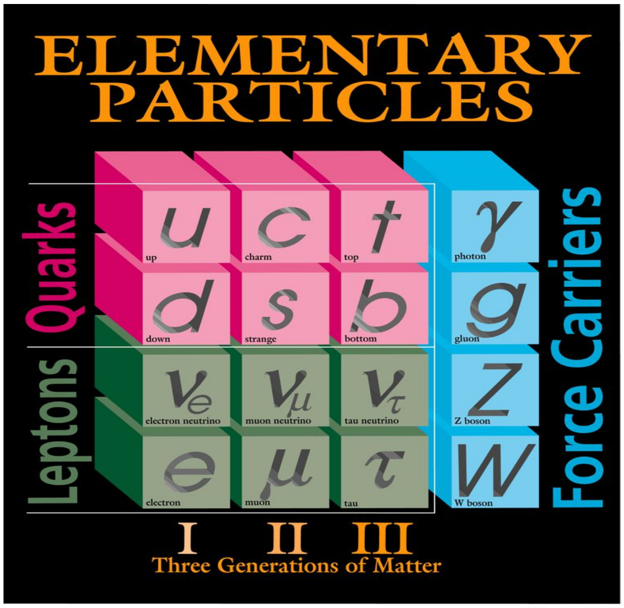
ELEMENTARY PARTICLES
Quarks
Leptons
Force Carriers
u
up
c
charm
t
top
d
down
s
strange
b
bottom
ν_e
electron neutrino
ν_μ
muon neutrino
ν_τ
tau neutrino
e
electron
μ
muon
τ
tau
γ
photon
g
gluon
Z
Z boson
W
W boson
I II III
Three Generations of Matter

Fermilab 95-759

Figure 1.1: Classification of elementary particles and their interactions according to the standard model. Figure taken from Ref.[2].

interactions and gluons for the strong interaction. The photons and gluons are massless bosons, whereas the $W^{\pm}$ and Z^0 bosons are highly massive ($M_{W^{\pm}} \sim 80$ GeV, $M_{Z^0} \sim 90$ GeV). The large masses of the weak interaction bosons is explained by the symmetry-breaking field associated with a Higgs boson [3]. Although the SM has been very successful so that experimental data matched theoretical predictions, there are still various arguments that lead to the undoubtable conclusion that the SM is not a complete theory describing the fundamental particles and their interactions. For example, the SM assumed neutrinos to be massless. However the observation of neutrino oscillations imply that they must have mass. Today it is accepted that neutrinos are very light neutral leptons listed in the top row of Eq. (1.2) that only interact with matter via weak interactions (if one ignores gravity). Below I describe some salient aspects of neutrino physics and weak interaction theory relevant for this work.

1.2 A brief history

In the early years it was assumed that a nuclear beta decay was a two-body kinematics problem. However, the experimentally measured energy distribution for electrons (positrons) from a given decay showed a continuous energy spectrum (Fig. 1.2).

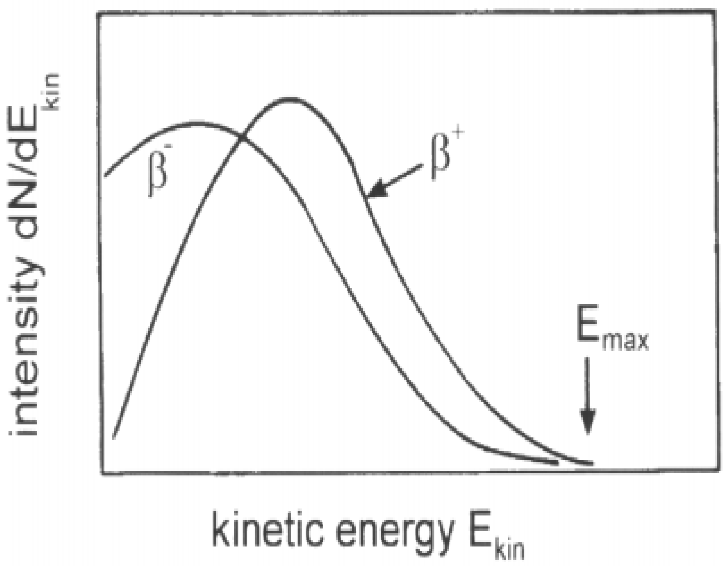

Figure 1.2: Energy distribution of electrons and positrons observed during beta decays. Figure taken from Ref. [4].

The continuous spectra shown in Fig. 1.2 could only be interpreted as non-conservation of energy and momentum or a missing particle. To account for fundamental conservation laws, Pauli postulated in 1932 the existence of an extremely light spin-1/2 neutral particle which was not detected as it interact very weakly with matter. He called the missing particle a neutron. Later Fermi presented a more rigorous theory for beta decays using a current-current interaction [3] and called the new particle a neutrino (little neutral one in Italian).

1.3 Lepton number conservation

In 1946 Bruno Pontecorvo proposed the radiochemical method for neutrino detection, which was based on the observation of processes such as

$$\nu_e + n \longrightarrow p + e^-. \tag{1.3}$$

Indeed this process was measured by the famous Homestake measurement [5, 6] in which solar neutrinos from fusion reactions in the sun were detected using the reaction

$$\nu_e + {}^{37}\mathrm{Cl} \longrightarrow {}^{37}\mathrm{Ar} + e^-. \tag{1.4}$$

During the same time other experiments that used nuclear reactors as a source of neutrinos did not observe a similar process. However the Reines and Cowan experiment [7] did successfully observe a process of the type

$$\nu_e + p \longrightarrow n + e^+, \tag{1.5}$$

from nuclear reactors. This clearly indicated that the neutrinos from reactors were not the same as neutrinos from the sun and led to the definition of *lepton* *number* to label the neutrinos, so that the reactor neutrinos were actually *anti-neutrinos*, with lepton number $L = -1$. Therefore, the observed process in the Reines-Cowan experiment was

$$\bar{\nu}_e + p \longrightarrow n + e^+. \tag{1.6}$$

In summary, experimental evidence shows that the processes

$$n + \nu_e \longrightarrow p + e^- \tag{1.7}$$

and

$$p + \bar{\nu}_e \longrightarrow n + e^+ \tag{1.8}$$

are allowed (observed), while the processes

$$n + \bar{\nu}_e \longrightarrow p + e^- \tag{1.9}$$

and

$$p + \nu_e \longrightarrow n + e^+ \tag{1.10}$$

are forbidden (not observed). This leads to the conservation rule for lepton number, so that lepton number for particles is +1 and for antiparticles it is −1.

The neutrinos emitted from beta decays are therefore labeled as

$$n \longrightarrow p + e^- + \bar{\nu}_e \tag{1.11}$$

and

$$p \longrightarrow n + e^+ + \nu_e. \tag{1.12}$$

The above clearly shows that (based on experimental evidence alone) neutrinos and anti-neutrinos ought to be distinct from one another (or are Dirac particles). However, this picture describing neutrino charge-conjugation properties is not based on any fundamental physical principles. A $\bar{\nu}_e$ and ν_e can still be indistinguishable as they are both electrically neutral spin 1/2 elementary fermions. This possibility was put forth in 1937 by Ettore Majorana and would result in neutrinoless double beta decay ($0\nu\beta\beta$), represented by,

$$2n \longrightarrow 2p + 2e^-. \tag{1.13}$$

This $0\nu\beta\beta$ process (discussed further in Section 1.5) would violate lepton number number conservation by two units due to the absence of anti-neutrinos. However such a decay is ruled out for massless neutrinos due to the phenomenon of parity violation in weak interactions, that was both proposed and experimentally observed in the 1950's. I briefly describe the symmetry properties of the parity (space-reflection) operator and its associated conservation law below.

1.4 Parity violation in weak interactions

Parity is also known as mirror or left-right symmetry, as the parity operator P results in a spatial inversion about the origin, so that the operator transforms the sign of true vectors $(x, y, z) \longrightarrow (-x, -y, -z)$ while leaving axial-vectors unchanged [3].

For example, a parity transformation on an angular momentum vector (an axial vector) $\vec{L} = \vec{r} \times \vec{p}$ leads to

$$P\vec{L} = \vec{L}. \tag{1.14}$$

From the above one can clearly see that the eigenvalues of P are either $+1$ or -1. Parity symmetry leads to a multiplicative conservation law. Therefore, if a composite system is made of two non-interacting sub systems with parities π_1 and π_2, then the parity π of the combined system is the product

$$\pi = \pi_1 \pi_2. \tag{1.15}$$

So, if parity were conserved, then all physical processes would occur with no distinction of left and right. In fact, parity is conserved in electromagnetic and strong interactions, but violated *maximally* in weak interactions. Historically, parity conservation was under question with the famous tau-theta puzzle [1]. Two particles, the τ and the θ appeared to be identical in every way (with same mass, spin, charge, etc.), yet they decayed via two different modes

$$\theta^+ \longrightarrow \pi^+ + \pi^0 \tag{1.16}$$

and

$$\tau^+ \longrightarrow \pi^+ + \pi^+ + \pi^-. \tag{1.17}$$

One can clearly see from the above that the reaction products in the two decays have opposite parity, based on the multiplicative conservation rule in Eq. (1.15). It was a puzzle that the two particles can be identical in every respect, expect with opposite parities in their decay products. This paradox was resolved by Lee and Yang who postulated that parity was violated in weak interactions and that the two particles were in fact the same particle (called a kaon) [8].

In 1956, Wu and Ambler *et al.* [9] performed a ground breaking experiment to observe parity violation in nuclear β decays. The experiment used samples of ^{60}Co placed in a strong magnetic field, so that they were polarized along the axis of the $\vec{B}$ field. ^{60}Co decays via the β^- decay mode to ^{60}Ni, which de-excites to its ground state by emitting two gamma rays,

$$^{60}\mathrm{Co} \longrightarrow {}^{60}\mathrm{Ni} + e^- + \bar{\nu}_e + 2\gamma. \tag{1.18}$$

Since electromagnetic interactions conserve parity, the distribution of emitted gamma rays was used to check the polarization of the emitted electrons with respect to the oriented nuclear spin. By comparing the distribution of the gamma rays and the emitted electrons when the ^{60}Co nuclei are polarized in (say) the positive $\hat{z}$ direction to when they are polarized in the negative $\hat{z}$ direction, Wu and collaborators found that about 60% of gamma rays were emitted in one direction, while $\sim$ 40% were emitted in the other. In contrast the electrons were always emitted preferentially in a direction opposite to that of the ^{60}Co spin [9]. This implied that parity is violated in weak interactions. A schematic representation of the experiment is illustrated in Fig. 1.3.

The Wu experiment was followed by another elegant experiment by Goldhaber, Grodzins and Sunyar [11] who experimentally determined the helicity of neutrinos (described below). They used the electron capture decay of

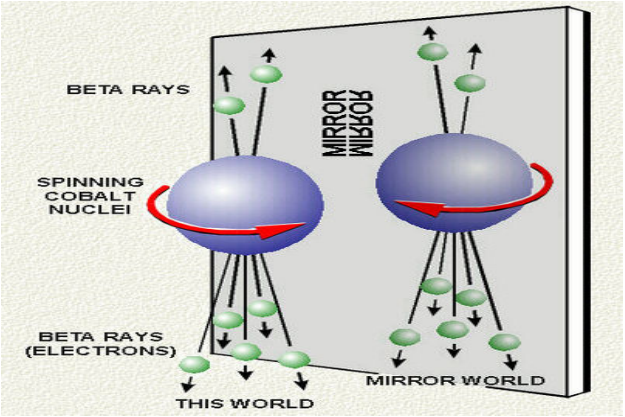

Figure 1.3: Observed electron angular distributions when the nucleus is polarized along positive z-axis (left side), and when the nucleus is polarized in the negative z-axis (right side). Figure taken from Ref. [10]

$^{152}\mathrm{Eu}^{\mathrm{m}}$

$$^{152}\mathrm{Eu}^{\mathrm{m}} + e^{-} \longrightarrow {}^{152}\mathrm{Sm}^{*} + \nu_e \tag{1.19}$$

which leaves $^{152}\mathrm{Sm}$ in an excited state that makes a transition to the ground state and emits a γ-ray.

$$^{152}\mathrm{Sm}^{*} \longrightarrow {}^{152}\mathrm{Sm} + \gamma. \tag{1.20}$$

Let us assume that the neutrino is emitted towards the right, along the z axis so that the recoil of the nucleus is towards the left. Goldhaber *et al.* experiment showed that the γ-rays from the decay were always right-circularly polarized (Fig. 1.4).

Since both $^{152}\mathrm{Eu}^{\mathrm{m}}$ and $^{152}\mathrm{Sm}$ have spin 0 in their ground state, the change in angular momentum by the whole process is ΔJ =1/2, which must be carried away by the photon and the neutrino. On choosing the quantization

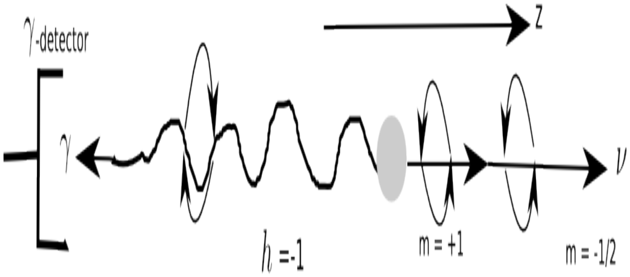

Figure 1.4: Schematic representation of Goldhaber *et al.* experiment.

axis to be along the direction of the γ-ray, it is clear that the projections of the spins (or magnetic substates) of the photon, the neutrino and the captured electron along the $\hat{z}$ direction should be either $m_\gamma = +1$, $m_{\nu_e} = -1/2$ and $m_e = -1/2$, or $m_\gamma = -1$, $m_{\nu_e} = +1/2$ and $m_e = +1/2$. The right circular polarization of the γ-ray shows that $m_\gamma = -1$, which implies that $m_{\nu_e} = +1/2$. The selectivity of the experiment ensured that the momentum of the neutrino was always opposite to that of the γ-ray for the data that were recorded. One can then define the helicity of a neutrino as the projection of its intrinsic spin along the direction of its momentum. Clearly, since the neutrinos are in an opposite direction to the γ-rays and m_{ν_e} can only be $= +1/2$, the experiment shows that neutrinos have helicity $h = -1$ or are *left-handed.* In other words, the direction of neutrino's spin is always opposite to its momentum. This is the concept of a helicity eigenstate = -1. Since neutrinos are nearly massless fermions that move at relativistic speeds, they are best described by the Dirac equation, which clearly shows that the existence of anti-particles are an essential requirement to explain its negative energy solutions [1]. Further, if one defines a charge conjugation operator that converts particles to anti-particles, it naturally follows that a charge-conjugated left-handed fermion field is converted to a right-handed field [1]. Thus, anti-neutrinos should have (positive) helicity $h = 1$ or are *right-handed* (or momentum and intrinsic spin pointing in the same direction).

The above experiments show that massless neutrinos (or anti-neutrinos) carried an additional label of handedness (or helicity). This forbids neutrinoless double beta decay processes shown in Eq. (1.13) due to "helicity suppression", which can be explained as follows. Assume the $0\nu\beta\beta$ decay shown in Eq. (1.13) can be represented by two simultaneous β decays through virtual states, so that the first neutrino is absorbed by a neutron in the nuclear medium to produce a second electron (assuming that the neutrino is Majorana particle or $\nu_e \equiv \bar{\nu}_e$).

Then, the $0\nu\beta\beta$ decay process (Eq. (1.13)) is forbidden for massless Majorana neutrinos because the neutrino that is emitted and then reabsorbed is required to have opposite helicities for the two processes (section 1.3). Therefore, if parity were maximally violated and only left-handed massless neutrinos (and right handed anti-neutrinos) exist in nature, then $0\nu\beta\beta$ decays of the type shown in Eq. (1.13) would be impossible.

1.5 Massive neutrinos and $0\nu\beta\beta$ decays

Although since their discovery, neutrinos were assumed to be massless particles, this was proved to be not the case in the late 20^{th} century. It was first predicted by Pontecorvo in 1957 that if neutrinos had mass they would undergo a quantum mechanical phenomenon called neutrino oscillations, whereby a neutrino with a specific flavor (electron neutrino ν_e, tau neutrino ν_τ, or muon neutrino ν_μ) would change to a different flavor after a certain flight time [12]. Indeed, neutrino oscillation experiments such as Super-Kamiokande [13], SNO [14], GALLEX [15] etc., revealed that neutrinos do oscillate from one type to another. Thus they ought to be non-zero mass particles. Additionally the three neutrino flavors (ν_e, ν_τ, ν_μ) are not expected to have the same mass. The eigenstates of flavor are related to the mass eigenstates via the transformation

$$\begin{pmatrix} \nu_e \\ \nu_\mu \\ \nu_\tau \end{pmatrix} = \begin{pmatrix} U_{e_1} & U_{e_2} & U_{e_3} \\ U_{\mu_1} & U_{\mu_2} & U_{\mu_3} \\ U_{\tau_1} & U_{\tau_2} & U_{\tau_3} \end{pmatrix} \begin{pmatrix} \nu_1 \\ \nu_2 \\ \nu_3 \end{pmatrix}, \tag{1.21}$$

where the 3×3 matrix is called the Pontecorvo-Maki-Nakagwa-Sakata (PMNS) neutrino mixing matrix [12]. The probability that a neutrino changes flavor $\nu_\alpha \longrightarrow \nu_\beta$ is given by [16],

$$\begin{aligned} P_{\alpha\longrightarrow\beta} = \delta_{\alpha\beta} - 4\sum_{i>j} Re\left[U_{\beta i}U^*_{\alpha i}U^*_{\beta j}U_{\alpha j}\right]\sin^2\left[\frac{(m_j^2 - m_i^2)L}{4E}\right] \\ - 2\sum_{i>j} Im\left[U^*_{\alpha i}U_{\beta i}U_{\alpha j}U^*_{\beta j}\right]\sin\left[\frac{(m_j^2 - m_i^2)L}{2E}\right]. \end{aligned} \tag{1.22}$$

In other words, neutrino oscillation experiments only determine neutrino mass squared differences and not absolute masses. One method to determine the absolute neutrino mass scale is described below.

1.5.1 Double beta decays in atomic nuclei

Unlike the decay shown in Eq. (1.13), two neutrino double beta decays ($2\nu\beta\beta$) of the type

$$2n \longrightarrow 2p + 2e^- + 2\bar{\nu}_e \tag{1.23}$$

are allowed to occur in nuclei where the nuclear pairing force forbids single β decays. One such example is relevant for this thesis and is shown in Fig 1.5, where ^{136}Xe double beta decays to ^{136}Ba via a second-order weak process.

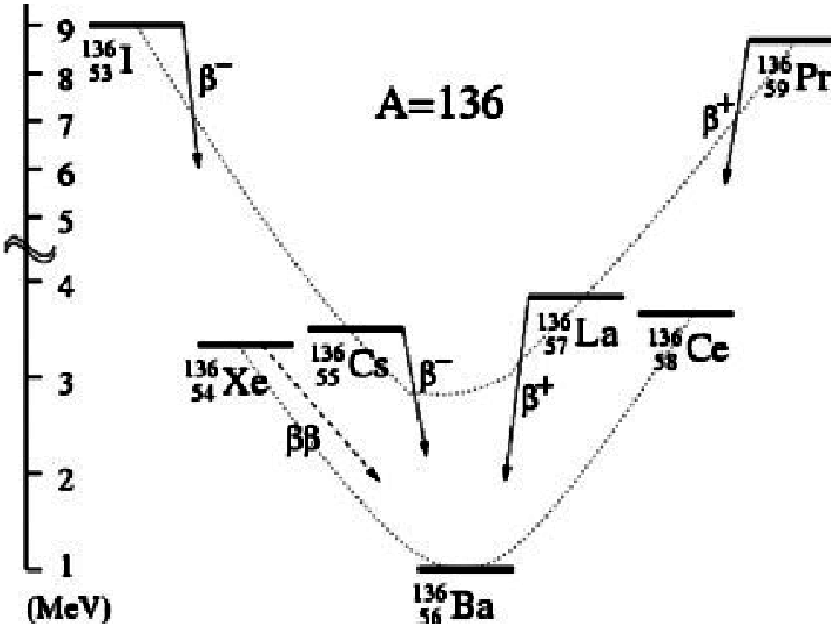
9
8
7
6
5
4
3
2
1
(MeV)
$^{136}_{53}$I
β⁻
A=136
$^{136}_{59}$Pr
β⁺
$^{136}_{54}$Xe
ββ
$^{136}_{55}$Cs
β⁻
$^{136}_{57}$La
β⁺
$^{136}_{58}$Ce
$^{136}_{56}$Ba

Figure 1.5: Mass parabola for A = 136 isobars. Although ^{136}Xe cannot β decay to ^{136}Cs, $\beta\beta$ decays to ^{136}Ba are allowed. Figure taken from Ref [17].

Clearly, from the mass parabola shown above, single beta decays from ^{136}Xe to ^{136}Cs are energetically forbidden. As mentioned previously, the $2\nu\beta\beta$ decay process is allowed in the SM as it conserves lepton number . This process is very rare and have been observed in several isotopes, with long lifetimes ranging between $10^{19} - 10^{22}$ years.

Since now neutrinos are known to possess mass, their description using a helicity operator is not appropriate any more, as helicity is not Lorentz invariant for massive particles. If some new (unknown) physics mechanism allows a Lorentz transformation that changes the sign of a neutrino's helicity, $0\nu\beta\beta$ decays of the type shown in Eq. (1.13) would be allowed. Most theories that aim to go beyond the standard model incorporate this effect for massive neutrinos and require a violation of lepton number by 2 units. However $0\nu\beta\beta$ decays are expected to be highly suppressed due to the smallness of neutrino masses. The Feynman diagrams for both the SM allowed $2\nu\beta\beta$ decay and the SM forbidden $0\nu\beta\beta$ decay are shown in Fig 1.6.

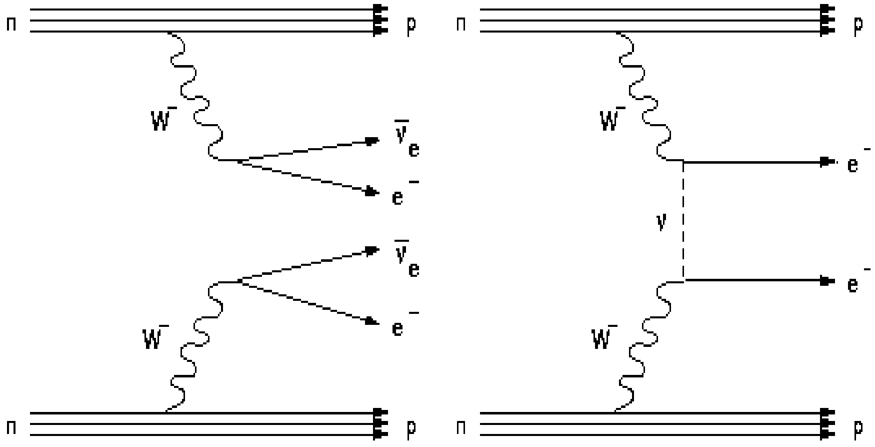

Figure 1.6: Left panel: $2\nu\beta\beta$ decay. Right panel: $0\nu\beta\beta$ decay.

If one assumes the dominant mechanism driving a $0\nu\beta\beta$ decay is the exchange of light Majorana neutrinos, the measured decay rate will be

$$\left(T^{0\nu}_{1/2}\right)^{-1} = G^{0\nu}(Q,Z)|M^{0\nu}|^2 \left(\frac{\langle m_{\beta\beta}\rangle}{m_e}\right)^2, \tag{1.24}$$

where $G^{0\nu}(Q,Z)$ is a phase space factor, m_e is the electron mass, $M^{0\nu}$ is the nuclear matrix element (NME) for the decay and $m_{\beta\beta}$ is the effective Majorana mass of the electron neutrino. For three neutrino flavors,

$$m_{\beta\beta} = \sum_{i=1}^{3} m_i U_{ei}^2, \tag{1.25}$$

where the U_{ei} are elements of the PMNS neutrino mixing matrix described previously. Therefore, one can determine the effective Majorana mass of an electron neutrino from a measured $0\nu\beta\beta$ decay rate. However this requires that the NME for the decay is evaluated accurately. This aspect has always proved to be very challenging. Current theoretical calculations report NME values with significant disagreements depending on the nuclear model used (Fig. 1.7). Below I provide a brief discussion on the two main theoretical models used for calculations of NMEs for $0\nu\beta\beta$ candidates. I place emphasis on the current status of ^{136}Xe $\longrightarrow$ ^{136}Ba $0\nu\beta\beta$ decay, which is relevant for this work.

1.5.2 $0\nu\beta\beta$ Nuclear Matrix Elements

The theoretical models currently used to evaluate nuclear matrix elements of $0\nu\beta\beta$ decay candidates include the quasiparticle random phase approximation (QRPA) [18], interacting shell model (ISM) [19], projected Hartree-Fock Bogoluibov (P-HBF) method [20], interacting boson model (IBM) [21] and energy density functional method (EDF) [22]. Below I briefly discuss the QRPA and the ISM, which are two of the most commonly used approaches to evaluate the NMEs.

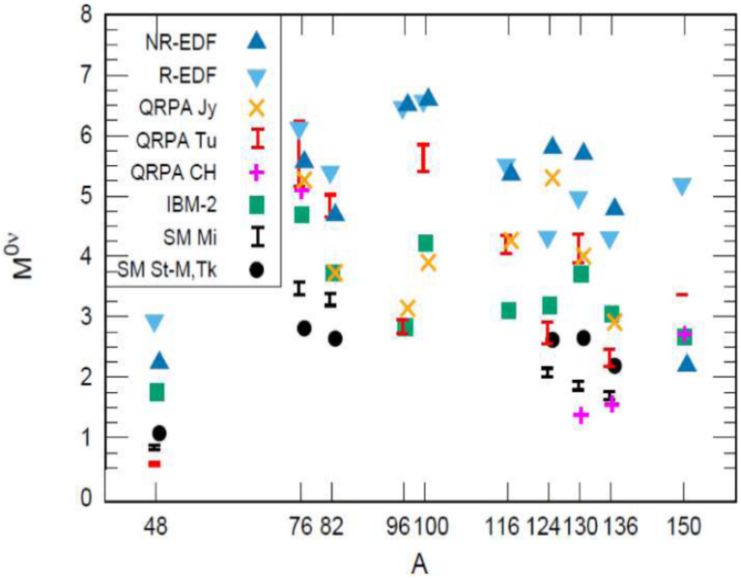

Figure 1.7: Calculated NMEs for several $0\nu\beta\beta$ decay candidates using different theoretical approaches. Figure taken from Ref [23].

Interacting Shell Model (ISM)

Within the shell model each nucleon in an atomic nucleus experiences an average potential due to the other nucleons. The nucleons occupy eigenstates labeled by quantum numbers nlj, similarly as the wavefunctions of individual electrons in atoms. The shell model explains very accurately several properties of nuclei with specific number of protons Z and number of neutrons $N = (A - Z)$ called “magic numbers” (2, 8, 20, 28, 50, 82, 126). For example, nuclei in which the number of protons and the number of neutrons are equal to magic numbers are called closed shell nuclei. Such nuclei have a much higher binding energy compared to their neighbours, analogous to noble gas atoms that have their electronic shells completely filled.

The shell model nuclear Hamiltonian is expressed as a sum of independent-particle Hamiltonians $\hat{H}_0$ and a residual interaction $\hat{V}$ [24],

$$\hat{H} = \hat{H}_0 + \hat{V}. \tag{1.26}$$

Here $\hat{H}_0$ is the summed single-particle Hamiltonian

$$\hat{H}_0 = \sum_{i=1}^{A} \hat{h}_i, \tag{1.27}$$

where $\hat{h}_i$ represents the Hamiltonian of the i^{th} nucleon. The single-particle motion of i^{th} nucleon in an average central potential $U(r_i)$ is

$$\hat{h}_i = \frac{\hat{p}_i^2}{2M} + U(r_i), \tag{1.28}$$

where $\hat{p}_i = -i\hbar\nabla_i$ is the momentum of the i^{th} nucleon [24].
To obtain solutions to the Schrödinger equation for the Hamiltonian $\hat{H}$, one needs an appropriate potential describing the short-range nuclear force. Although the square-well and the spherical harmonic oscillator potentials in principle provide single-particle wavefunctions in analytic form, these are not good approximations of the nuclear potential. The square-well potential for example requires an infinite amount of energy to take out a nucleon from the well, and the harmonic oscillator potential tends to infinity at large r. A

reasonable potential is the Woods-Saxon potential defined by [24]

$$U(r) = -V_0 \left[1 + \exp\left(\frac{r-R}{a}\right)\right]^{-1} \tag{1.29}$$

where $R = 1.25A^{1/3}\ fm$, $a = 0.524\ fm$ is the half distance and $V_0 \simeq 50$ MeV. Figure 1.8 shows a comparison between harmonic oscillator potential (HO) and the Woods-Saxon potential (WS).

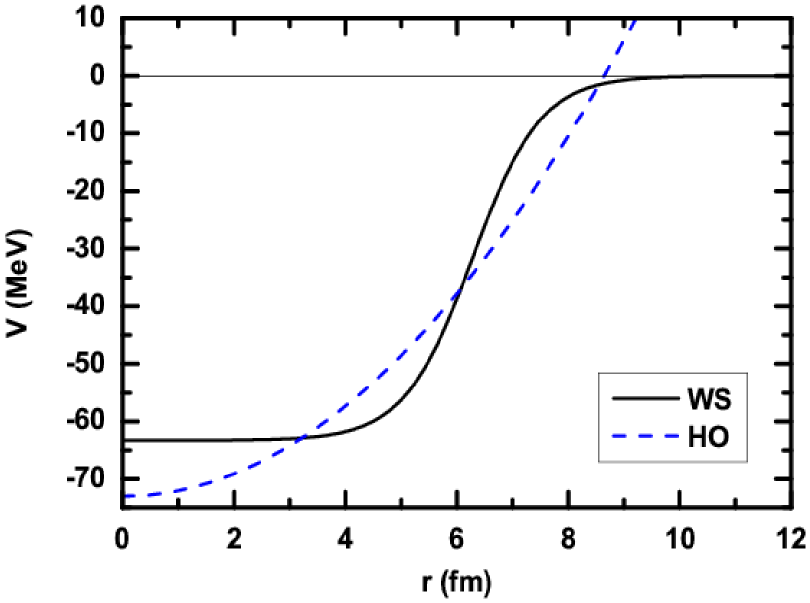

Figure 1.8: Single-particle shell model potentials. Figure taken from Ref. [25].

Although the Woods-Saxon potential seems realistic, it is not sufficient by itself to describe experimental data adequately. One needs to take into consideration the spin-orbit coupling $V_{so}\vec{l}\cdot\vec{s}$, where $\vec{l}$ is the orbital angular momentum and $\vec{s}$ is the intrinsic spin of a nucleon. Since,

$$j^2 = (\vec{l} + \vec{s})^2 = l^2 + s^2 + 2\vec{l} \cdot \vec{s}, \tag{1.30}$$

the spin-orbit coupling is described by the operators

$$\vec{l} \cdot \vec{s} = \frac{1}{2}(j^2 - l^2 - s^2), \tag{1.31}$$

whose expectation value is

$$\langle \vec{l} \cdot \vec{s} \rangle = \frac{1}{2}\left[j(j+1) - l(l+1) - s(s+1)\right]. \tag{1.32}$$

Since $s = 1/2$, we have two possible values of total angular momentum for a given nucleon, $j = l + 1/2$ and $j = l - 1/2$, with energies -$\frac{1}{2}l\hbar^2$ and -$\frac{1}{2}(l+1)\hbar^2$ respectively. The spin-orbit coupling leads to the energy splitting so that the higher j have lower energy and reproduces all the magic numbers showing an explicit shell structure (Fig. 1.9). The shell model describes nuclear properties using a valence space in which active nucleons occupy a few single-particle states outside an inert core (the Fermi surface). Within this limited valence space, the full configuration interaction eigenstates and eigenvalues are obtained by diagonalizing the Hamiltonian for the many body nuclear wavefunctions. However, this model works best for reasonably lighter nuclei. Current computational capabilities allow arbitrarily complex correlations within the valence nucleons to perform state-of-the-art calculation of nuclear observables.

In the shell model calculations for ^{136}Xe $0\nu\beta\beta$ decay, the valence space is limited to magic numbers 50 and 82 (shown in Fig. 1.9) for the protons and neutrons. This restricts the calculations to only the ($0g_{7/2}$, $1d_{5/2}$, $1d_{3/2}$, $2s_{1/2}$, $0h_{11/2}$) orbitals. The two-body decay operators are [19]

$$\begin{aligned}\hat{M}^{0\nu} &= \sum_{j}\left(\sum_{i,j,k,l} M^{J}_{i,j,k,l}\left[(a^{\dagger}_{i}a^{\dagger}_{j})^{J}(a_k a_l)^{0}\right]\right)\\ &= \sum_{J^{\pi}} \hat{P}^{\dagger}_{J^{\pi}}\hat{P}_{J^{\pi}},\end{aligned} \tag{1.33}$$

where the $\hat{P}$ operators annihilate pairs of neutrons and $\hat{P}^{\dagger}$ operators create pairs of protons coupled to the same spin and parity J^{π}. The dominant contribution to the NME is found to be from $J = 0$ pairs, while the $J > 0$ couplings mainly cancel this term [19].

Quasiparticle Random Phase Approximation (QRPA)

Unlike the ISM, the QRPA calculations use a large valence space, but with restricted configurations for the valence nucleons [18]. One of the main approximations used in the QRPA calculations is the Bardeen-Cooper-Schrieffer (BCS) approximation for pairing between like nucleons. The BCS theory assumes the formation of Cooper pairs for the neutrons and protons similar to bound state electron pairs in a superconductor [24].

Assuming a weak pairing interaction between the identical nucleons, similar to the BCS theory of electrons [24], the nucleons occupy states in time-reversed orbits ψ_{jm} and ψ_{j-m}. The nuclear many body system can be expressed similarly as electrons, as an antisymmetrized product function, given by a Slater determinant. The occupancy of each state is treated statistically, using the second quantization formalism. The pairing interaction is given

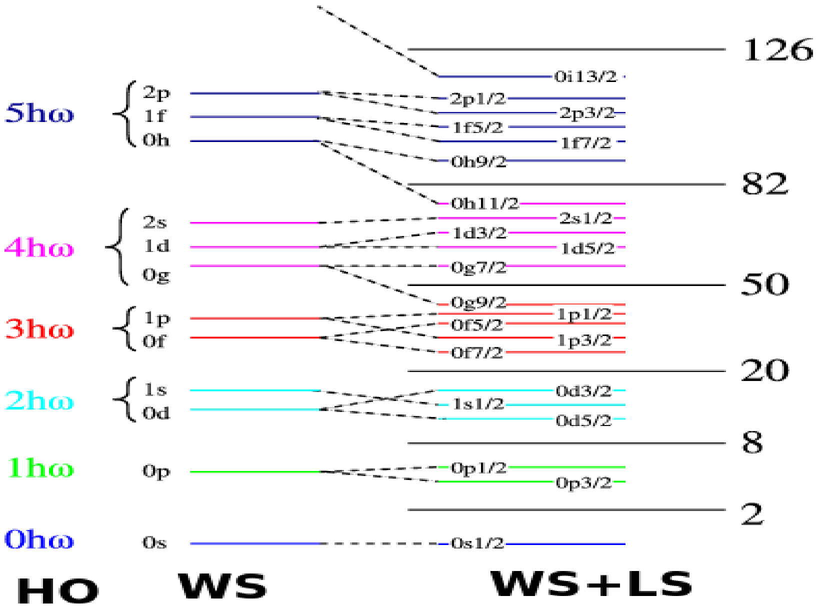
126
0i13/2
5hω
2p
1f
0h
2p1/2
2p3/2
1f5/2
1f7/2
0h9/2
82
0h11/2
4hω
2s
1d
0g
2s1/2
1d3/2
1d5/2
0g7/2
50
0g9/2
3hω
1p
0f
1p1/2
0f5/2
1p3/2
0f7/2
20
2hω
1s
0d
0d3/2
1s1/2
0d5/2
8
1hω
0p
0p1/2
0p3/2
2
0hω
0s
0s1/2
HO
WS
WS+LS

Figure 1.9: Single-particle levels obtained with the harmonic oscillator potential (HO), Woods-Saxon potential (WS) and Woods-Saxon plus spin-orbit coupling (WS+LS). Figure taken from Ref [26].

by [27]

$$V_{pair} = -G \sum_{mm'} a^{\dagger}_{jm} a^{\dagger}_{j\bar{m}} a_{j\bar{m}'} a_{jm}, \tag{1.34}$$

where

$$a^{\dagger}_{jm} \left|0\right\rangle = \psi_{jm} \tag{1.35}$$

and

$$a^{\dagger}_{j\bar{m}} \left|0\right\rangle = (-)^{j-m} \psi_{j-m}. \tag{1.36}$$

In the above, G represents the strength of the pairing interaction and $a^{\dagger}$ and

a are creation and annihilation operators operating on the vacuum state $|0\rangle$. The ground state BCS wavefunction is then [27]

$$\psi_G = \prod_{\nu} (U_\nu + V_\nu a^\dagger_\nu a^\dagger_{\bar{\nu}})\,|0\rangle \tag{1.37}$$

for paired states $|jm\rangle$ and $|j\bar{m}\rangle$, which are labeled as ν amd $\bar{\nu}$. The U_ν and V_ν coefficients are the amplitudes for the occupation probabilities of a state $|\nu\rangle$ for a pair of nucleons. If we choose $|V_\nu|^2$ to be the probability that a paired state is occupied, then $|U_\nu|^2 = 1$ - $|V_\nu|^2$ is the probability that it is not occupied. If one defines $U_\nu = \sin\theta_\nu$ and $V_\nu = \cos\theta_\nu$, then the normalization condition $U^2_\nu + V^2_\nu = 1$ is satisfied. The other constraint is from the total nucleon number n, defined so that

$$2 \sum_{\nu} |V_\nu|^2 = n. \tag{1.38}$$

One can then use the ground state energy minimum using a variational method to solve for V_ν and U_ν

$$\frac{\partial W_{BCS}}{\partial \theta_\nu} = 0, \tag{1.39}$$

where one can define

$$\xi_\nu = (\epsilon_\nu - E_F), \tag{1.40}$$

ϵ_ν being the single particle energy where, $\epsilon_k = \frac{\hbar^2 k^2}{2m}$, and ξ_ν represents the energy above the Fermi surface. The variational result yields (for the ground state) [27]

$$V^2_\nu = \frac{1}{2}\left[1 - \frac{\xi_\nu}{(\Delta^2 + \xi^2_\nu)^{1/2}}\right], \tag{1.41}$$

and

$$U_\nu^2 = \frac{1}{2}\left[1 + \frac{\xi_\nu}{(\Delta^2 + \xi_\nu^2)^{1/2}}\right], \tag{1.42}$$

where

$$E_\nu = \sqrt{\Delta^2 + \xi_\nu^2} \tag{1.43}$$

and Δ is the minimum excitation energy or the pairing gap

$$\Delta = G \sum_\nu U_\nu V_\nu. \tag{1.44}$$

The QRPA many body calculations of $0\nu\beta\beta$ decay matrix elements allow the use of a much larger configuration space compared to the ISM, but with fewer correlations. A similar cancellation between $J = 0$ and $J > 0$ pairs of the NME has been observed in the QRPA calculations as well. Importantly, in the QRPA calculations, nucleon pairing is treated separately using the BCS approximation [28]. Furthermore, the calculations mostly assume spherical ground states for the parent and daughter nuclei, which need not be the case. This aspect is further discussed in the conclusion section of chapter 4.

1.5.3 Current experimental status of ^{136}Xe$\longrightarrow^{136}$Ba $0\nu2\beta$ decay

Currently there are several experiments ongoing to search for neutrinoless double beta decays. Some of these include KamLAND-ZEN [29], EXO-200 [30], CUORE [31], Majorana Demonstrator [32], GERDA [33] and CUPID-0 [34]. Below I describe briefly the KamLAND-Zen and EXO-200 experiments, which aim to observe the $0\nu2\beta\beta$ decay of ^{136}Xe. As mentioned previously, this candidate is relevant for this thesis and has the following advantages over other $0\nu\beta\beta$ decay experiments.

- ^{136}Xe is relatively abundant (8.9%), affordable and easy to purify.
- The liquid or gaseous Xe can be used as a time projection chamber (TPC). This allows for maximal background rejection using the method of barium ion tagging [35].
- ^{136}Xe is singly closed shell with $N = 82$ and $Z = 54$. So the matrix element calculations for its $0\nu\beta\beta$ decay are expected to be relatively easier.
- Its standard model allowed $2\nu\beta\beta$ decay background is highly suppressed, with a measured value of its matrix element being $\mathrm{M}^{2\nu} \approx 0.02$ MeV^{-1} [36]. As shown in Fig. 1.10, this means that large background structure on the left will be significantly diminished for this case.

It is due to the above advantages that the most sensitive limit explicitly obtained to date for $m_{\beta\beta}$ is from a ^{136}Xe $\beta\beta$ decay experiment with KamLAND-Zen (described below), with $m_{\beta\beta} \leq$ 61-165 meV [29], depending on the choice of the matrix element for the decay.

The EXO-200 experiment

EXO-200 is a cylindrical homogeneous time projection chamber (TPC), which uses $\sim$ 81% enriched ^{136}Xe as both source and the detector [38]. This detector is designed to minimize radioactive backgrounds, use maximally enriched liquid Xe, and provide good energy resolution at the Q-value of $\sim$ 2.4 MeV.

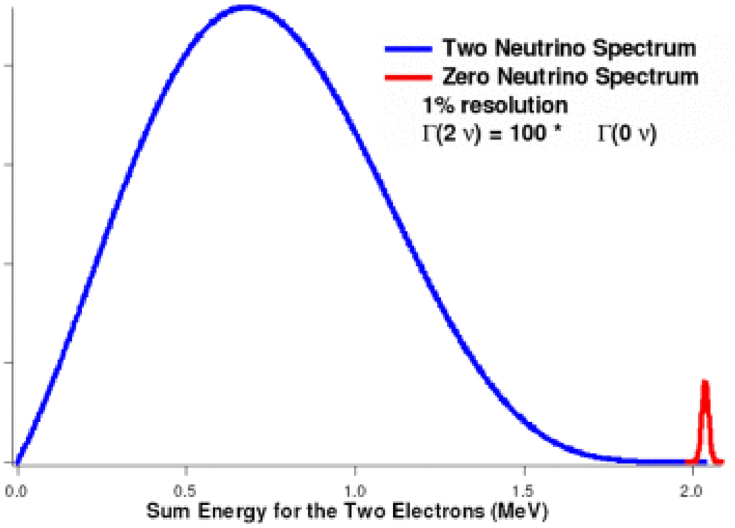

Figure 1.10: Comparison of the expected signals for $0\nu\beta\beta$ and $2\nu\beta\beta$ decays, as shown in Ref. [37]

The cylindrical part is divided in two symmetrical volumes separated by a cathode grid. A schematic of the EXO-200 detector is shown in Fig. 1.11.

The KamLAND-ZEN experiment

The KamLAND-ZEN detector stands for Kamioka Liquid Scintillator Antineutrino detector. It uses $\sim$ 400 kgs of ^{136}Xe enriched to 90%, dissolved in a liquid scintillator (made of mineral oil, benzene, and fluorescent chemicals). The scintillator fills inside an inner balloon located at the center of the detector [39]. The 13 m diameter outer balloon of the detector comprises a spherical tank that contains $\sim$ 1 kton of ultra-pure liquid scintillator material, which provides shielding from external radiation. A schematic of the

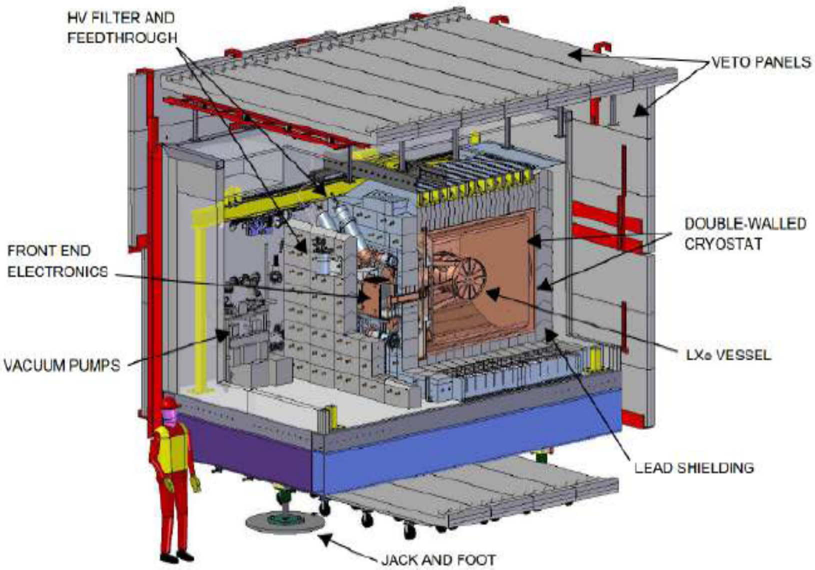
HV FILTER AND FEEDTHROUGH
VETO PANELS
DOUBLE-WALLED CRYOSTAT
FRONT END ELECTRONICS
LXe VESSEL
VACUUM PUMPS
LEAD SHIELDING
JACK AND FOOT

Figure 1.11: Schematic view of the EXO-200 detector. Figure taken from Ref. [38].

KamLAND-ZEN detector is shown in Fig. 1.12.

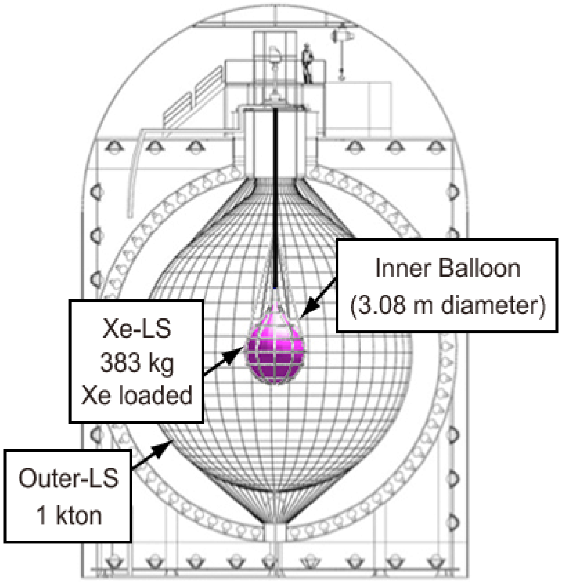
Inner Balloon
(3.08 m diameter)
Xe-LS
383 kg
Xe loaded
Outer-LS
1 kton

Figure 1.12: Schematic of the kamLAND-ZEN detector. Figure taken from Ref. [39].

After giving the necessary background of this work, let us get to the heart of this thesis. In the next chapter, I provide a discussion on direct nuclear reactions and I emphasize on the (p,t) reaction, which provides useful nuclear structure information relevant for the NME of $0\nu\beta\beta$.

Chapter 2

Direct nuclear reactions

The study of nuclear reactions plays an important role in nuclear physics as almost all properties of nuclei need to be measured using scattering, where in target nuclei are bombarded by particles from an accelerator or a radioactive substance[1]. It was Rutherford's experiment with α-particles scattering on a gold foil that provided experimental evidence of an atomic nucleus. In general, nuclear reactions can be classified in three different types, direct, pre-equilibrium, and compound reactions. These reaction mechanisms differ depending on the interaction time scales and the number of nucleons involved in the interaction between the incident particle and the target nucleus.

Direct reactions are said to occur when the projectile interacts with very few target nucleons, and the interaction occurs at very short time scales (10^{-21}-10^{-22}s). Direct reactions are generally useful to probe the shell effects in atomic nuclei, since they are selective to specific states resulting from the addition or removal of nucleons to (or from) a given orbital. Direct reactions allow one to extract information regarding the overlap between the wave functions of the target nucleus and the ground or particular excited states in the residual nucleus with the employment of simple models [40]. There are many types of direct reactions such as elastic scattering, inelastic scattering, nucleon transfer reactions, break-up reactions and charge-exchange reactions. Each of these reaction channels may be opened in a given experiment, depending on the specific beam energy. On the other hand, in a compound reaction, the interaction time-scale between the projectile and the target is much longer ($\approx 10^{-18}$s), and the reaction proceeds through many collisions before particle (or photon) emission. In such reactions, the projectile is captured by the target and its entire energy is distributed between the nucleons leading to the formation of a compound nucleus. The compound nucleus is usually formed in an excited state and can evaporate one or more particles (or lead to fission), etc. The de-excitation to the final products only depends on the energy, angular momentum and parity of the quantum state of the compound nucleus.

---

[1] In fact, even nuclear decays are described by a formalism that is very similar to scattering processes.

Finally, pre-equilibrium reactions are reaction mechanisms between direct and compound reaction processes. These reactions can be interpreted as multi-step direct reactions, so that particle emission occurs before the statistical equilibrium of the compound nuclear state is reached. In general, all three reaction types can occur with different probabilities. I shall spend much of this chapter discussing direct reactions, since this work employed a two-neutron transfer (p, t) reaction.

2.1 Scattering Theory

Reaction cross sections can be evaluated by solving the Schrödinger equation for a scattering process, given an interaction potential. This section provides a discussion on theoretical expressions for differential cross sections as a function of scattering angles. We start with the simplest description of a differential cross section in terms of the number of particles scattered and incident particles. We then introduce quantum mechanical approaches to derive an expression of differential cross sections in terms of scattering amplitudes of reaction outcomes, each outcome being described by its own set of partial-waves.

2.1.1 Differential Cross Section

Consider a collision experiment (figure 2.2) which involves measuring the number of scattered events in an element of solid angle $d\Omega$ in direction (θ, ϕ). If the incident flux of particles j_{inc} is defined as the number of particles per unit time crossing a unit area normal to direction of incidence, then the number of particles per unit time scattered into an element of $d\Omega$ is ($j_{scat} d\Omega$) proportional to the incident flux. The differential cross section can be defined as the ratio of the scattered flux (j_{scat}) to the incident flux (j_{inc}) [41].

$$\frac{d\sigma}{d\Omega} = \frac{j_{scat}}{j_{inc}} \tag{2.1}$$

The scattered flux j_{scat} is in units of number of particles per steradian per second. Thus, the differential scattering cross section $\frac{d\sigma}{d\Omega}$ is in units of area per steradian. If a detector subtends a surface A, and is placed at distance R

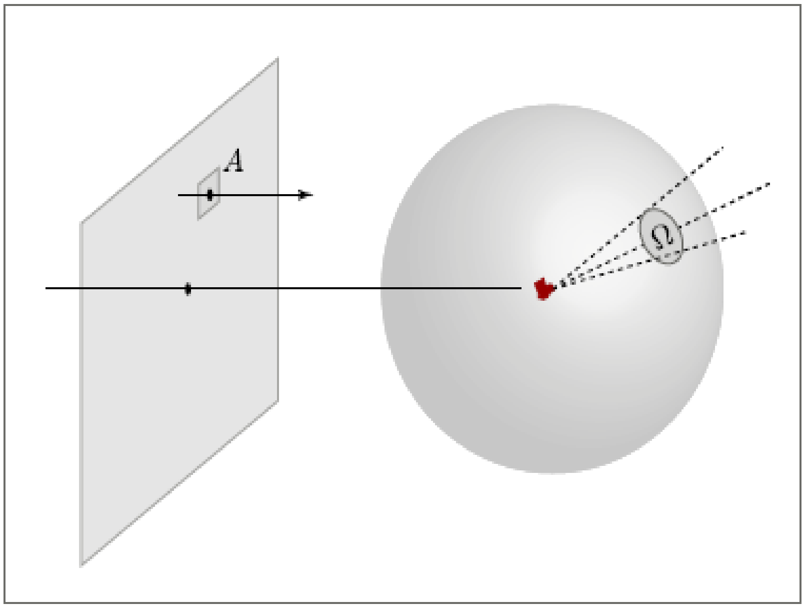

Figure 2.1: Scattering of a beam of particles into a solid angle Ω.

from the target, the total solid angle covered is $\Delta\Omega \simeq A/R^2$. One can obtain the total cross section by integrating the differential cross section over all $d\Omega$,

$$\sigma = \int \frac{d\sigma}{d\Omega} d\Omega. \tag{2.2}$$

A convenient unit of cross section is the barn (b), $1b = 10^{-28}\ m^2 = 100\ fm^2$.

2.1.2 Quantum mechanical theory of scattering

The Schrödinger equation for a central force scattering problem is given by

$$\left[-\frac{\hbar}{2\mu}\nabla^2 + V(r)\right]\psi(r) = E\psi(r) \tag{2.3}$$

where E is the total kinetic energy in the CM frame, $\mu = \frac{m_1 m_2}{m_1+m_2}$ is the reduced mass of the two particles, $V(r)$ is the potential that depends on the distance of the particles and $r = |\vec{r_1} - \vec{r_2}|$, where $\vec{r_1}$ and $\vec{r_2}$ represent vector positions of the projectile and target respectively.

If the incoming projectile has well defined energy, the incident wave function can be assumed to be a plane wave, with wave number $\vec{k}$, given by

$$\psi_{inc}(\vec{r}) = e^{i\vec{k}\cdot\vec{r}}. \tag{2.4}$$

The scattered wave function is obtained assuming that the interaction potential $V(r)$ is isotropic and short-ranged (falls faster than $1/r$). The outgoing waves are spherical with wave number $\vec{k'}$, expressed by [41]

$$\psi_{scat}(\vec{r}) = f(\theta, \phi)\frac{e^{i\vec{k'}\cdot\vec{r}}}{r}. \tag{2.5}$$

The general asymptotic wave function outside the interaction region, is a superposition of incident plane waves and scattered spherical waves,

$$\psi(\vec{r}) = \psi_{inc} + \psi_{scat} = e^{i\vec{k}\cdot\vec{r}} + f(\theta, \phi)\frac{e^{i\vec{k'}\cdot\vec{r}}}{r}. \tag{2.6}$$

In the above, the scattering amplitude $f(\theta, \phi)$, depends on the internal structure of the particles involved and can be expanded into a set of partial waves.

$$f(\theta, \phi) = \frac{1}{2ik}\sum_{l=0}^{\infty}(2l+1)(e^{2i\delta_l(k)} - 1)P_l(\cos\theta), \tag{2.7}$$

where $P_l(\cos\theta)$ are Legendre polynomials and $\delta_l(k)$ are the phase shifts.

The particle flux associated with ψ can be described as the probability current density, given by

$$\vec{j} = Re\left\{\psi^* \left(-\frac{i\hbar}{\mu}\nabla\right)\psi\right\}. \tag{2.8}$$

Therefore, using Eqs.(2.4) and (2.8), the incident flux can be rewritten as

$$j_i = \frac{\hbar k}{\mu}. \tag{2.9}$$

Similarly, Eqs.(2.5) and (2.8) show that the scattered flux can be expressed as

$$j_{scat} = \frac{\hbar k'}{\mu} \frac{|f(\theta, \phi)|^2}{r^2} + O(1/r^3), \tag{2.10}$$

expressed in paticles/area/second. In order to account for the solid angle coverage of the detector, the initial expression of the scattered flux must be integrated over a surface of a sphere, so that the scattered flux in terms of steradian/second is

$$j_{scat} = \frac{\hbar k'}{\mu} \frac{|f(\theta, \phi)|^2}{r^2} + O(1/r), \tag{2.11}$$

where the higher-order term $O(1/r)$ is neglected because it vanishes when r is very large.

The differential cross section can now be determined by substituting Eqs. (2.11) and (2.9) in Eq. (2.1)

$$\frac{d\sigma}{d\Omega} = \frac{k'}{k} |f(\theta, \phi)|^2, \tag{2.12}$$

where $k = \sqrt{2\mu E}/\hbar$. In the case of elastic scattering, since there is no change of energy (momentum), $k = k'$. The cross section is then simply reduced to

$$\frac{d\sigma}{d\Omega} = |f(\theta, \phi)|^2 = |f(\theta)|^2 \tag{2.13}$$

where the ϕ dependence redundant on account of the spherical symmetry.

In general, for an inelastic process, where the initial and final reduced masses are not necessarily equal, the differential cross section is expressed as

$$\left(\frac{d\sigma}{d\Omega}\right)_{i\to f} = \frac{\mu_i\mu_f}{(2\pi\hbar)^2}\left(\frac{k_f}{k_i}\right)|T_{if}|^2, \tag{2.14}$$

where T_{if} is the transition amplitude (or matrix element) between the initial (incident) and final (outgoing) channels.

2.1.3 Elastic Scattering

In general, the scattering potential in nuclei has contributions from both the short-range attractive nuclear potential and the long-range repulsive Coulomb potential.

For pure Coulomb interaction between the projectile with charge Z_p and target with charge Z_t, the potential is simply

$$V_C(r) = \frac{Z_pZ_te^2}{r}, \tag{2.15}$$

where r is the relative distance between the projectile and target nuclei. To simplify the problem, it is common to introduce a dimensionless Sommerfield parameter η, given by

$$\eta = \frac{Z_pZ_te^2\mu}{\hbar^2k} = \frac{Z_pZ_te^2\mu}{\hbar}\left(\frac{\mu}{2E}\right)^{\frac{1}{2}}, \tag{2.16}$$

with μ being the reduced mass and $E = \frac{\hbar^2k^2}{2\mu}$ is the energy of relative motion. The scattering amplitude can be expanded for this Coulomb interaction similarly as in Eq. (2.7)

$$f_C(\theta, \phi) = \frac{1}{2ik} \sum_{l=0}^{\infty} (2l+1)(e^{2i\delta_l^C(\eta)} - 1) P_l(\cos\theta), \tag{2.17}$$

where $\delta_l^C(\eta)$ is the Coulomb phase shift. Since the Coulomb potential does not go to zero fast enough for large r and the phase shift $\delta_l^C(\eta)$ is always non-zero, this series expression does not converge. In order for the series to have a physical meaning, a screened Coulomb potential is used instead. The point-source Coulomb scattering amplitude is defined so that the screened radius tends to infinity [41]. The asymptotic amplitude for such Coulomb scattering is given by

$$f_C(\theta) = -\frac{\eta}{2k\sin^2(\theta/2)}\, e^{\left(-i\eta\ln(\sin^2(\theta/2)) + 2i\delta_0^C(\eta)\right)}, \tag{2.18}$$

so that the point-source Coulomb scattering differential cross section is

$$\left.\frac{d\sigma}{d\Omega}\right|_c = |f_c(\theta)|^2 = \frac{\eta^2}{4k^2\sin^4(\theta/2)}, \tag{2.19}$$

the Rutherford scattering cross section.

If the beam energy is sufficiently above the Coulomb barrier, the interaction will include both the nuclear potential and the Coulomb potential,

$$V(r) = V_C(r) + V_N(r), \tag{2.20}$$

so that the total phase shift for scattering off $V(r)$ will be composed of both Coulomb $\delta_l^C(\eta)$ and nuclear δ_l^N phase shifts,

$$\delta_l = \delta_l^C(\eta) + \delta_l^N. \tag{2.21}$$

The scattering amplitude is naturally the sum of Coulomb and nuclear amplitudes,

$$f_{NC}(\theta) = f_C(\theta) + f_N(\theta). \tag{2.22}$$

The $f_N(\theta)$ also includes the effects of Coulomb distortion on the nuclear potential, so that [41],

$$f_N(\theta) = \frac{1}{2ik}\sum_{l=0}^{\infty}(2l+1)\, e^{2i\delta_l^C(\eta)}(\, e^{2i\delta_l^N(\eta)} - 1)P_l(\cos\theta). \tag{2.23}$$

Therefore, the differential cross section for a combination of Coulomb and nuclear scattering is

$$\left.\frac{d\sigma}{d\Omega}\right|_{NC} = |f_{NC}(\theta)|^2 = |f_N(\theta) + f_C(\theta)|^2. \tag{2.24}$$

2.2 The Distorted-Wave Born Approximation

Because of the complexity in solving the Schrödinger equation for a scattering in Coulomb and nuclear potential, some approximations need to be taken into account in order to evaluate transition matrix elements. The Born approximation is a useful tool to simplify the calculation of the transition amplitudes between the initial and final systems. Assuming that reaction procees $A(a,b)B$ is caused by an interaction potential V, the transition amplitude between two channels (entrance and exit) can be calculated using an approximation known as the distorted-wave Born approximation (DWBA)[42]. This approximation is the most useful one in the direct nuclear reaction theory and remains valid as long as the interaction potential is sufficiently weak.

The transition amplitude for the reaction $A(a,b)B$ under the DWBA is given as

$$T_{DWBA} = \int d^3r_b d^3r_a \chi^{(-)}(\overrightarrow{k}_f, \overrightarrow{r}_b)^* \langle \psi_B\psi_b|V|\psi_A\psi_a\rangle \chi^{(+)}(\overrightarrow{k}_i, \overrightarrow{r}_a), \quad (2.25)$$

where $\chi^{(-)}$ and $\chi^{(+)}$ are the distorted waves, $\overrightarrow{r}_a$ and $\overrightarrow{r}_b$ are the relative coordinates for the initial system (a,A) and final system (b,B), respectively. The quantity $\langle \psi_B\psi_b|V|\psi_A\psi_a\rangle$ is the nuclear matrix element and can be as series expansion in terms of spherical harmonics [43],

$$\langle \psi_B\psi_b|V|\psi_A\psi_a\rangle = \sum_{L,M} f_l Y_L^M(\theta,\phi). \quad (2.26)$$

The distorted waves $\chi^{\pm}(\overrightarrow{k}, \overrightarrow{r})$ asymptotically describe a plane wave of wave vector $\overrightarrow{k}$ plus an outgoing (or incoming) spherical scattered wave, which in the case of a $1/r$ potential has the form [44],

$$\chi^{\pm}(\overrightarrow{k}, \overrightarrow{r}) = e^{i\overrightarrow{k}\overrightarrow{r}} + f(\theta)\frac{e^{\pm i\overrightarrow{k}\overrightarrow{r}}}{r}. \quad (2.27)$$

The distorted waves which has an incoming and outgoing spherical waves are connected by [44],

$$\chi^{(-)*}(\overrightarrow{k}, \overrightarrow{r}) = \chi^{(+)}(-\overrightarrow{k}, \overrightarrow{r}). \quad (2.28)$$

2.3 Optical Model Potential

We saw in Section 2.2 how in a direct nuclear reaction the initial and final systems are connected via an interaction potential. This potential is not explicitly defined for the case of the nucleon-nucleus interaction. Due to the complexity of the many-body system in the nucleus, the interaction between each nucleon of the projectile and each nucleon of the target can be described in term of an average potential $U(r)$ experienced by a single nucleon with the rest of the nucleus. This approximation results in an *optical model potential* (OMP), which by definition has two components

$$U(r) = V(r) + iW(r), \tag{2.29}$$

where $V(r)$ represents the real part of the potential and $W(r)$ represents the imaginary part of the potential, which takes into account the absorption effects. The *optical model potential* only considers the relative motion within a reaction channel. The appropriate OMP is thus determined by an adjustment of its parameters to the experimental data. The optical potential is composed of three parts: the volume part, the surface part, and the spin-orbit part of interaction. The Coulomb term is also taken into account in the case of charged projectiles. Therefore, the optical potential is the sum

$$\begin{aligned} U(r) = & -V_v f_v(r, R_v, a_v) - iW_v f_w(r, R_w, a_w) \\ & + i4W_s a_s \frac{d}{dr} f_s(r, R_s, a_s) \\ & + \lambda_\pi^2 \frac{(V_{so} + iW_{so})}{r} \frac{d}{dr} f_{so}(r, R_{so}, a_{so}) \vec{\sigma} \cdot \vec{l} \\ & + V_C(r), \end{aligned} \tag{2.30}$$

where λ_π is the pion Compton wavelength, $\lambda_\pi^2 \approx 2$. In the above the Woods-

Saxon form factor is defined as

$$f(r, R_i, a_i) = \left[1 + \exp\frac{(r - R_i)}{a_i}\right]^{-1}. \tag{2.31}$$

This factor takes into consideration that the nuclear density is almost constant in the interior of the nucleus ($r < R$) and falls smoothly to zero outside for $r > R$ [42]. The V_i, W_i, and r_i terms are the parameters to be determined by fitting the DWBA predictions to elastic scattering data. In the above $R_i = r_i A^{1/3}$ is the radius of the nucleus and a_i is the diffuseness of the potential. The Coulomb potential between the projectile with charge Z_p and target with charge Z_t is given by

$$V_C(r) = \begin{cases} \frac{Z_p Z_t e^2}{2R}\left(3 - \frac{r^2}{R^2}\right), & r \leq R, \\ \frac{Z_p Z_t e^2}{r}, & r > R \end{cases} \tag{2.32}$$

where R is the nuclear charge radius, $R = r_c A^{1/3}$.

2.4 Two-Body Nuclear Reaction Kinematics

In this section I discuss the kinematics of the two-body nuclear reactions with light projectiles (p, n, d, t, or α). The interaction produces an ejectile, which is a scattered projectile-like particle, and a recoil, which is a target-like nucleus. Generally, the central goal of the reaction is to analyze the ejectile distribution and use that to probe the nuclear structure of the recoiling nucleus.

The general notation used to describe such a nuclear reaction is:

$$a + A \longrightarrow B + b. \tag{2.33}$$

Another shorthand way to denote the nuclear reaction is $A(a,b)B$. In the above, a is the projectile, A is the target, B is the recoil, and b is the ejectile. The reaction presented in this thesis is

$$p + {}^{136}\mathrm{Ba} \longrightarrow {}^{134}\mathrm{Ba} + t \tag{2.34}$$

also shown as ${}^{136}\mathrm{Ba}(p,t){}^{134}\mathrm{Ba}$.

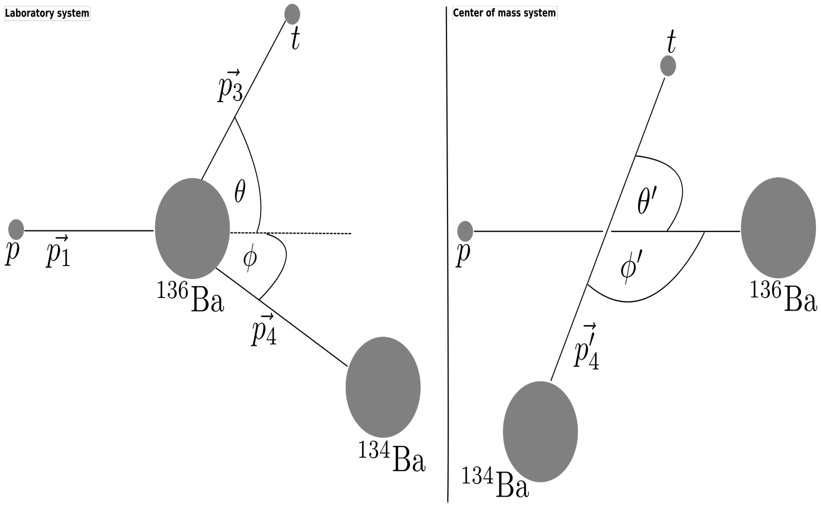
Laboratory system
t
$\vec{p_3}$
θ
p
$\vec{p_1}$
ϕ
^{136}Ba
$\vec{p_4}$
^{134}Ba
Center of mass system
t
θ'
p
ϕ'
^{136}Ba
$\vec{p'_4}$
^{134}Ba

Figure 2.2: A graphic representation of two-body kinematics for the reaction ${}^{136}\mathrm{Ba}(p,t)$ in the laboratory coordinate system (left side) and the center-of-mass coordinate sytem (right side).

Below I derive the kinematics for a two body reaction.

Consider m_1, m_2, m_3, and m_4 the rest masses of projectile, target, ejectile, and recoil nuclei, respectively. Momentum conservation leads to the equations,

$$p_1 = p_3 \cos\theta + p_4 \cos\phi \tag{2.35}$$

$$0 = p_3 \sin\theta - p_4 \sin\phi. \tag{2.36}$$

Similarly, energy conservation can be written as

$$E_1 + m_2c^2 + Q = E_3 + E_4 + E_x = E_{tot} + E_x \tag{2.37}$$

where $E = T + mc^2$ and $E^2 = p^2c^2 + m^2c^4$. T represents the kinetic energy and E is the total energy (kinetic + rest-mass energy). The reaction Q-value is defined as $Q = [m_1 + m_2 - (m_3 + m_4)]\, c^2$, and the laboratory scattering angles of ejectile are determined from experiment.

The minimum kinetic energy required by the projectile so that the reaction proceeds is the threshold kinetic energy $W_{th} = -\frac{Q}{2m_2}(m_1+m_2+m_3+m_4)$ [45]. Squaring Eq (2.35) and Eq (2.36), we get

$$(p_1 - p_3\cos\theta)^2 = p_4^2\cos^2\phi \tag{2.38}$$

$$p_3^2\sin^2\theta = p_4^2\sin^2\phi. \tag{2.39}$$

Summing Eq (2.38) and Eq (2.39) results in

$$p_1^2c^2 + p_3^2c^2 - 2p_1p_3c^2\cos\theta = p_4c^2, \tag{2.40}$$

while substituting $p_4^2c^2 = (E_{tot} - E_3)^2 - m_4^2c^4$ into Eq (2.40) leads to

$$p_1^2c^2 + p_3^2c^2 - 2p_1p_3c^2\cos\theta = (E_{tot} - E_3)^2 - m_4^2c^4 = E_{tot}^2 + E_3^2 - 2E_{tot}E_3 - m_4^2c^4 \tag{2.41}$$

$$\Rightarrow p_1^2c^2 + E_3^2 - m_3^2c^4 - 2p_1p_3c^2\cos\theta + m_4^2c^4 - E_3^2 = E_{tot}^2 - 2E_{tot}E_3 \tag{2.42}$$

$$\Rightarrow 2p_1p_3c^2\cos\theta = (m_4^2c^4 - m_3^2c^4) + p_1^2c^2 + 2E_{tot}E_3 - E_{tot}^2. \tag{2.43}$$

Squaring Eq (2.43), one obtains

$$4(E_3^2 - m_3^2)(p_1c)^2\cos^2\theta = \left[(m_4^2c^4 - m_3^2c^4) + p_1^2c^2 + 2E_{tot}E_3 - E_{tot}^2\right]^2. \tag{2.44}$$

Further grouping the terms of Eq (2.44), one obtains the quadratic equation for E_3

$$\begin{aligned}&(4p_1^2c^2\cos^2\theta - 4E_{tot}^2)E_3^2 + \left(4E_{tot}^3 + 4E_{tot}p_1^2c^2 + 4m_3^2c^4E_{tot} - 4m_4^2c^4E_{tot}\right)E_3\\ &+ 2p_1c^2E_{tot}^2 - 2m_3^2c^4E_{tot}^2 + 2m_3^2c^4p_1^2c^2 + 2m_4^2c^4E_{tot}^2 - 2m_4^2c^4p_1^2c^2 + 2m_3c^4m_4^2c^4\\ &- E_{tot}^4 - p_1^4c^4 - m_3^4c^8 - m_4^4c^8 - 4m_3^2c^4p_1^2c^2\cos^2\theta = 0.\end{aligned} \tag{2.45}$$

This equation can be trivally solved so that once the laboratory energy of ejectile is known, the remaining quantities can be easily determined [45],

$$T_3 = E_3 - m_3c^2 \tag{2.46}$$

$$p_3 = \frac{1}{c}\left(E_3^2 - m_3^2c^4\right)^{1/2} \tag{2.47}$$

$$E_4 = E_{tot} - E_3 \tag{2.48}$$

$$T_4 = E_4 - m_4c^2 \tag{2.49}$$

$$p_4 = \frac{1}{c}\left(E_4^2 - m_4^2c^4\right)^{1/2} \tag{2.50}$$

$$\phi = \arcsin\left(\frac{p3}{p4}\sin\theta\right). \tag{2.51}$$

The kinematic equations in the centre-of-mass frame are similarly,

$$E'_{tot} = \left(m_1^2c^4 + m_2^2c^4 + 2m_2c^2E_1\right)^{1/2} \tag{2.52}$$

$$p'_1 = p'_2 = \frac{p_1m_2c^2}{E'_{tot}} \tag{2.53}$$

$$E'_1 = \frac{m_1^2c^4 + m_2c^2E_1}{E'_{tot}} \tag{2.54}$$

$$E'_2 = \frac{m_2^2c^4 + m_2c^2E_1}{E'_{tot}} \tag{2.55}$$

$$E'_3 = \frac{E'^2_{tot} + m_3^2c^4 - m_4^2c^4}{2E'_{tot}} \tag{2.56}$$

$$E'_4 = \frac{E'^2_{tot} + m_4^2c^4 - m_3^2c^4}{2E'_{tot}} \tag{2.57}$$

$$p'_3 = \frac{1}{c}\left(E'^2_3 - m_3^2c^4\right)^{1/2} \tag{2.58}$$

$$p'_4 = \frac{1}{c}\left(E'^2_4 - m_4^2c^4\right)^{1/2} \tag{2.59}$$

$$\theta' = \arcsin\left(\frac{p_3}{p_3'}\sin\theta\right) \tag{2.60}$$

$$\phi' = 180^\circ - \theta' \tag{2.61}$$

2.5 Two-nucleon transfer reactions

Two-nucleon transfer reactions occur when a pair of nucleons is added (or removed) to or from the target nucleus during the reaction. The pair of transferred nucleons that is transferred can be either composed of two like-nucleons or one proton and one neutron, then the reaction cross sections depend on the correlations between the transferred nucleons from various orbitals. Since this thesis describes the two neutron transfer ^{136}Ba(p,t) reaction, below I discuss briefly two-neutron transfer reactions and their relevance for the study of pairing in nuclei.

Particle-particle pairing correlations between nucleons play an important role in the structural considerations for atomic nuclei. In particular the pairing forces between nucleons are an important constituent in the residual part of the nucleon-nucleon interaction described in section 1.5.2. Two nucleon transfer reactions such as the (t,p), (p,t) and (^{3}He,n) reactions are important probes of pairing correlations in nuclei. If one assumes the two transfered nucleons are in a relative $L=0$ (s-wave) state, then the $L=0$ orbital angular momentum transfer strength to 0^+ states in the residual nucleus would test the BCS approximation used in QRPA calculations. For fully coherently paired system of like nucleons the BCS theory is valid and the nucleons can be assumed to be in a superfluid state of paired bosons. In such a scenario one would expect significant strength connecting the 0^+ ground states of the target and residual nuclei [46]. However, a large breakdowns of this approximation (from the superfluid limit) can occur due to the onset of a shell gap or changes in deformation between the initial and final state nuclei. Such a scenario would require a reassessment of the BCS approximation in QRPA calculations. Below I discuss the selection rules for the (p, t) reaction in this context.

In a (p, t) reaction, if the total orbital and spin angular momenta of the two transferred neutrons are J_1, L_1, S_1, and J_2, L_2, S_2 respectively, the allowed angular momentum values for a two nucleon transfer reaction will be as follows

$$J_R = J_T + L + S = J_T + J, \tag{2.62}$$

so that

$$|J_T - J_R| \leq J \leq J_T + J_R. \tag{2.63}$$

In the above, J_T and J_R are the angular momenta of the target and residual nucleus respectively, and J is the total angular momentum transferred by the two nucleons. Let us discuss the (p, t) reaction on an angular momentum $J^\pi = 0^+$ even-even nucleus which is relevant for this thesis. Since the two neutrons picked up mainly couple to $S = 0$ as it is the more energetically favorable configuration. Therefore, the selection rule for (p, t) reaction on an even-even nucleus (with $J^{\pi} = 0^{+}$) results in

$$J_R = L. \tag{2.64}$$

The multiplicative conservation rule of parity shown in Eq. (1.15) will further result in

$$\pi_R \pi_T = (-1)^L. \tag{2.65}$$

$L = J_R$, only natural parity states (0^+, 1^-, 2^+, 3^- etc) would be populated in such reactions. In the following experimental and analysis chapters I discuss the procedures that we employed to perform the spectroscopy of states in ^{134}Ba, using a ^{136}Ba(p,t) two neutron transfer reaction.

Chapter 3

Experimental Setup and Data Analysis

In this chapter I describe the experimental apparatus and the data analysis methods used to both obtain and analyse the ^{136}Ba(p,t) data. For the purpose of this experiment, a 2μA 22 MeV proton beam was incident on a 40 $\mu g/cm^2$ ^{136}BaO target that was isotopically enriched to 93% and evaporated on a carbon foil which had a thickness of 30 $\mu g/cm^2$. A more detailed description is below.

3.1 Experimental Setup

3.1.1 Facility

The experiment was performed at the Maier Leibnitz Laboratory (MLL), located on the joint campuses of the Ludwig-Maximilian Universität (LMU) and Technische Universität München (TUM) in Garching, Germany. The MLL has a 14 MV Tandem Van de Graaff accelerator which can provide polarized and unpolarized stable light ion beams (Fig. 3.1).

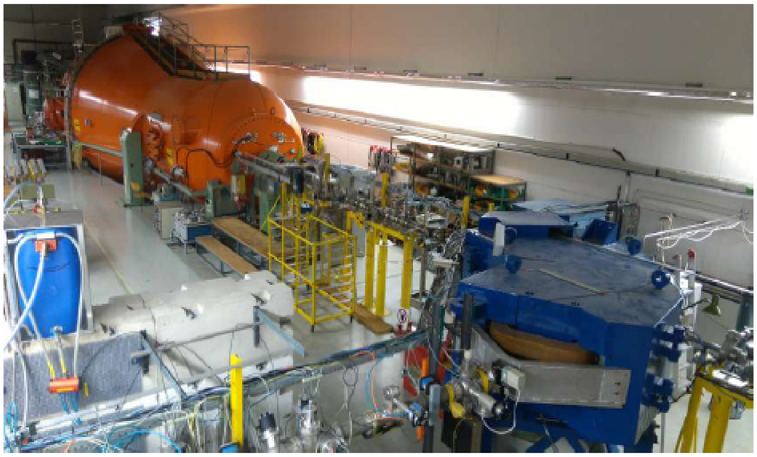

Figure 3.1: A photograph of the tandem hall at MLL, showing the tandem Van de Graaff accelerator (orange) and the 90° analyzing magnet (blue).

3.1.2 Ion source

The Stern-Gerlach negative ion source at MLL (shown in Fig. 3.2) is a source that uses the electron cyclotron resonance (ECR) method of ionization. The negative ion beams are obtained using the ionization process in two steps. In the first step, the hydrogen atoms are singly ionized within the ECR plasma, resulting in positively charged H^+ ions. This single electron stripping process has an efficiency of a few percent. In the second step, the hydrogen ions pass through cesium vapour where they pick up two electrons, resulting in negatively charged H^- ions. The efficiency of the second step is about 30%.

The ion source generates high-intensity unpolarized H^- beams which are then directed towards the tandem accelerator.

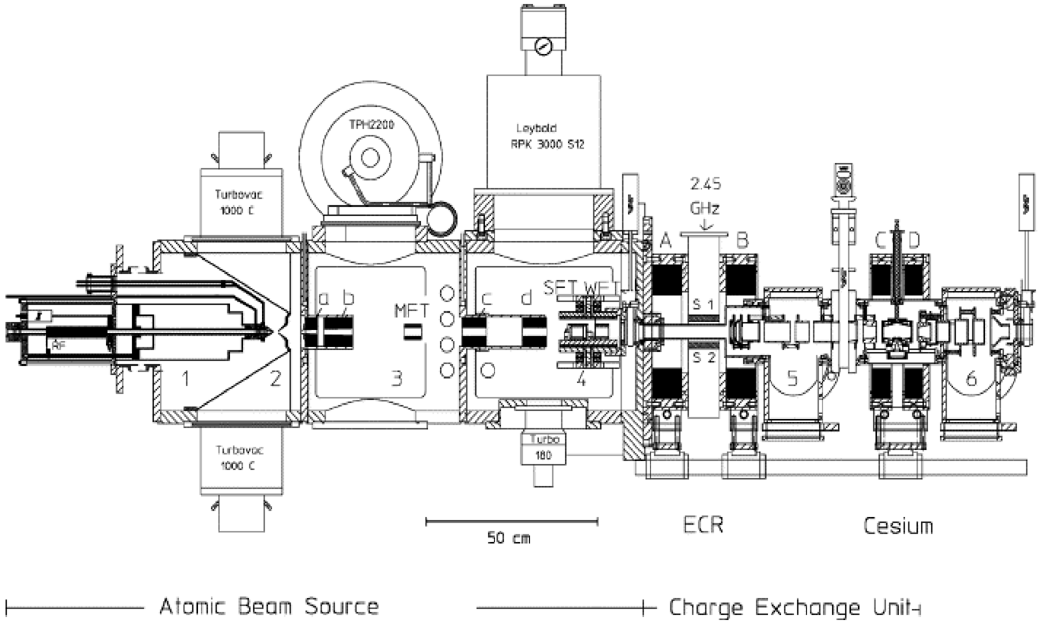
TPH2200
Leybold RPK 3000 S12
Turbovac 1000 C
2.45 GHz
A
B
C
D
RF
a
b
MFT
c
d
SFT
WFT
S 1
S 2
1
2
3
4
5
6
Turbovac 1000 C
Turbo 180
50 cm
ECR
Cesium
Atomic Beam Source
Charge Exchange Unit

Figure 3.2: Scheme of the Stern-Gerlach ion source at MLL, figure taken from Ref. [47].

3.1.3 Tandem Van de Graff accelearator

The tandem accelerates charged ions in two stages by using a single terminal high voltage. The H^- ions are first towards the positive high-voltage (HV) terminal at the center of the tank. At the center of the tandem tank, they pass through a thin carbon stripping foil, that strips off the electrons making positively H^+ ions. The resulting ions are thus accelerated away from the central positive potential, providing a second stage of acceleration. After exiting the accelerator, the ions are steered by a 90° analyzing magnet that directs them towards the Q3D hall. The trajectories of the ions are determined by

$$R = B\rho = \frac{mv}{q}, \tag{3.1}$$

where B, ρ, mv, and q are the magnetic field, the gyroradius of the particle, the momentum of particle, and the charge of particle respectively. The analyzing magnet selects a specific energy of the beam to be sent to the Q3D. To control the energy of the beam, a feedback system is set up right after the analyzing magnet. The system is made of a pair of slits that reads the currents on both the left and the right slit. If the beam energy is lower or higher than required, the system will read more current on one compared to the other and the voltage is then adjusted to correct the beam energy. This combination results in a very stable beam with an energy spread of $\Delta E/E$ $\leq 10^{-4}$. A schematic view of the different stages of tandem acceleration is shown in Fig. 3.3 .

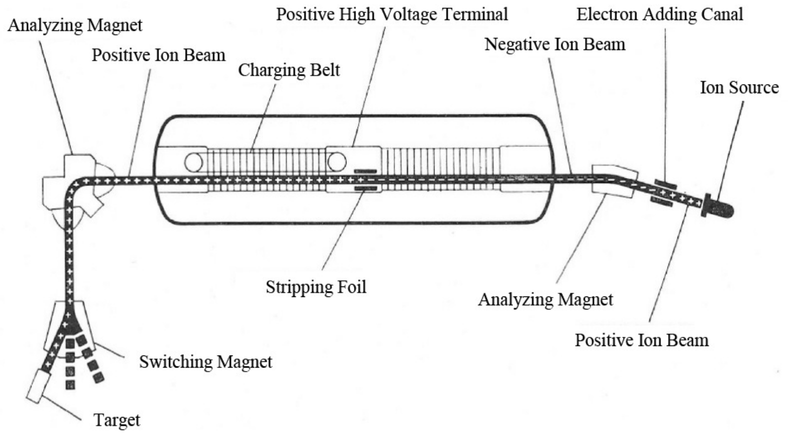
Analyzing Magnet
Positive Ion Beam
Positive High Voltage Terminal
Charging Belt
Electron Adding Canal
Negative Ion Beam
Ion Source
Stripping Foil
Analyzing Magnet
Positive Ion Beam
Switching Magnet
Target

Figure 3.3: Schematic picture of a tandem Van de Graaff accelerator.

3.1.4 Q3D Magnetic Spectrograph

The Q3D is a high resolution magnetic spectrograph, composed of three dipole magnets, a quadrupole magnet and a multipole magnet. The dipole magnets deflect light charged ejectiles from reactions such as $^{136}\mathrm{Ba}(p,t)$ and they provide a way to do rigidity selection, while the quadrupole magnet is used to provide vertical focus onto the focal plane. The radius of the charged particle in the magnetic field is given by Eq (3.1). A computer program is used to set the desired value of magnetic field according to the reaction and measurement angles. The spectrograph sits on a semi-circular iron rail which allows it to be rotated to different laboratory angles relative to the beam axis. A schematic of the Q3D magnetic spectrograph is shown in Fig. 3.4 and a picture in Fig. 3.5.

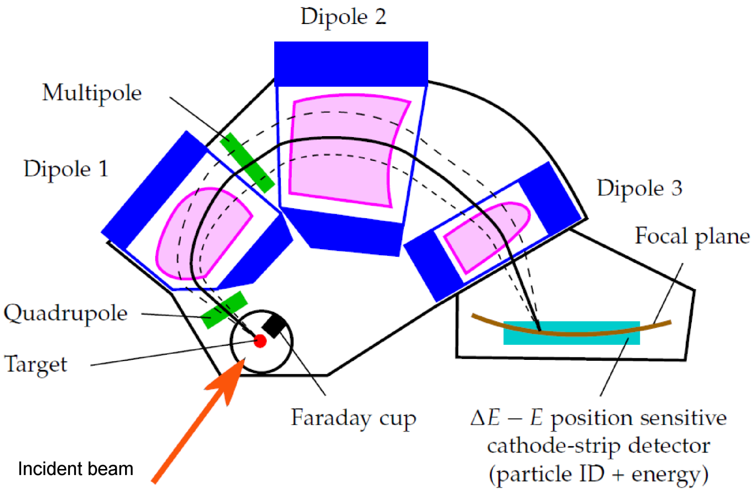
Dipole 2
Multipole
Dipole 1
Dipole 3
Focal plane
Quadrupole
Target
Faraday cup
$\Delta E - E$ position sensitive cathode-strip detector (particle ID + energy)
Incident beam

Figure 3.4: The Q3D magnetic spectrograph, illustrating the trajectory of a light charged ejectile to the focal plane.

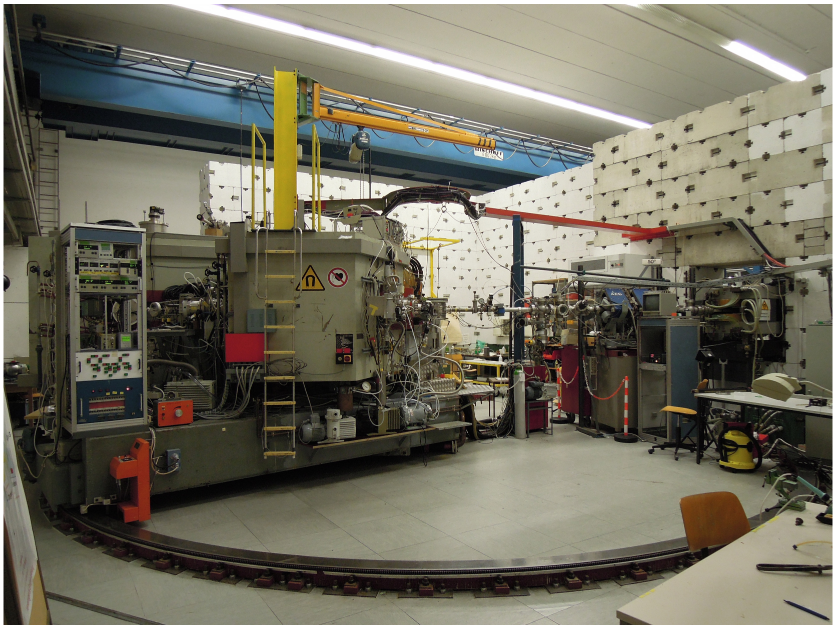

Figure 3.5: The Q3D vault at MLL.

3.1.5 Focal plane detector

The focal plane detector of the spectrograph is comprised of two proportional counters and a plastic scintillator. Each proportional counter is filled with isobutane gas at $\sim$ 500 mbar. The first proportional counter comprises of two cathode foils and a single anode wire at the center. The second proportional counter is made of one cathode foil, one cathode-strip foil and two anode wires positioned such that one is vertically above the other to ensure that the number of events on each wire is approximately the same. The cathode-strip foil is composed of 272 strips, each 3 mm wide and separated by 0.5 mm, which precisely determine the positions of the ejectiles along the focal plane.

The 7 mm thick plastic scintillator is coupled to photo-multiplier tubes

(PMTs), which convert the light from scintillator into electrical pulses.

When the charged ejectiles travel inside the two proportional counters, they lose energy by ionizing the gas. The free electrons caused by this ionization move towards the anode wire, so that the electric field around the anode gives the electrons enough energy to create further electron-ion pairs. An electron avalanche is consequently induced close to the wire. The total amount of charge collected on the wire in the first counter is proportional to the energy lost ΔE_1. A similar process occurs for the second counter. The positive charge resulting from the avalanche hit the cathode-strip foil. This contributes an event that is registered by the data acquisition system. A schematic view of the detector is shown in Fig. 3.6.

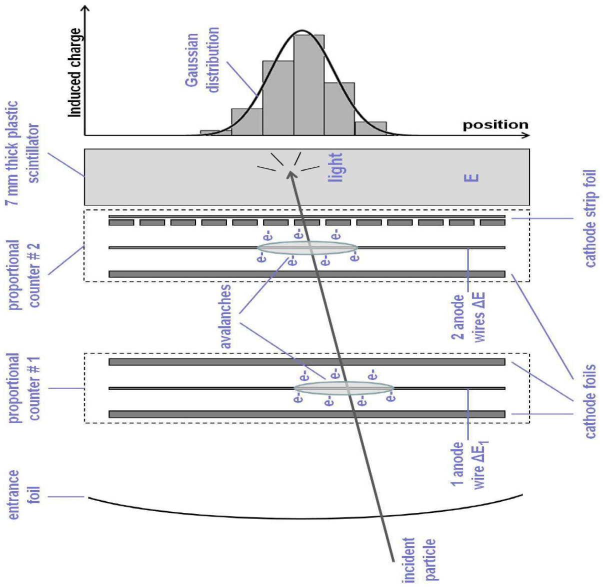
Induced charge
Gaussian distribution
position
7 mm thick plastic scintillator
light
E
cathode strip foil
proportional counter # 2
e-
avalanches
2 anode wires ΔE
proportional counter # 1
cathode foils
1 anode wire ΔE_1
entrance foil
incident particle

Figure 3.6: Schematic diagram of the focal plane detector at the Q3D spectrograph as shown in Ref. [48].

3.2 Data Analysis

The data presented in this thesis were collected using five momentum settings for the spectrograph, ranging up to an excitation energy of 3.4 MeV. The laboratory scattering angle was varied between 5° and 60° in increments 5° over the course of the experiment.

3.2.1 Particle identification

Since multiple ^{136}Ba+p nuclear reaction channels open up in the experiment and the focal plane detector would detect all charged ejectiles within the regidity acceptance, in order to ensure that we collect data only from the reaction of interest, specific particle identification (PID) gates are required for analyzing the data. In most Q3D experiments, two PID gates are set. The first gate is set by comparing the energy lost (ΔE_1 vs ΔE_2) in the two proportional counters. The second gate is set by comparing the energy lost in the second proportional counter with the energy deposited on the plastic scintillator (ΔE_2 vs E). The 2-dimensional histograms showing both these PID gates for the ^{136}Ba(p, t) reaction are shown in Fig 3.7.

3.2.2 Peak fitting

Each triton peak within the spectrum represents a state populated in the recoil nucleus and the number of counts under a peak represents the probability for populating that nuclear state. We used a Levenberg-Marquardt [49] χ^2 minimization method to perform the peak fitting to extract peak centroids and areas. The lineshape function used to fit the peaks was the convolution

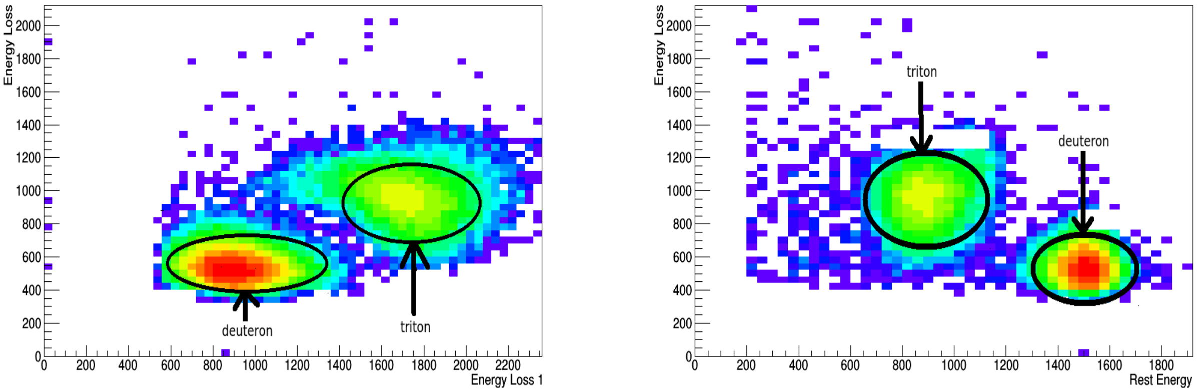

Figure 3.7: Left panel: particle identification, ΔE_1-ΔE_2 plot showing the partial energy loss of ejectiles in the two proportional counters. Right panel: ΔE_2-E plot showing the ejectiles' energy loss in the second proportional counter and total energy deposited on the plastic scintillator.

of a Gaussian with a low energy exponential tail, on a flat background [50]. The low energy tail is necessary to take into account the energy straggling of the ejectiles through the target material and the focal plane detector.

3.2.3 Energy calibration

We first identified the triton peaks corresponding to excited states in ^{134}Ba using a very rough energy calibration. Once identified, the momentum for each triton group was calculated using Eq (2.47) in Section 2.4. Since the focal plane of the Q3D spectrograph is curved, we used a quadratic relation between the momentum (P) and centroid of the peak on the focal plane (x).

$$P(x) = (A + Bx + Cx^2). \tag{3.2}$$

Table 3.1: Polynomial fit parameters for the energy calibration in each momentum setting.

Fitting Parameters	MB1	MB2	MB3	MB4	MB5
A	273.372	266.525	258.426	250.095	241.482
B	0.0138061	0.0175375	0.0170596	0.0167728	0.0156578
C		-3.58x10^{-6}	-3.54x10^{-6}	-3.64x10^{-6}	-3.06x10^{-6}

Here A, B and C are the coefficients obtained for each momentum setting. We used a modified χ^2 description to account for uncertainties in both the x and y coordinates [51], so that

$$\chi^2 = \sum_{i=1}^{N} \frac{[y_i - y_{fit}(x_i)]^2}{\left(\sigma_{y_i}^2 + \sigma_{x_i}^2 \frac{dy_{fit}(x_i)^2}{dx}\right)}. \tag{3.3}$$

In the above, the coordinates (x, y) represent the focal plane centroids and momenta, and (σ_x, σ_y) represent their associated uncertainties. The minimization was performed using ROOT program [52] and the MINUIT library [53] to obtain the coefficients of Eq (3.2). The resulting coefficients are listed in Table 3.1, for all momentum settings used in this experiment. These coefficients were used to convert focal plane centroids to triton momenta. The corresponding excitation energies were then back calculated using the reaction kinematics described in Section 2.4.

3.2.4 Uncertainties in excitation energy calculations

In addition to the statistical uncertainties, systematic uncertainties also contribute to add to the total uncertainty in extracted excitation energies. The first contribution arises from the uncertainty in beam energy ($\Delta E/E \leq 10^{-4}$). The second comes from the uncertainty in masses of the nuclei involved in the reaction, and the last one[1] is due to the angular acceptance of the Q3D as a function of X-slit width. The uncertainty ($\Delta\theta$) due to the angular acceptance of the Q3D is

$$\Delta\theta = \tan^{-1}\left(\frac{\Delta X}{R}\right), \tag{3.4}$$

where R is the distance from the the aperture to the target chamber. The total uncertainties in the excitation energies are then added in quadrature so that

$$\Delta E_x = \sqrt{(\Delta E_{stat})^2 + (\Delta E_{beam})^2 + (\Delta E_{mass})^2 + (\Delta E_{Q3D})^2} \tag{3.5}$$

where ΔE_{stat}, ΔE_{beam}, ΔE_{mass}, and ΔE_{Q3D} are the uncertainties due to statistics, beam energy, nuclear masses, and the Q3D angular acceptance.

3.2.5 Cross section determination

The measured laboratory differential scattering cross section was determined using the formula

$$\left(\frac{d\sigma}{d\Omega}\right)_{lab} = \frac{N_c}{N_t N_b \Omega LT_{DAQ} LT_{DET}}.10^{34}\left[\frac{mb}{sr}\right], \tag{3.6}$$

where N_c is the number of counts in a given peak, N_b is the number of beam particles incident on the target, Ω is the solid angle acceptance of Q3D,

---

[1] To the lowest order, uncertainties due to the target thickness can be ignored as well known states in ^{134}Ba were used as an intrinsic calibration.

LT_{DAQ} and LT_{DET} are corrections due to the live-times associated to the DAQ and detector, and N_t is the number of target nuclei. The number of ^{136}Ba nuclei in the target were determined from elastic scattering data as discussed in Section 3.2.7.

The cross sections were determined at different Q3D angles, and the angular distributions were obtained for the purpose of comparison between theoretical DWBA predictions and experimental data. Since the theoretical cross sections are calculated in the centre-of-mass frame, a transformation from lab frame to the centre-of-mass frame for both the angles and the $(\frac{d\sigma}{d\Omega})$ values was necessary.

3.2.6 Laboratory to centre-of-mass (CM) frame transformations

Since our experiment was performed with a proton beam energy of 22 MeV, non-relativistic equations can be applied for the transformation from the laboratory frame to the CM frame. The position of centre-of mass is given by

$$\vec{R}_{cm} = \frac{m_1\vec{r}_1 + m_2\vec{r}_2}{M} \tag{3.7}$$

where m_1, m_2 are described in Section 2.4, $\vec{r}_1$, $\vec{r}_2$ are the positions of projectile and target respectively and the total mass is $M = m_1 + m_2$. In the laboratory frame, the projectile velocity is $\overrightarrow{V_1}$, and the target is at rest. From Eq. (3.7), the centre-of-mass velocity is simply

$$\vec{v}_{cm} = \frac{m_1}{m_1 + m_2}\vec{V}_1. \tag{3.8}$$

Referring to Fig 2.2 in Section 2.4, one obtains

$$\vec{V}_3 = \vec{v}_3 + \vec{v}_{cm}. \tag{3.9}$$

Therefore by making projections into parallel and perpendicular components along the beam direction, one obtains

$$V_3 \sin\theta_{lab} = v_3 \sin\theta_{cm} \tag{3.10}$$

$$V_3 \cos\theta_{lab} = v_3 \cos\theta_{cm} + v_{cm}. \tag{3.11}$$

From Eq. (3.10) and Eq. (3.11), one can get the relationships

$$\tan\theta_{lab} = \frac{\sin\theta_{cm}}{\cos\theta_{cm} + v_{cm}/v_3} = \frac{\sin\theta_{cm}}{\cos\theta_{cm} + \gamma} \tag{3.12}$$

and

$$\cos\theta_{lab} = \frac{\gamma + \cos\theta_{cm}}{\sqrt{1 + \gamma^2 + 2\gamma\cos\theta_{cm}}}. \tag{3.13}$$

Furthermore, the relationship between the centre of mass angle and the laboratory angle is given by [54]

$$\theta_{cm} = \sin^{-1}\left(\gamma\sin(\theta_{lab})\right) + \theta_{lab}, \tag{3.14}$$

where

$$\gamma \approx \sqrt{\frac{m_1 m_3}{m_2 m_4}\left(\frac{1}{1+(1+\frac{m_1}{m_2})\frac{Q}{E}}\right)}. \tag{3.15}$$

Eq. (3.15) is obtained assuming that the sum of projectile and target nuclear mass in the initial state is equal to the sum of the ejectile and recoil nuclear mass in the final state. Here, E is the laboratory energy of the incident particle, and Q is the reaction Q-value corresponding to the specific excited state. It assumed that the Q-value is negligible compared to the total mass of the initial state. Finally, one obtains

$$\frac{d\sigma}{d\Omega_{cm}} = \frac{d\sigma}{d\Omega_{lab}}\frac{d\Omega_{lab}}{d\Omega_{cm}}, \tag{3.16}$$

$$\frac{d\Omega_{lab}}{d\Omega_{cm}} = \frac{d(\cos\theta_{lab})}{d(\cos\theta_{cm})}. \tag{3.17}$$

From the above, the relationship between the centre of mass cross section and the laboratory cross section is given by [54]

$$\left(\frac{d\sigma}{d\Omega}\right)_{cm} = \left(\frac{d\sigma}{d\Omega}\right)_{lab}\left(\frac{1+\gamma\cos\theta_{cm}}{(1+2\gamma\cos\theta_{cm}+\gamma^2)^{\frac{3}{2}}}\right). \tag{3.18}$$

3.2.7 Elastic scattering

The elastic scattering data from our experiment served two purposes. The first was to select the best optical model parameters (OMPs) for the DWBA calculations. The second was to determine the correct number of ^{136}Ba nuclei in the target N_t.

Selecting the appropriate optical model parameters

To trust the reliability of the OMP sets for the entrance channel of the (p, t) reaction, we compared the experimental ^{136}Ba(p, p) cross sections (as a ratio to Rutherford cross sections) with the DWBA predictions using different global OMPs. The ratio to Rutherford cross sections is used instead of the absolute scattering cross sections because differences in the optical model parameters are expected to arise from the nuclear part of interaction rather than the Coulomb part. Rutherford scattering is purely Coulomb interaction, and the centre of mass cross section for any charged particle (z_p) and target combination (z_t) is

$$\left(\frac{d\sigma}{d\Omega}\right)_{Rutherford} = 10\left[\frac{z_p z_t \alpha(\hbar c)}{4E_{cm}\sin^2(\theta_{cm}/2)}\right]^2 \text{mb/sr.} \tag{3.19}$$

Here θ_{cm} is given in Eq. (3.14), $E_{cm} = \frac{m_t}{m_t+m_p}E_{lab}$ is the projectile energy in the center of mass, $\alpha = 1/137$ is the fine structure constant and $\hbar c =$ 197 MeV-fm. The Rutherford cross sections are multiplied so that they have the same units as the ones obtained from Eq. (3.6). The DWBA ratio-to-Rutherford cross sections were obtained from DWUCK4 [44] using diffrent OMPs. Based on previous work [55] with ^{138}Ba(p, t) and ^{138}Ba(p, p) and our experimental data, we chose the OMP that gave the minimum χ^2, defined by

$$\chi^2 = \sum_i \frac{[Y_{DWBA}(\theta_i) - Y_{Exp}(\theta_i)]^2}{\sigma^2_{Exp}(\theta_i)}. \tag{3.20}$$

In the above, $Y_{DWBA}(\theta_i)$ and $Y_{Exp}(\theta_i)$ represent DWBA and experimental cross sections respectively. The parameter $\sigma_{Exp}(\theta_i)$ denotes the variances of $Y_{Exp}(\theta_i)$ and θ_i represent the CM angles described previously.

Target thickness determination

Since Rutherford scattering dominates at small angles, its cross section can be used to determine the effective target thickness. Consequently, at small θ_i, the measured cross sections are mostly independent of the choice of OMPs. The number of ^{136}Ba nuclei in the target is given by

$$N_t = \frac{\rho t N_A \beta}{M \cos\theta_{target}} 0.93, \tag{3.21}$$

where ρ is the target material density, t is the target thickness, N_A is the Avogadro's number and M is the molar mass of the target material (^{136}BaO). The quantity $\rho t \approx 40 \mu g/cm^2$ is the nominal areal density of the target, provided by the target maker and the factor 0.93 accounts for the isotopic enrichment of ^{136}Ba. The $\cos\theta_{target}$ term accounts for the angle of the target frame relative to the beam. In the above, β is the correction factor obtained by normalizing the DWBA calculation to the experimental elastic scattering data obtained at $\theta_{lab} = 15°$. This small angle was chosen because the (p, p) cross sections obtained using different proton optical models start diverging at higher angles due to contributions from the nuclear part of the interaction. These results are shown in Figs. 3.8 and 3.9 respectively. Based on these data, we chose to use the OMP parameters recommended by Varner *et al.* [56] to analyse our data. The correction factor was $\beta = 0.36 \pm 0.01$ which allowed to obtained the measured effective target thickness of 14.4 $\mu g/cm^2$.

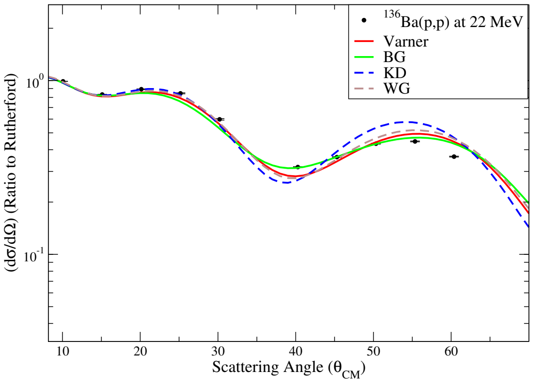

Figure 3.8: Comparison between experimental data and DWBA predictions of angular distributions for ^{136}Ba(p,p) elastic scattering. Proton OMPs were taken from Becchetti and Greenless (BG) [57], Koning and Delaroche (KD) [58], Varner *et al.* [56], Walter and Guss (WG) [11].

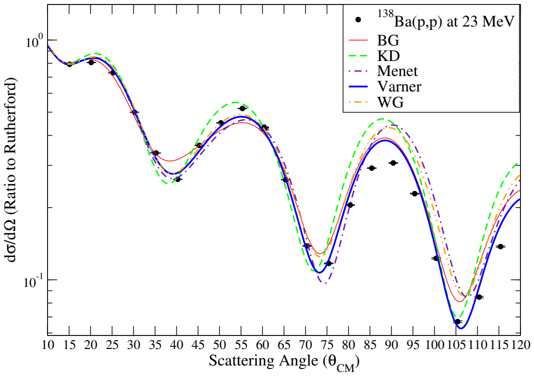

Figure 3.9: Comparison between experimental data and DWBA predictions of angular distributions for ^{138}Ba(p,p) elastic scattering . Proton OMPs were taken from Becchetti and Greenless (BG) [57], Koning and Delaroche (KD) [58], Varner *et al.* [56], Walter and Guss (WG) [11] and Menet *et al.* [59].

3.2.8 Beam particles

In order to obtain absolute cross sections, it is important to know the total number of beam particles incident on the target. For the Q3D, this is obtained using a Faraday cup placed behind the target ladder (at zero degrees to the beam axis). Since only a very small percentage of the beam interacts with the target material, the undeflected beam current measured on the Faraday cup is approximately equal to the total beam current incident on the target. It is connected to the Brookhaven Instruments Corporation (BIC) current integrator. The measured current (I) is directly proportional to the number N of beam particles hitting the Faraday cup per second,

$$\frac{N}{t} = \frac{I}{e}. \tag{3.22}$$

The BIC converts charge into pulses that can be read out on a scaler module (scaler 1). The current scale on the BIC was set to 2 μA, which yielded a pulse rate of 1 kHz. For each run, the number of beam particles was then determined using the following relationship,

$$N_b = Scaler1 \frac{2\mu A}{(1000s^{-1})e}. \tag{3.23}$$

3.2.9 Dead time corrections

In detector systems, there exists a minimum amount of time required to process the signals. This minimum processing time is called dead time of the counting system and it occurs both in the detector as well as in the data acquisition system (DAQ) [60]. The dead time causes true events to be missed being recorded while collecting data. Therefore, absolute measurements always have to correct for such dead time effects. For this experiment, the events affected by the application specific integrated circuit (ASIC) dead time of the detector were recorded and binned in channel 0 of the analog-to-digital convertor (ADC). The fraction of dead events due to this effect was calculated from the ratio of the number of the counts in the channel 0 to the total number of counts in the ADC, so that the ASIC dead time correction factor is

$$LT_{DET} = 1 - \left(\frac{channel(i=0)}{\sum_{i=0}^{2500} channel(i)} \right). \tag{3.24}$$

Similarly, if events were not recorded due to the DAQ dead time and the current integrator were incremented during this time, missed events were read into another scaler (scaler 3) for each run. The dead time percentage for the DAQ was obtained using the ratio of scalar 3 to scaler 1, such that

$$LT_{DAQ} = 1 - \left(\frac{Scaler3}{Scaler1} \right). \tag{3.25}$$

3.2.10 Solid angle determination

The solid angle acceptance of the Q3D is controlled by a set of horizontal (X) and vertical (Y) slits. The slits are opened or closed using micrometer precision screwgauges. The aperture is diamond shaped, as shown in Fig 3.10. The spectrograph has a maximum solid angle coverage of about 15 msr. The total solid angle coverage of the detector is evaluated from the geometry of

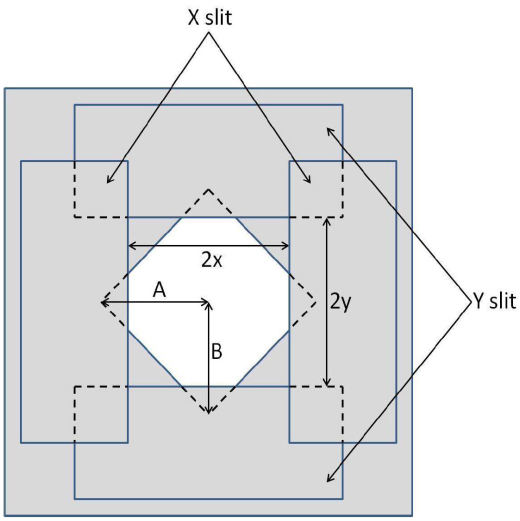

Figure 3.10: Acceptance slits at the Q3D spectrograph.

the system as

$$\Delta\Omega = \frac{1}{R^2}\left[4\Delta X\Delta Y - 2\left(\Delta X - A + \frac{A\Delta Y}{B}\right)\left(\Delta Y - B + \frac{B\Delta X}{A}\right)\right] \tag{3.26}$$

In the above A, B are the half width and height of the opening, R is the distance between the aperture and target ladder. The ΔX and ΔY parameters represent the distances between the X and Y slits respectively.

3.2.11 Uncertainties in Cross Section

The total uncertainty in the measured values of cross section arises from statistical uncertainties and several systematic uncertainties that were added in quadrature. For instance, while estimating the appropriate target thickness, uncertainties contribute from the choice of optical models, as explained in

Section 3.3. Additional contributions also arise from the uncertainties in the laboratory angles, masses of nuclei, reaction Q values, and the beam energy.

3.3 DWBA calculation

The orbital angular momentum transfer (L) to excited states were assigned by comparing the experimental angular distributions with the DWBA predictions. As discussed in Section 2.5, only natural parity states would be strongly populated in the (p, t) reaction. Thus the spin-parity of the states is determined based on agreement with the shapes of angular distributions. Various DWBA codes have been developed to evaluate theoretical angular distributions for transfer reactions. The DWBA analysis used in this thesis were carried out using the DWUCK4 [44] code described briefly in Appendix A.

Optical Model Parameters for DWBA

For the entrance p + ^{136}Ba channel, we used the OMPs recommended by Varner *et al*. [56] based on the discussion in Section 3.2.7. For the exit t + ^{134}Ba channel, since we did not have triton scattering data available, we compared our data with the DWBA calculations performed with the OMPs recommended by Li, Liang, and Cai [61] and Becchetti and Greenless [62]. We observe that the global OMPs recommended by Liang, and Cai showed better agreement with our data. These results are shown in Fig. 3.11.

Therefore, we used the proton OMPs set from Ref. [56] and the triton OMPs set from Ref. [61] in our DWBA analysis. The proton OMPs are fixed for proton energy $E_p = 22$ MeV while the triton parameters are calculated for each excitation energy as a function of triton outgoing energy. The two-neutron transfer form factor was obtained by adjusting the depth of the real volume part of the potential such that each neutron transferred had a binding energy of half the two-neutron separation energy and the excitation energy of the recoil nucleus,

$$BE = \frac{S_{2n}(^{136}Ba) + E_x(^{134}Ba)}{2}. \tag{3.27}$$

The OMPs used to perform our calculations are presented in Table 3.2.

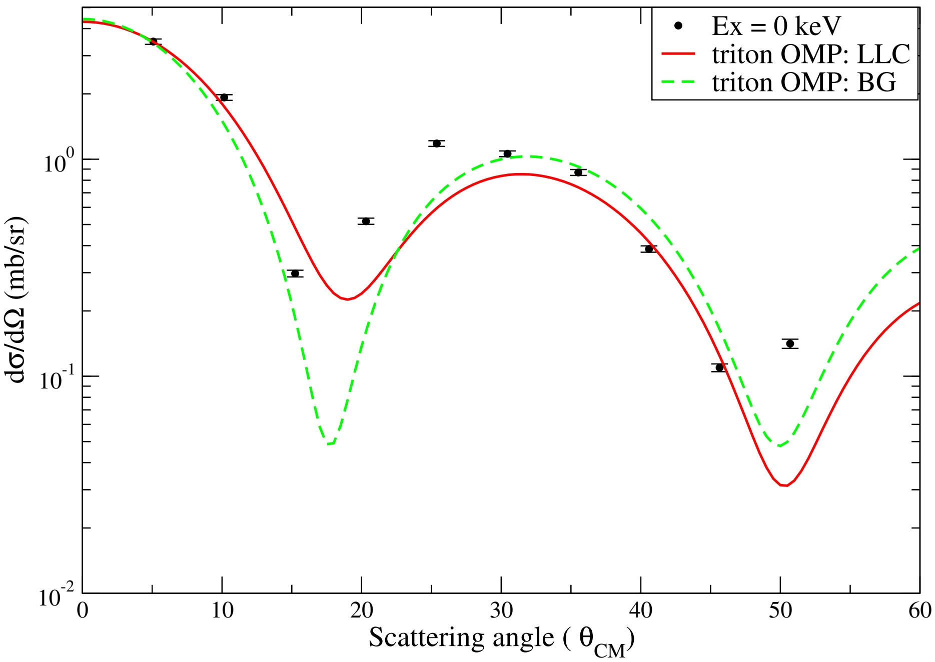

Figure 3.11: Triton angular distribution for the ground state in ^{134}Ba. The DWBA curves are obtained using two different triton OMPs, t + ^{134}Ba set by Li, Liang, and Cai [61] and t + ^{134}Ba set by Becchetti and Greenless [62].

Table 3.2: Optical model parameters used our analysis. The proton OMPs are from Varner *et al.* [56], triton OMPs from Li, Liang, and Cai [61] and neutron OMPs are from Ref. [57]. The triton parameters are given as a function of triton energy E_t, mass number $A = 134$, atomic number $Z = 56$, and neutron number $N = 78$.

Parameters	p	t	n
V_v (MeV)	53.1023	137.6-0.1456E_t + 0.0436E_t^2	-
		+ 4.3751$(N-Z)/A$ + 1.0474$Z/A^{1/3}$	
r_v (fm)	1.20	1.1201 - 0.1504$A^{-1/3}$	1.170
a_v (fm)	0.690	0.6833 + 0.0191$A^{1/3}$	0.75
W_v (MeV)	1.158	7.383 + 0.5025E_t - 0.0097E_t^2	-
r_{W_v} (fm)	1.248	1.3202 - 0.1776$A^{-1/3}$	-
a_{W_v} (fm)	0.690	1.119 + 0.01913$A^{1/3}$	-
W_s (MeV)	36.165	37.06 - 0.6451E_t - 47.19$(N-Z)/A$	-
r_s (fm)	1.248	1.251 - 0.4622$A^{-1/3}$	-
a_s (fm)	0.690	0.8114 + 0.01159$A^{1/3}$	-
V_{so} (MeV)	23.6	1.9029	-
r_{so} (fm)	1.106	0.46991 + 0.1294$A^{-1/3}$	-
a_{so} (fm)	0.63	0.3545 - 0.0522$A^{1/3}$	-
r_c (fm)	1.26	1.4219	-

Chapter 4

Results and Conclusions

4.1 Results and discussion

In this experiment, 66 energy levels in ^{134}Ba were observed in total, with most of the experimental angular distributions showing good agreement with the DWBA calculations. About 22 states are newly identified in this work and spin-parity assignments have been made for most of these states. We also observed one new 0^+ state and verified the existence of previously identified 0^+ states. Fig. 4.1 shows the ^{136}Ba(p,t) spectra obtained from this experiment at $\theta_{lab} = 25°$, and all the observed states in ^{134}Ba from this experiment are listed in Table. 4.1. The angular distribution plots for all these states are shown in Appendix B.

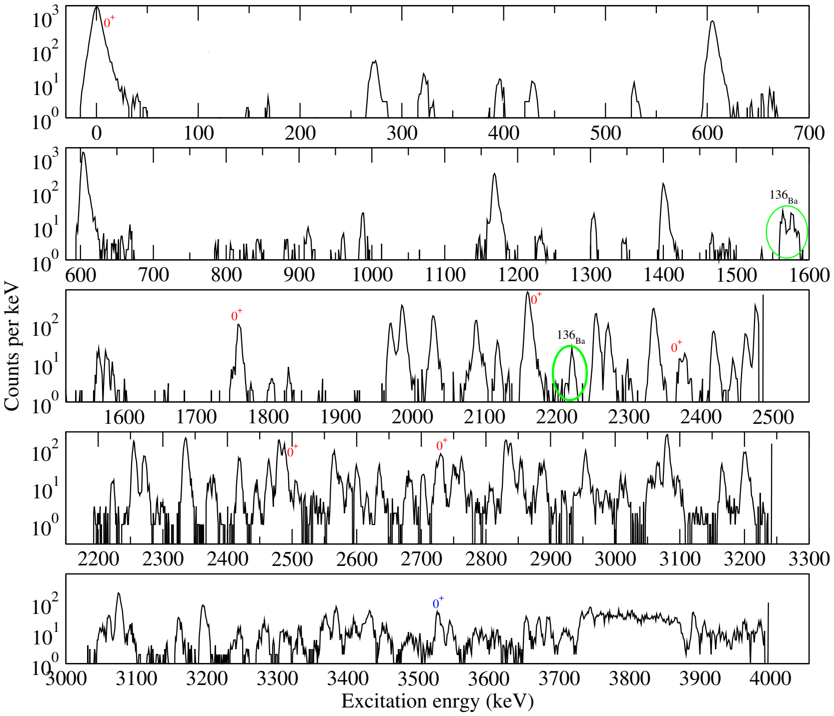

Figure 4.1: Triton spectra corresponding to excited states in ^{134}Ba obtained from this experiment. These data were collected with five magnetic field settings (momentum bites) and represent one angle at $\theta_{lab} = 25°$. The 0^+ states observed in this experiment and specific contaminants are labeled in this figure.

4.1.1 Excitation energy levels in ^{134}Ba

Table 4.1: Excitation energy levels in ^{134}Ba observed in this experiment compared to previously known information, taken from the Nuclear Data Sheets [63].

Known		This work	
E_x	J^π	E_x	J^π
0	0^+	0	0^+
604.7223 (9)	2^+	604.8 (2)	2^+
1167.968 (3)	2^+	1168 (2)	2^+
1400.590 (4)	4^+	1400.6 (2)	$(4^+, 5^-)$
1760.555 (22)	0^+	1760.3 (2)	0^+
1969.921 (4)	4^+	1970.1 (2)	4^+
1986.35 (21)	5^-	1986.2 (1)	$(4^+, 5^-)$
2029.242 (18)	2^+	2029.7 (1)	2^+
2088.288 (17)	2^+	2087.9 (6)	2^+
2118.195 (9)	(4^+)	2118.7 (2)	4^+
2159.683 (21)	$(0)^+$	2159.64 (9)	0^+
2254.95 (14)	3^-	2254.8 (1)	3^-
2271.57 (24)	7^-	2271.2 (2)	7^-
2334.76 (6)	$(1,2^+)$	2334.2 (1)	2^+
2371.02 (7)	2^+	2371.5 (4)	0^+
2379.112 (18)	0^+	2379.0 (4)	2^+
		2418.4 (3)	$(4^+,5^-)$
		2444.9 (5)	4^+
2464.28 (6)	(2^+)	2464.1 (3)	2^+
2480.34 (5)	(2,3)	2480.2 (3)	3^-
2488.434 (21)	0^+	2488.4 (3)	0^+
2564.712 (19)	$(1^+,2^+)$	2565.0 (3)	2^+
2574.31 (10)	(2^+)	2574.5 (4)	2^+
		2587.9 (4)	$(4^+,5^-)$
2599.88 (4)	2^+	2600.6 (3)	2^+

Table 4.1 – continued from previous page

E_{x}	J^{π}	E_{x}	J^{π}
		2635.1 (3)	$(4^{+},5^{-})$
		2680.9 (5)	3^{-}
		2702.8 (6)	$(4^{+},5^{-})$
2729.23 (4)	$(1^{+},2^{+})$	2729.0 (3)	0^{+}
2747.965 (24)	2^{+}	2750.8 (5)	2^{+}
2828.50 (4)	$(1^{+},2^{+})$	2830.5 (3)	2^{+}
2835.9 (4)	(8^{+})	2837.8 (4)	$(4^{+},5^{-})$
2851.26 (6)	2^{+}	2854.3 (4)	2^{+}
		2883.3 (5)	4^{+}
2950.56 (24)	(3,4)	2953.8 (5)	$(4^{+},5^{-})$
		3049.9 (5)	3^{-}
		3053.6 (7)	3^{-}
3061.29 (6)	$2^{(+)}$	3060.8 (5)	2^{+}
3074.72 (25)	(2)	3075.1 (4)	5^{-}
3079 (10)	4^{+}	3079.9 (7)	$(4^{+},5^{-})$
		3097.4 (9)	$(4^{+},5^{-})$
3160.07 (19)	$(1,2^{+})$	3160.5 (5)	1^{-}
		3195.7 (4)	3^{-}
3245.88 (19)	1	3245.3 (7)	$(6^{+}, 7^{-})$
		3281.6 (6)	3^{-}
3368.97 (6)	(1,2)	3369.5 (6)	2^{+}
		3383.5 (4)	2^{+}
3432.15 (1)	$(1,2^{+})$	3431.42 (5)	$(1^{-},2^{+})$
3451.0 (4)	$1,2^{+}$	3452.1 (6)	(4^{+})
		3528.1 (4)	0^{+}
3548.5 (4)	$(1,2^{+})$	3545.5 (5)	2^{+}
3652.1 (7)	$(1,2^{+})$	3653.5 (5)	1^{-}
3684.2 (4)	2^{+}	3684.6 (5)	4^{+}
3705	1	3707 (1)	$(4^{+},5^{-})$
		3715 (2)	2^{+}

Table 4.1 – continued from previous page

E_x	J^π	E_x	J^π
		3733.6 (8)	4^+
		3744.4 (6)	2^+
3754 (10)		3758.9 (6)	$(6^+, 7^-)$
		3798 (1)	$(3^-, 4^+)$
3836	1	3832 (1)	$(4^+,5^-)$
		3843 (1)	$(4^+,6^+)$
		3867.7 (8)	$(4^+,5^+)$
		3890.5 (5)	2^+
3899.1 (11)		3905.9 (5)	$(4^+,5^+)$
		3963.3 (6)	
3980	(1)	3984.8 (6)	

4.1.2 Spin-parity assignments

E = 1400 keV

The excited state at 1400 keV was first observed in the angular correlation of gamma rays of ^{134}Ba resulting from the decay of ^{134}Cs [64]. This energy level was measured at 1402 keV with the spin of 4 and the parity of this state was not reported. This state was remeasured in a (γ, γ) coincidence experiment [65] thereby confirming the 4^+ assignment. In our work, the DWBA prediction favors a 5^- assignment. Hence we assign $J^\pi = (4^+, 5^-)$ for this state.

E = 1986 keV

The energy leve at 1986 keV with assignment spin-parity $J^\pi = 5^-$ was first observed in the excitation energy spectrum of (p, t) reaction on ^{136}Ba, at the proton beam energy of 52 MeV [66]. This energy level was also reported in $(n, n'\gamma)$ measurements [67] at the energy of 1986.08 keV with $J^\pi = 5^-$. In our work, both $L = 4$ and 5 reproduce the experimental angular distribution. However the $L = 4$ angular distribution has a lower χ^2. Thus, we assigned $J^\pi = (4^+, 5^-)$ to this state.

E = 2118 keV

The 2118 keV energy level was assigned $J^\pi = (4^+)$ in the level scheme of ^{134}Ba from the $(n, n'\gamma)$ experiment [67]. Our DWBA angular distributions for $L = 4$ agrees with experimental data. So we assign $J^\pi = 4^+$ to this state, now removing the ambiguity.

E = 2159

The level at 2159 keV was assigned a tentative $J^\pi = (0^+)$ in the Nuclear Data Sheets of ^{134}Ba [66, 67, 68]. This state was also recently reported at 2159 keV from ^{136}Ba(p, t) measurements [69]. In our work we reproduce the angular distribution for this state using $L = 0$ transfer. Thus, we assign J^π $= 0^+$ for this level.

E = 2334 keV

The measurement of the 2334 keV level in ^{134}Ba was first observed from the decay of ^{134}Ce $\rightarrow$ ^{134}La by observing the γ-ray transitions in ^{134}La [68]. The J^π of this level was completely unknown from these measurements. Later $(n, n'\gamma)$ studies [67] reported the state with a J^π assignment of $1, 2^+$. This level was observed again in the (p, t) reaction on ^{136}Ba and assigned as

$J^\pi = 2^+$ [69]. In our work, the experimental angular distribution reproduced the characteristic of an $L = 2$ transfer. Thus, we assign this state as $J^\pi = 2^+$.

E = 2371 keV

The 2371 keV level was previously investigated through ^{134}Ba$(n, n'\gamma)$ measurements [67]. The γ-ray angular distributions from this work favored the $J^\pi = 2^+$. However, in our work the experimental angular distribution is consistent with the DWBA prediction for an $L = 0$ transfer. Thus, we assigned this level $J^\pi = 0^+$.

E = 2379 keV

This state was reported to be $J^\pi = 0^+$ [68, 67, 70]. However, our angular distribution shows a characteristic $L = 2$ shape. Therefore we assign the spin-parity of this energy level to be 2^+.

E = 2418 keV

Spin-parity of $J^\pi = 4^+$ was assigned for a state at 2420 keV using a ^{136}Ba(p, t) reaction [69]. In this work, we observed this level at 2418 keV. The experimental angular distribution is reproduced by both $L = 4$ and $L = 5$ transfer. Since we could not separate the two possibilities, we propose a $J^\pi = (4^+, 5^-)$ for this level.

E = 2444 keV

This energy level is observed for the first time and its experimental angular distribution agrees with an $L = 4$ transfer. Therefore, the spin-parity of level is assigned as $J^{\pi} = 4^{+}$.

E = 2464 keV

The 2464 level was assigned as a (2^{+}) from ^{134}Ba$(n, n'\gamma)$ measurements [67]. In this work, the angular distribution is consistent with a 2^{+} distribution. Thus, we confirm the spin-parity of this level to be 2^{+} .

E = 2480 keV

Two energy levels were previously reported in the vicinity of this energy. The first at 2479±10 keV with $J^{\pi} = 4^{+}$ [70]. The second was observed at 2480 keV from ^{134}Ba$(n, n'\gamma)$ measurements with $J^{\pi} = (2, 3)$ [67]. Our DWBA angular distribution for $L = 3$ agrees with the experimental data, hence it has been assigned as a 3^{-} state.

E = 2564 keV

The first measurement of 2564 keV level was reported as $J^{\pi} = 1^{+}, 2^{+}$ [68, 67]. A recent measurement done using (p, t) reaction on ^{136}Ba proposed a 2^{+} assignment for a state at 2566 keV [69]. The angular distribution for this state matches an $L = 2$ transfer. Hence we assigned this as $J^{\pi} = 2^{+}$.

E = 2574 keV

The angular distribution for this state is reproduced by an $L = 2$ transfer. Thus we assign this state to be $J^{\pi} = 2^{+}$, which clarifies a previous ambiguity.

E = 2587 keV

This level was observed in previous ^{136}Ba(p,t) studies and was assigned a spin-parity of 4^+ [69]. In this work, we compared both $L = 4$ and $L = 5$ transfer with the experimental angular distribution. However, since we could not separate the two possibilities, we suggest an assignment $J^\pi = (4^+, 5^-)$ for this level.

E = 2635 keV

Previous (p,t) reaction on ^{136}Ba studies identified a state with $J^\pi = 4^+$ at 2633 keV [69]. We compared both $L = 4$ and $L = 5$ transfer with experimental data. However, we could not separate the two possibilities. Thus we propose a $J^\pi = (4^+, 5^-)$ assignment.

E = 2680 keV

Previous studies measured a level at 2677 keV and reported it as $J = 3, 4$ [67]. This level was remeasured to be at 2679 keV using the ^{136}Ba(p,t) reaction and $J^\pi = 3^-$ was assigned [69]. In this work, the experimental angular distribution reproduced an $L = 3$ transfer, therefore we confirm this level to be a $J^\pi = 3^-$ state.

E = 2702 keV

The 2702 keV level was proposed to be a (4^+) state in Ref. [69]. In this work we compared $L = 4$ and 5 transfers with the experimental angular distribution. However, we could not separate these two possibilities from the angular distributions.

E = 2729 keV

In the adopted level scheme for ^{134}Ba, an excited state at 2729 keV is reported as $J^{\pi} = 1^{+}, 2^{+}$ [63]. However in a recent ^{136}Ba(p, t) measurement [69], a state at 2727.5 keV is reported to be 0^{+}. Our work confirms this assignment.

E = 2830 keV

A state at 2828.49 keV was first observed in the level scheme of ^{134}Ba resulting from the beta decay of ^{134}La, and reported as $J^{\pi} = 1^{+}, 2^{+}$ [68]. Later measurements observed that this level ought to have a $J^{\pi} = 2^{+}$ assignment [69]. Based on our experimental and DWBA angular distributions, we confirm that it is $J^{\pi} = 2^{+}$.

E = 2837 keV

The 2835 keV state was proposed to have a spin-parity of (8^{+}) [71]. In this work, two DWBA L transfer (4,5) were compared with the experimental data. It was difficult to separate the two possibilities and assign confidently the spin-parity of this state. Therefore, we suggest that the J^{π} of this state is $(4^{+}, 5^{-})$.

E = 2883 keV

Recent measurements using the ^{136}Ba(p, t) reaction reported the level at 2883 keV to be 0^{+} state [69]. However our angular distributions show that it is most likely $J^{\pi} = 4^{+}$.

E = 2953 keV

Previous ^{134}Ba$(n, n'\gamma)$ measurements showed that the 2950.56 keV state had a spin assignment of (3,4) [67]. Our angular distribution is more consistent with an $L = 4$ transfer. Thus we assigned this state as $J^\pi = 4^+$.

E = 3049 keV

This level is newly observed and the experimental data agrees with an $L = 3$ transfer. Hence we assigned $J^\pi = 3^-$ to the state at 3049 keV.

E = 3053 keV

A level at 3054 keV was previously observed in (p, t) reaction on ^{136}Ba with a $J^\pi = 2^+$ assignment [69]. Our angular distribution however agrees better with an $L = 3$ transfer. Thus we assigned $J^\pi = 3^-$ for this level.

E = 3060 keV

A study of this level observed from the decay of ^{134}La, showed that the spin-parity could be $1^+, 2^+$ at 3061 keV [68]. Other measurements using ^{134}Ba$(n, n'\gamma)$ reported a $2^{(+)}$ assignment [67]. Our experimental angular distribution is consistent with $L = 2$, so the ambiguity on the spin-parity of this level is resolved with $J^\pi = 2^+$.

E = 3079 keV

A previous study of ^{134}Ba(p, t) proposed state at 3079 keV with spin-parity 4^+ [66]. We considered two possibilities of L transfer (4,5). Unfortunately, we still could not resolve the $L = 4$ and 5 ambiguity from the angular distributions. We suggest that this state is $(4^+, 5^-)$.

E = 3097 keV

This level is observed for the first time and both $L = 4$ and 5 are possible, based on the experimental angular distributions. We report this level as a $J^\pi = (4^+, 5^-)$.

Ex = 3160 keV

Previous measurements described the 3160 keV level to be either a 1^- or 2^+ state [68, 67]. Our angular distribution agrees with $L = 1$ transfer. Therefore, the energy level of 3160 keV is assigned $J^\pi = 1^-$.

E = 3195 keV

Previous studies on ^{136}Ba(p, t) proposed a possible 0^+ assignment for a 3181±8 keV state [70]. Recent ^{136}Ba(p, t) studies reported a state 3182 with a $J^\pi = (3^-)$ [69]. In this work the level at 3195 keV is observed and the data agrees with a $L = 3$ transfer. Thus we assigned this level to be $J^\pi = 3^-$.

E = 3245 keV

The first observation of the level in ^{134}Ba was from the decay of ^{134}La. A tentative (1^+) was assigned to this level [66]. The latter was again observed in ^{134}Ba$(n, n'\gamma)$ measurements and the spin-parity of the state was reported as possibly (1^+) [67]. This state was again identified in a photon scattering experiment on ^{134}Ba and a spin (1^+) was suggested [72]. However, due to the selection rules that restricts the spin-parity of the states to the choice of natural-parity states, this possibilty has not been considered. Moreover, the angular distributions could not show a characteristic of the $L = 1$ transfer. However, we explored the $L = 6$ and 7 transfer to assign a J^π for this level. So, in this work we suggest the $J^\pi = (6^+, 7^-)$ at this level.

E = 3281 keV

There was no level observed at this energy from previous studies. Our experimental angular distributions for this level indicates a $L = 3$ transfer. Thus, this level is assigned $J^\pi = 3^-$.

E = 3369 keV

The energy level of 3369 keV was previously known to be either a $J = 1$ or $J = 2$ state [68, 67]. Another observation using ^{136}Ba(p, t) assigned this state to be $J^\pi = 2^+$ [69]. From our angular distributions, we confirm this level has a $J^\pi = 2^+$.

E = 3383 keV

At 3380 keV, it was reported a $J^\pi = (4^+)$ [69], but our experimental angular distribution agreed with $L = 2^+$. Therefore, we assigned a $J^\pi = 2^+$ at this level.

E = 3452 keV

Two states were previously observed within a very small energy range for the 3452 keV level. The first measurement predicted the state to be at 3450 keV with $J^\pi = (1^+)$ [68, 72]. Other experiments mention a 3451 keV state with a J^π = 1,2^+ [67]. Because of the selection rules in the two-nucleon transfer reaction, the 1^+ state is weakly populated, and predictions using $L = 2$ do not match our measured distribution. However using $L = 4$ we are able to reproduce the data. Therefore, a possible (4^+) state is assigned to the 3452 keV level. But we suggest this be investigated further.

E = 3545 keV

Previous studies via the decay of ^{134}La reported a $J^\pi = 1, 2^+$ at 3548 keV. Our experimental angular distribution reproduced the $L = 2$ transfer. Thus we confidently assign this to be a $J^\pi = 2^+$ state.

E = 3653 keV

Multiple assignments were proposed in this energy region. The first assignment was made from the decay of ^{134}La where a $J^\pi = 1^+, 2^+$ was proposed at 3652 keV [68]. The second assignment was made using a ^{136}Ba(p, t) reaction, where a $J^\pi = 4^+$ was proposed [69]. Our DWBA calculations assuming $L = 1$ better reproduces the experimental data. Therefore we assigned this level as a 1^-.

E = 3684

The energy level at 3684 keV was previous observed using ^{134}Ba$(n, n'\gamma)$ mesasurements and the $J^\pi = 2^+$ was assigned [67]. However, in this work the experimental angular distribution data showed a reasonable agreement with the $L = 4$ transfer. Therefore, we suggested the $J^\pi = 4^+$ assignment at this level.

E = 3707 keV

The energy level of 3707 keV was measured to be 3705 keV, with $J = 1$ in a ^{134}Ba(γ, γ') experiment [72]. But our DWBA calculations for $L = 1$ transfer do not agree with the experimental data. We considered two possibilities of L transfer $(4, 5)$. Therefore, we suggest that this state is $(4^+, 5^-)$.

E = 3890 keV

The level at 3890 keV is observed for the first time and the experimental angular distribution indicates an $L = 2$ transfer. Hence we assigned this level a spin-parity of $J^\pi = 2^+$.

E = 3905 keV

The data sheets of ^{134}Ba [63] show a state at 3899 keV, with undefined spin-parity. Our work observed the state at 3905 keV with a proposed $J^\pi = (4^+, 5^-)$.

E = 3963 keV

The level at 3963 keV is observed for the first time. But the angular distribution data are inconclusive for this state.

E = 3984 keV

The level at 3980 keV is listed in the data sheets for ^{134}Ba [63]. In this work, we observe a state at 3984 keV as well, but our measured angular distribution could not allow a reliable extraction of the spin-parity information.

4.1.3 Implications for neutron pairing correlations

In this work a total of seven 0^+ states are identified in ^{134}Ba, three of which were already known previously [63]. Three other 0^+ states previously had ambiguities regarding their spin-parity assignments, that are now resolved. We also observe one new 0^+ state at 3528.1 keV. Additionnally, we do not observe the well known 0^+ states at 2336 keV, 2874keV [63], 3395 keV [69] and other potential 0^+ states at 2874 keV, 2996 keV, 3181 keV, 3501 keV, 3618 keV reported in the data sheets of ^{134}Ba [63] and 2961 keV, 3602 keV, 3750 keV reported in a recent ^{136}Ba(p,t) measurement [69].

The (p,t) strength of 0^+ excited states relative to the ground state is used as a factor to evaluate neutron-pair correlations. This strength is calculated using the following relationship

$$\varepsilon = \left(\frac{\left(\frac{d\sigma}{d\Omega}\right)^{exp}_{0^+_{ex}}}{\left(\frac{d\sigma}{d\Omega}\right)^{dwba}_{0^+_{ex}}} \right) \left(\frac{\left(\frac{d\sigma}{d\Omega}\right)^{exp}_{0^+_{gs}}}{\left(\frac{d\sigma}{d\Omega}\right)^{dwba}_{0^+_{gs}}} \right)^{-1} . \tag{4.1}$$

The above ratio removes the Q-value dependence on the cross sections. Our results for the relative $L = 0$ (p,t) strengths are shown in Table 4.2. We also plot in Fig. 4.2 the angular distributions of the excited 0^+ states in ^{134}Ba observed in our experiment.

In the above, we compare relative normalizations described by Eq. (4.1) for the most forward angle ($\theta_{CM} \sim {}^\circ$) and the forward angle data for the first

Table 4.2: Relative (p, t) strength calculations of all excited 0^+ states in ^{134}Ba observed in this experiment. The integrated strength calculations take into account all the 0^+ states relate to the ground state.N is the DWBA to data normalization.

Ex (keV)	σ (mb/sr)	ϵ (θ_{CM} ~5°)	N (5°-15°)	ϵ(%)
0	3.48(9)	100	17439(323)	100
1760.3(2)	0.184(7)	10.6(5)	1805(49)	10.4(3)
2159.64(9)	0.224(8)	16.5(7)	2936(72)	16.8(5)
2371.5(4)	0.007(1)	0.6(1)	171(16)	0.98(9)
2488.4(3)	0.075(4)	7.0(4)	1394(50)	8.0(3)
2729.0(3)	0.028(2)	3.1(2)	833(36)	4.7(2)
3528.1(4)	0.004(1)	0.9(3)	269(39)	1.5(2)
Σ		38(1)		42.5(8)

three angles (5°-15°) to determine the fragmentation of the $L = 0$ (p, t) strength. The latter are more reliable as they use more data points in a region where DWBA is best satisfied.

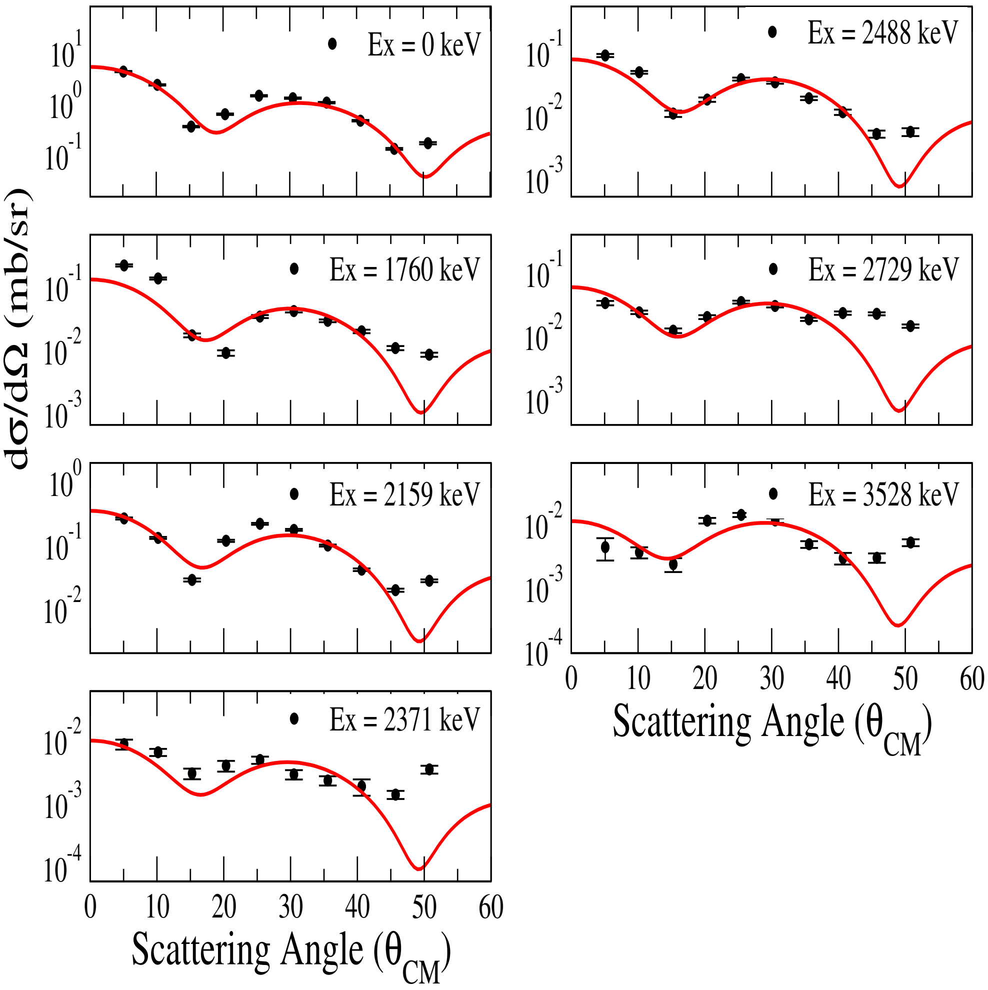

Figure 4.2: Angular distributions of 0^+ states in ^{134}Ba, observed with the ^{136}Ba(p,t) reaction.

4.2 Conclusions

In conclusion, we studied neutron pairing correlations using ^{136}Ba(p,t) reaction. In this experiment, we identified a total of seven 0^+ states wherein one 0^+ state is being reported for the first time and we could resolve the ambiguity in spin-parity for other three previously known states. We also do not observe several other predicted 0^+ states from previous investigations. In addition, 21 states were newly observed in our experiment, wherein we assign definite spins and parities for 19 states. We also observe a $\sim 40\%$ fragmentation in the (p, t) strength to 0^+ states indicating a breakdown in the neutron BCS approximation for ^{134}Ba. This is in addition to a similar breakdown from superfluid behavior observed in ^{136}Ba [55]. Our observations clearly indicate that since the (p, t) strength continues to be fragmented over excited 0^+ sates in another even Ba nucleus with $N \leq 82$, clearly deformation effects play an important role. The parent $0\nu\beta\beta$ decay nucleus (^{136}Xe) has neutron number $N = 82$ (it is singly closed shell) and is therefore nearly spherical. The work of Ref. [55] shows that ^{136}Ba in its ground state need not be nearly spherical as ^{136}Xe or ^{138}Ba, both of which have $N = 82$. This work supports the claim that the nuclear shapes continue to vary significantly for even barium nuclei with decreasing neutron number. This prompts a reassessment of the differences in nuclear deformation between ^{136}Xe and ^{136}Ba for future NME calculations of this important case.

Appendix A

DWUCK4 code

A.1 General description of DWUCK4

DWUCK4 is a computer code that calculates the scattering and reaction amplitudes using the distorted wave Born approximation. The calculations of transition amplitude for the reaction $A(a,b)B$ are performed assuming a zero-range interaction between the coordinate of incoming and outgoing wave functions. This approximation is valid for the calculation of particle transfer reactions, and the transition amplitudes for the DWBA take into account any combination of spin 0, spin 1/2 or spin 1 of the incoming and outgoing systems [44]. The optical potential used by DWUCK4 is similar to the OMP form explained in Section 2.3 and it uses OPTION = 1, 2 and 4 given by,

$$\begin{aligned} V(r) = &-V_v f_v(r, R_v, a_v) - iW_v f_w(r, R_w, a_w) && \text{OPTION} = 1 \\ &+ i4W_I a_s \frac{d}{dr} f_s(r, R_s, a_s) && \text{OPTION} = 2 \\ &+ \frac{(V_{so} + iW_{so})}{r} \frac{d}{dr} f_{so}(r, R_{so}, a_{so}) \vec{l} \cdot \vec{s} && \text{OPTION} = 4 \end{aligned} \tag{A.1}$$

The differences between the global OMP and DWUCK4 lFukudaie in the value of W_I and V_{so}. $W_I = 4 \times W_s$, the terms $\vec{\sigma} \cdot \vec{l}$ which is replaced by $\vec{l} \cdot \vec{s}$, and the potential used in DWUCK4 does not include the λ_π^2 factor. Therefore, the strength of the spin-orbit interaction potential used in DWUCK4 should be four times the strength of the spint-orbit potential defined with the $\lambda_\pi^2 \approx 2$ factor and an $\vec{\sigma} \cdot \vec{l}$ operator, $V_{so}^{DWUCK} = 4 \times V_{so}^{OMP}$. The DWUCK4 input file is described below.

A.2 DWUCK4 input file

The DWUCK4 input file is written following the FORTRAN77 format, and a sample of its file is shown in Fig A.1.

The input files of DWUCK4 are composed of seven input blocks. The first four input blocks describe the initialization variables. Blocks 5 and 6 describe the OMP to calculate the distorted waves for entrance and exit channels respectively, and the last block describes the core transferred particle interaction.

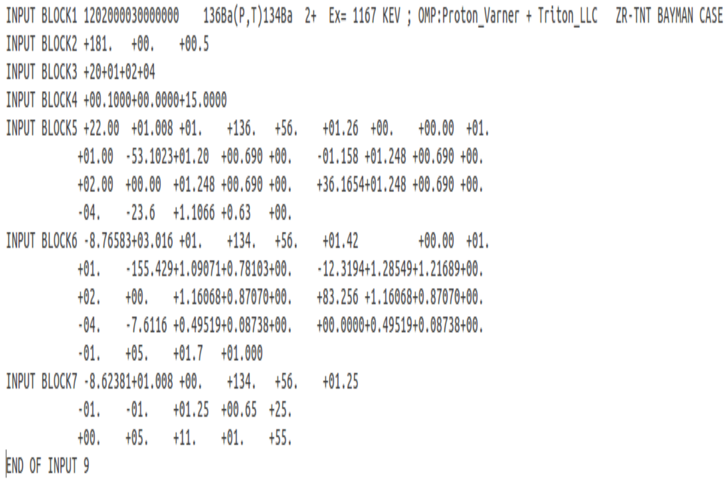

```
INPUT BLOCK1 120200003000000    136Ba(P,T)134Ba  2+  Ex= 1167 KEV ; OMP:Proton_Varner + Triton_LLC   ZR-TNT BAYMAN CASE
INPUT BLOCK2 +181.   +00.    +00.5
INPUT BLOCK3 +20+01+02+04
INPUT BLOCK4 +00.1000+00.0000+15.0000
INPUT BLOCK5 +22.00  +01.008 +01.    +136.   +56.    +01.26  +00.    +00.00  +01.
            +01.00  -53.1023+01.20  +00.690 +00.    -01.158 +01.248 +00.690 +00.
            +02.00  +00.00  +01.248 +00.690 +00.    +36.1654+01.248 +00.690 +00.
            -04.    -23.6   +1.1066 +0.63   +00.
INPUT BLOCK6 -8.76583+03.016 +01.    +134.   +56.    +01.42          +00.00  +01.
            +01.    -155.429+1.09071+0.78103+00.    -12.3194+1.28549+1.21689+00.
            +02.    +00.    +1.16068+0.87070+00.    +83.256 +1.16068+0.87070+00.
            -04.    -7.6116 +0.49519+0.08738+00.    +00.0000+0.49519+0.08738+00.
            -01.    +05.    +01.7   +01.000
INPUT BLOCK7 -8.62381+01.008 +00.    +134.   +56.    +01.25
            -01.    -01.    +01.25  +00.65  +25.
            +00.    +05.    +11.    +01.    +55.
END OF INPUT 9
```

Figure A.1: Input file sample for $L = 2$ transfer in ^{136}Ba$(p,t)^{134}$Ba reaction.

Input Block 1

This input block is divided in two parts. The first part is composed of 17 digits referred to as ICON(i) which initializes the program and allows the outputs to be generated. For instance, the first digit being 0 means do not read input block 2, the first digit being 1 means read the input block 2, and the digit 9 is used to stop the program. The second part is represented by 60 characters, beginning at column 21. This is used to give details of the reaction calculation.

Input Block 2

This input block gives the number of angles for the cross section calculation (N-ANGLES), specifies the the initial angle (ANGLE1) and the angle increment (D-ANGLE). The angles are set in degrees, and if there is no data input in this block, the program set the interval from 0° to 180° with 5° as increment.

Input Block 3

This input block sets the maximum number of partial waves (LMAX) that are used in the calculation, the maximum number of angular momentum transfers (NLTR), the orbital (LTR(I)) and the total (JTR(I)) angular momentum transfer. The value of JTR is twice the J transfer.

Input Block 4

This input block has five terms, the integration step-size for the radial coordinate (DR), the lower (RMIN) and upper (RMAX) cuttoff for the radial integrals, the Coulomb excitation scale factor (COUEX) and the Finite range correction factor (FNRNG).

Input Block 5

This input block has multiple inputs that provide the information about the entrance channel and specifies the optical model parameters choosen for the distorted waves. The first line sets the laboratory energy of the proton, the mass of proton in amu, charge of proton, the mass of ^{136}Ba in amu and charge of Ba nucleus, the reduced charge radius (r_{0_c}), the diffuseness of charge radius (AC), the non locality parameter (PNLOC) and twice the spin of the proton. The second line gives the potential option as established in Eq (A.1), which gives the type of potential, for example OPTION = 1 denotes the volume part of interaction as defined by the Volume Wood-Saxon potential ($V(r)$), OPTION = 2 represents the surface part of interaction ($W_I = 4 \times W_s^{OMP}$), and OPTION = 4 represents the spin-orbit part of interaction ($V_{so} = 4 \times V_{so}^{OMP}$ and $W_{so} = 4 \times W_{so}^{OMP}$). The negative value for option means that the current potential input block is the last one.

Input Block 6

This input block is the same as the input block 5 but the only difference is that the distorted waves correspond to the (t+^{134}Ba) channel and the proton energy is replaced by the Q-value of a specific excited state in ^{134}Ba.

Input Block 7

This input block represents the interaction between the transferred particle and the core nucleus. The input lines have the same meaning as the lines of input block 5 and 6 but that the projectile energy is replaced by the binding energy of the single particle transferred. The input lines varie from one reaction model to another, for example the form factor of (p, t) reaction is calculated using ICON(2)=2.

An extra line is added to the input lines in this block, it reads the number of nodes in the radial function excluding the origin and infinity (FN), the orbital angular momentum for the radial function (FL), twice the total angular momentum quantum number of the radial function (2*FJ), twice the intrinic spin of the radial function (2*FS), and the scaling factor for the potential defining the radial function (VTRIAL).

DWUCK4 output is by default displayed in the screen but can be transported into a text file using the following terminal command,

```
./dwuck4 dwuck.inp > dwuck.out.
```

Appendix B

^{136}Ba$(p,t)^{134}$Ba Angular distributions

Angular distributions for the ^{136}Ba(p, t) reaction are plotted below. The DWBA curves are obtained using DWUCK4 code, we used proton OMPs recommended by Varner [56] and triton OMPs by Li, Liang and Cai [61].

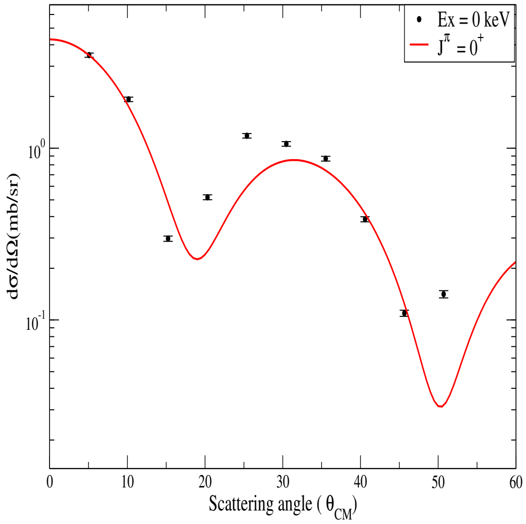
Ex = 0 keV
$J^\pi = 0^+$
dσ/dΩ(mb/sr)
10^0
10^{-1}
0
10
20
30
40
50
60
Scattering angle (θ_{CM})

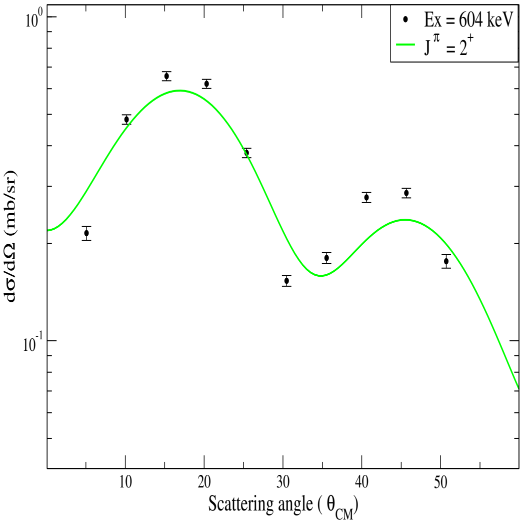
Ex = 604 keV
$J^\pi = 2^+$
dσ/dΩ (mb/sr)
10^0
10^{-1}
10
20
30
40
50
Scattering angle (θ_{CM})

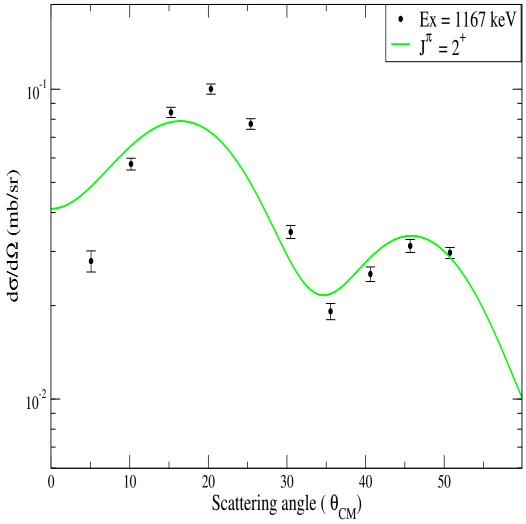
Ex = 1167 keV
$J^\pi = 2^+$
dσ/dΩ (mb/sr)
10^{-1}
10^{-2}
0
10
20
30
40
50
Scattering angle (θ_{CM})

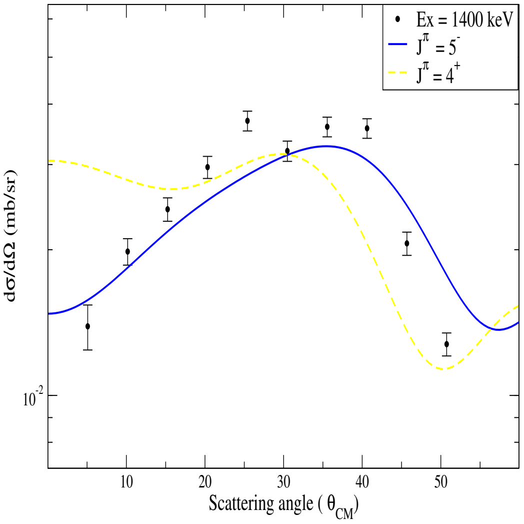
Ex = 1400 keV
$J^\pi = 5^-$
$J^\pi = 4^+$
dσ/dΩ (mb/sr)
10^{-2}
10
20
30
40
50
Scattering angle (θ_{CM})

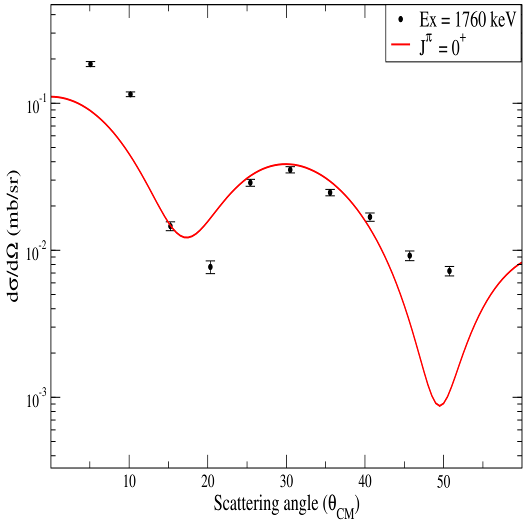
Ex = 1760 keV
$J^\pi = 0^+$
dσ/dΩ (mb/sr)
10^{-1}
10^{-2}
10^{-3}
10
20
30
40
50
Scattering angle (θ_{CM})

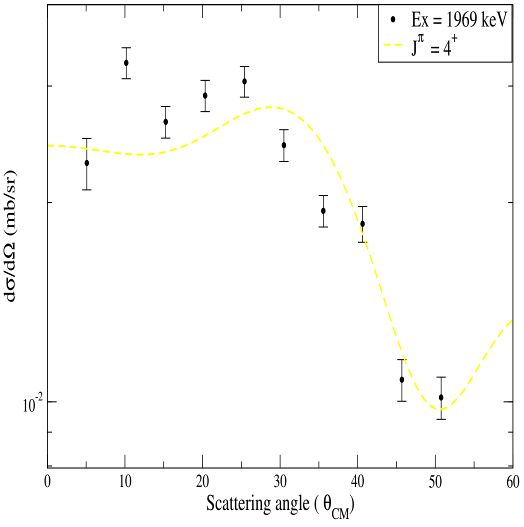
Ex = 1969 keV
$J^\pi = 4^+$
dσ/dΩ (mb/sr)
10^{-2}
0
10
20
30
40
50
60
Scattering angle (θ_{CM})

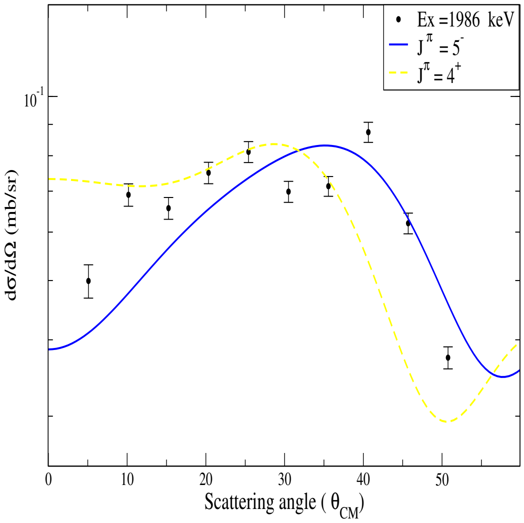
Ex =1986 keV
J^π = 5^-
J^π = 4^+
10^-1
dσ/dΩ (mb/sr)
0
10
20
30
40
50
Scattering angle (θ_CM)

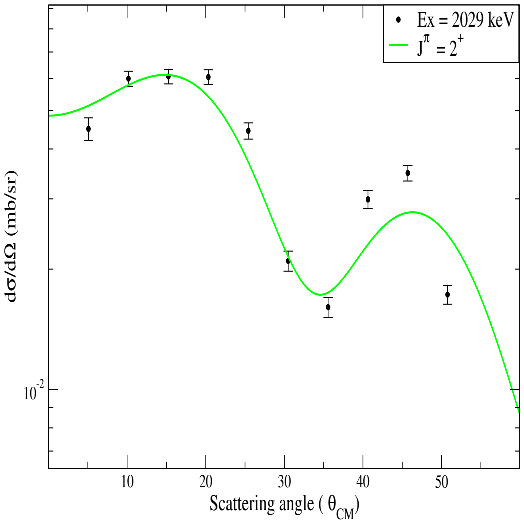
Ex = 2029 keV
J^π = 2^+
10^-2
dσ/dΩ (mb/sr)
10
20
30
40
50
Scattering angle (θ_CM)

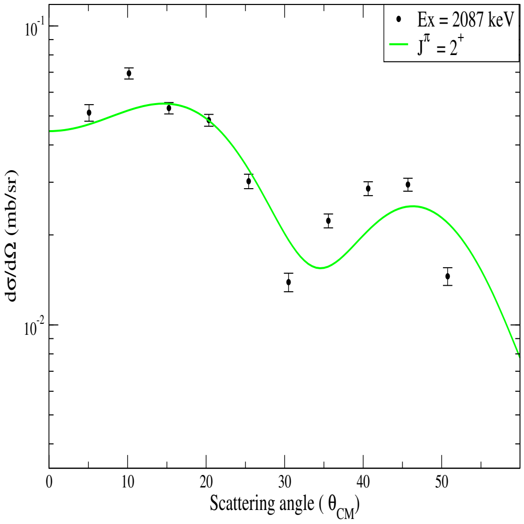
Ex = 2087 keV
J^π = 2^+
10^-1
10^-2
dσ/dΩ (mb/sr)
0
10
20
30
40
50
Scattering angle (θ_CM)

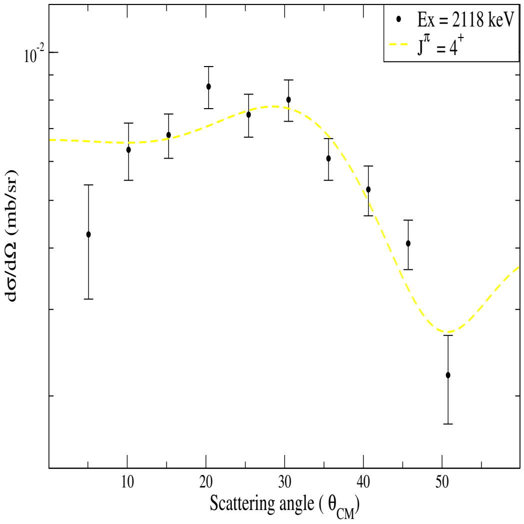
Ex = 2118 keV
J^π = 4^+
10^-2
dσ/dΩ (mb/sr)
10
20
30
40
50
Scattering angle (θ_CM)

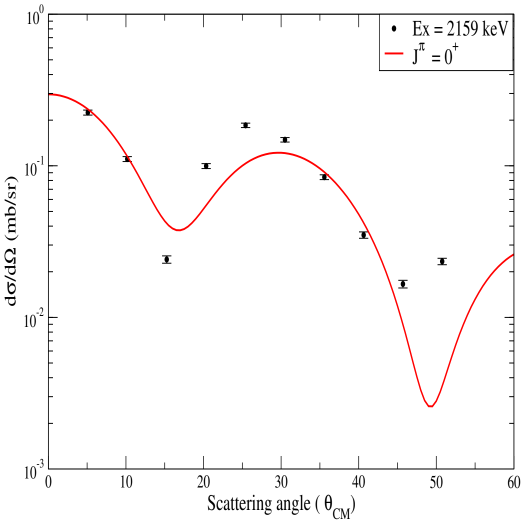
Ex = 2159 keV
J^π = 0^+
10^0
10^-1
10^-2
10^-3
dσ/dΩ (mb/sr)
0
10
20
30
40
50
60
Scattering angle (θ_CM)

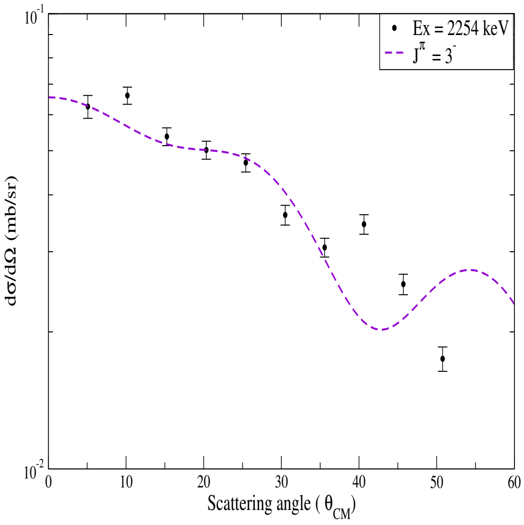
Ex = 2254 keV
J^π = 3^-
10^-1
10^-2
dσ/dΩ (mb/sr)
0
10
20
30
40
50
60
Scattering angle (θ_CM)

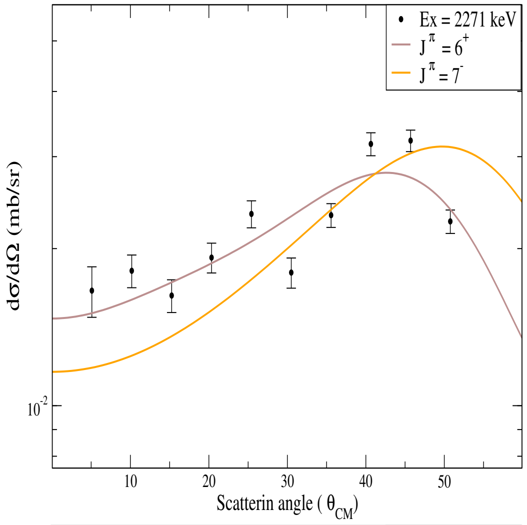
Ex = 2271 keV
J^π = 6^+
J^π = 7^-
dσ/dΩ (mb/sr)
10^-2
10
20
30
40
50
Scatterin angle (θ_CM)

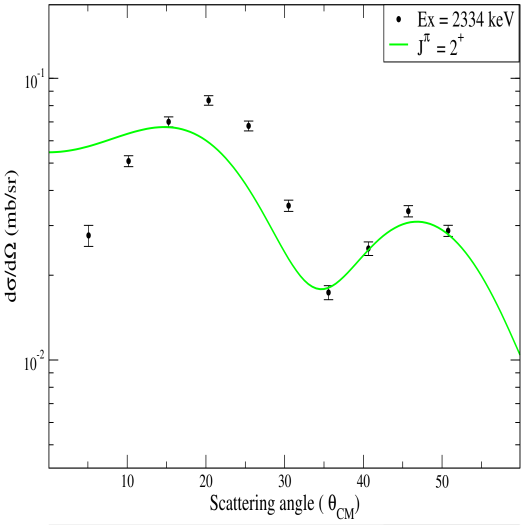
Ex = 2334 keV
J^π = 2^+
dσ/dΩ (mb/sr)
10^-1
10^-2
10
20
30
40
50
Scattering angle (θ_CM)

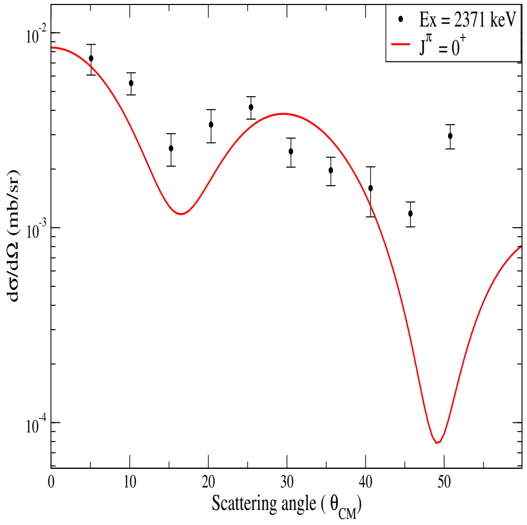
Ex = 2371 keV
J^π = 0^+
dσ/dΩ (mb/sr)
10^-2
10^-3
10^-4
0
10
20
30
40
50
Scattering angle (θ_CM)

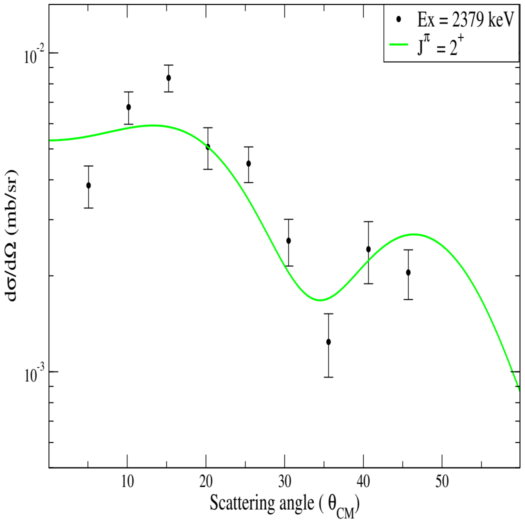
Ex = 2379 keV
J^π = 2^+
dσ/dΩ (mb/sr)
10^-2
10^-3
10
20
30
40
50
Scattering angle (θ_CM)

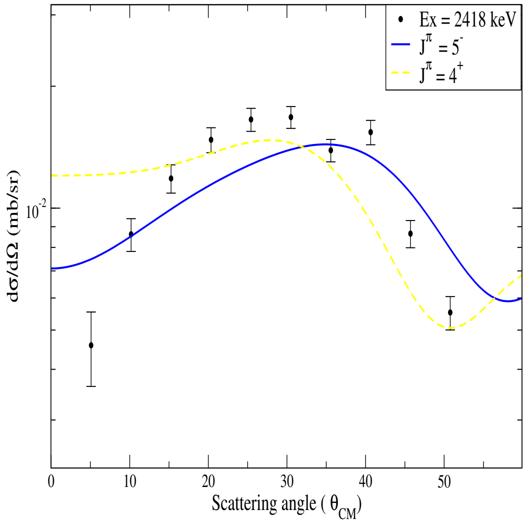
Ex = 2418 keV
J^π = 5^-
J^π = 4^+
dσ/dΩ (mb/sr)
10^-2
0
10
20
30
40
50
Scattering angle (θ_CM)

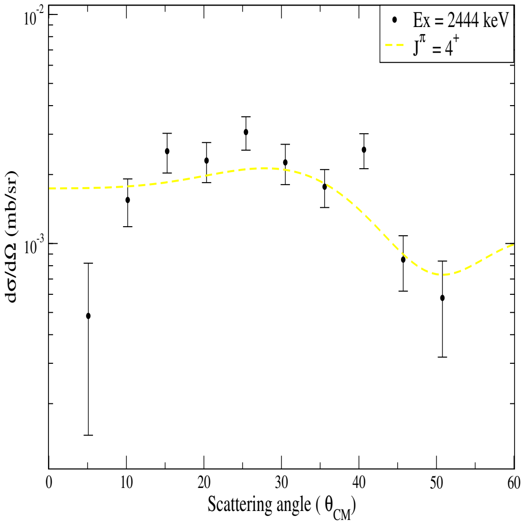
Ex = 2444 keV
J^π = 4^+
dσ/dΩ (mb/sr)
10^-2
10^-3
0
10
20
30
40
50
60
Scattering angle (θ_CM)

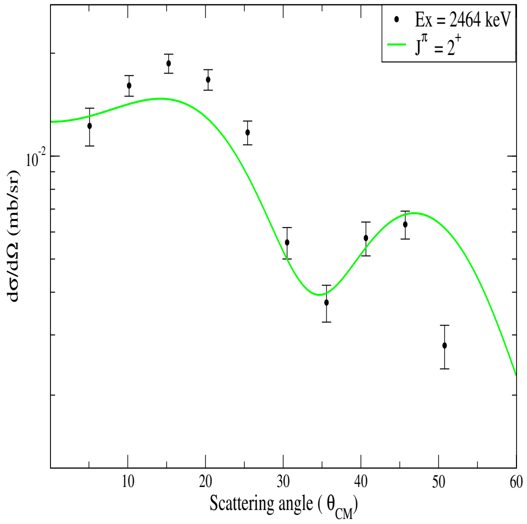

Ex = 2464 keV
J$^{\pi}$ = 2^{+}
dσ/dΩ (mb/sr)
10^{-2}
10
20
30
40
50
60
Scattering angle (θ$_{CM}$)

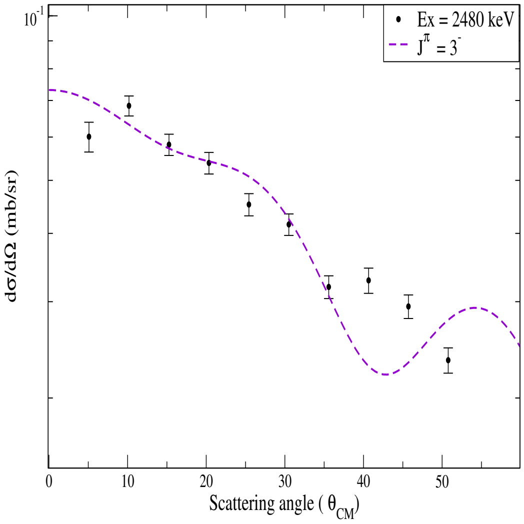

Ex = 2480 keV
J$^{\pi}$ = 3^{-}
dσ/dΩ (mb/sr)
10^{-1}
0
10
20
30
40
50
Scattering angle (θ$_{CM}$)

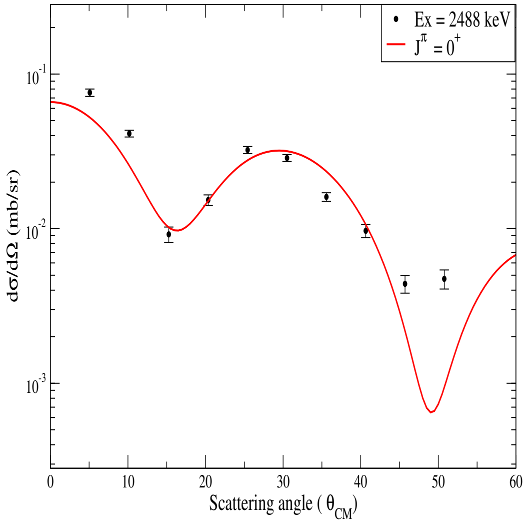

Ex = 2488 keV
J$^{\pi}$ = 0^{+}
dσ/dΩ (mb/sr)
10^{-1}
10^{-2}
10^{-3}
0
10
20
30
40
50
60
Scattering angle (θ$_{CM}$)

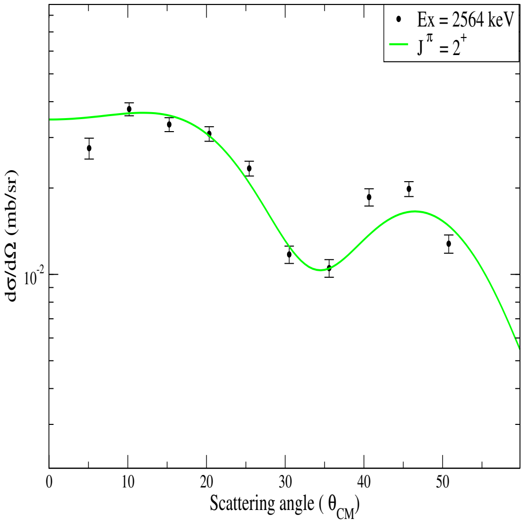

Ex = 2564 keV
J$^{\pi}$ = 2^{+}
dσ/dΩ (mb/sr)
10^{-2}
0
10
20
30
40
50
Scattering angle (θ$_{CM}$)

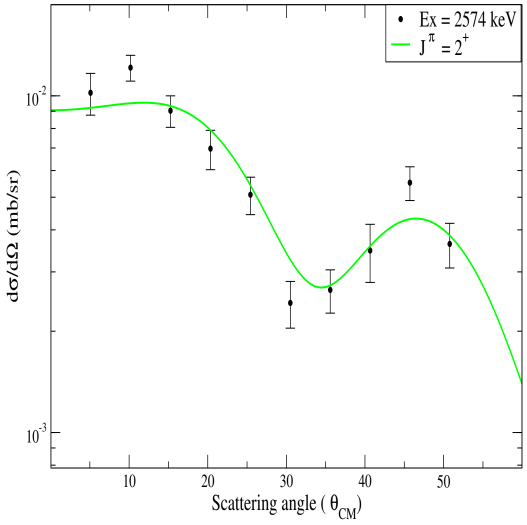

Ex = 2574 keV
J$^{\pi}$ = 2^{+}
dσ/dΩ (mb/sr)
10^{-2}
10^{-3}
10
20
30
40
50
Scattering angle (θ$_{CM}$)

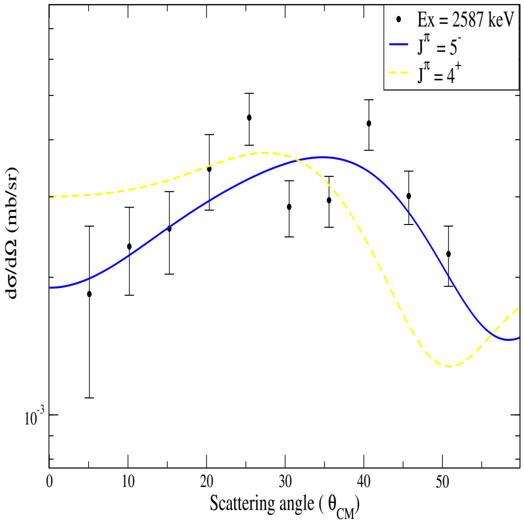

Ex = 2587 keV
J$^{\pi}$ = 5^{-}
J$^{\pi}$ = 4^{+}
dσ/dΩ (mb/sr)
10^{-3}
0
10
20
30
40
50
Scattering angle (θ$_{CM}$)

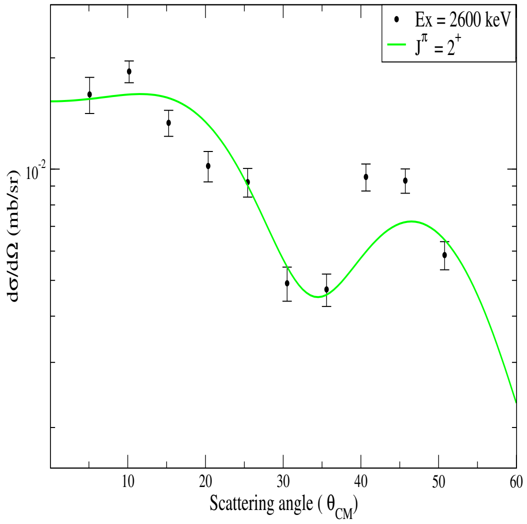
Ex = 2600 keV
$J^{\pi} = 2^{+}$
dσ/dΩ (mb/sr)
10^{-2}
10
20
30
40
50
60
Scattering angle (θ_{CM})

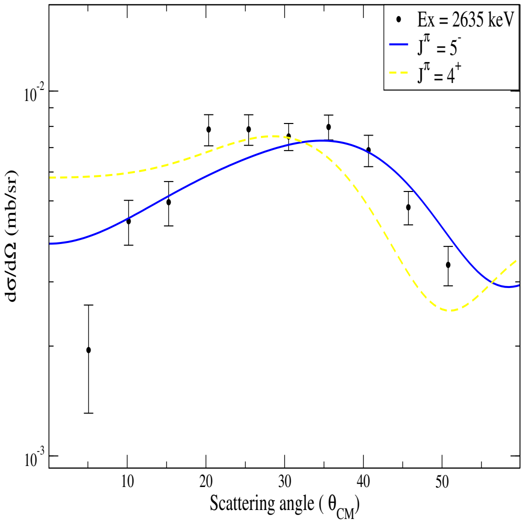
Ex = 2635 keV
$J^{\pi} = 5^{-}$
$J^{\pi} = 4^{+}$
dσ/dΩ (mb/sr)
10^{-2}
10^{-3}
10
20
30
40
50
Scattering angle (θ_{CM})

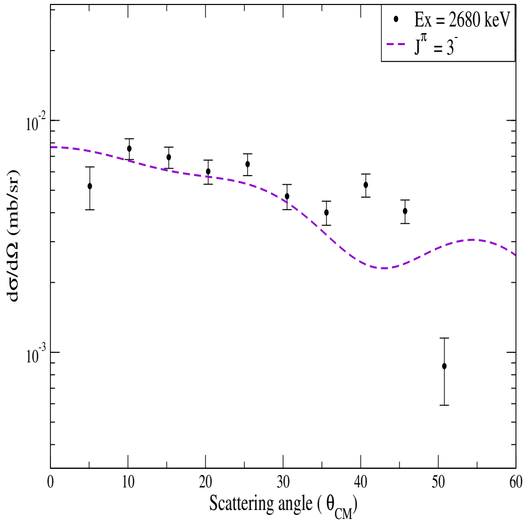
Ex = 2680 keV
$J^{\pi} = 3^{-}$
dσ/dΩ (mb/sr)
10^{-2}
10^{-3}
0
10
20
30
40
50
60
Scattering angle (θ_{CM})

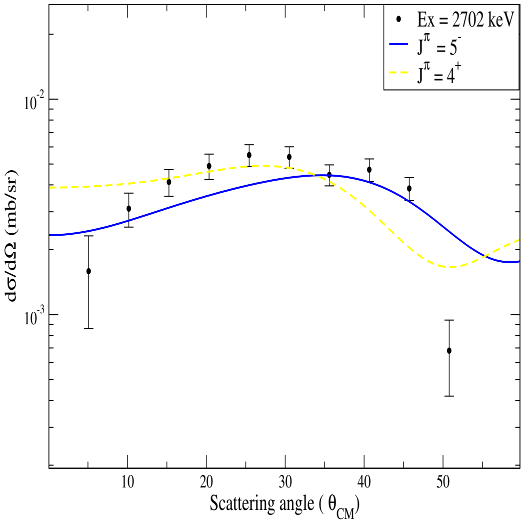
Ex = 2702 keV
$J^{\pi} = 5^{-}$
$J^{\pi} = 4^{+}$
dσ/dΩ (mb/sr)
10^{-2}
10^{-3}
10
20
30
40
50
Scattering angle (θ_{CM})

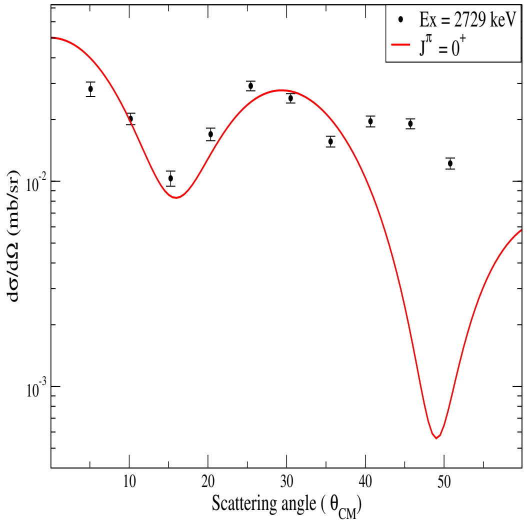
Ex = 2729 keV
$J^{\pi} = 0^{+}$
dσ/dΩ (mb/sr)
10^{-2}
10^{-3}
10
20
30
40
50
Scattering angle (θ_{CM})

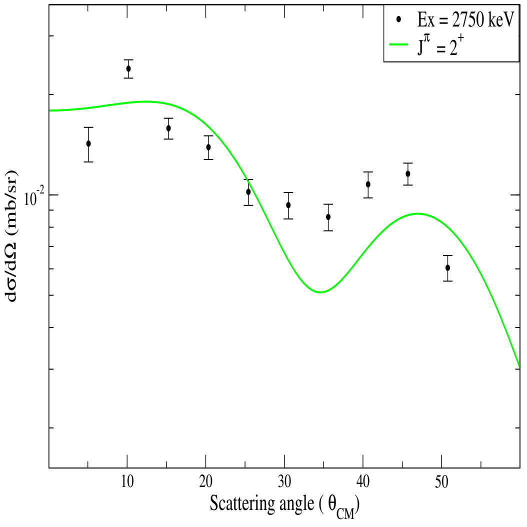
Ex = 2750 keV
$J^{\pi} = 2^{+}$
dσ/dΩ (mb/sr)
10^{-2}
10
20
30
40
50
Scattering angle (θ_{CM})

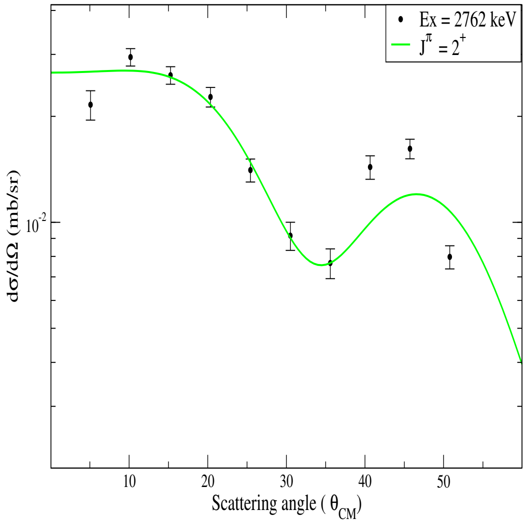
• Ex = 2762 keV
$J^\pi = 2^+$
dσ/dΩ (mb/sr)
10^{-2}
10
20
30
40
50
Scattering angle (θ_{CM})

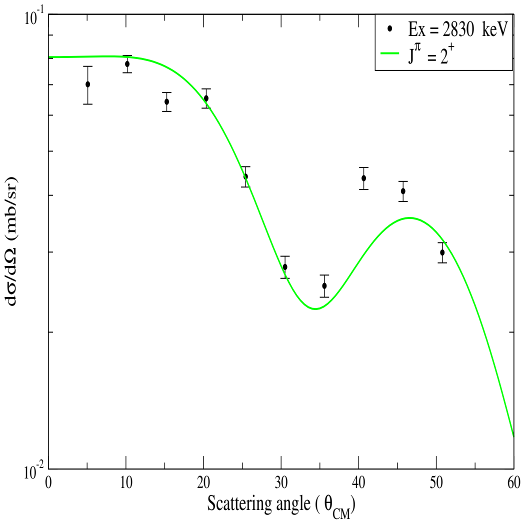
• Ex = 2830 keV
$J^\pi = 2^+$
dσ/dΩ (mb/sr)
10^{-1}
10^{-2}
0
10
20
30
40
50
60
Scattering angle (θ_{CM})

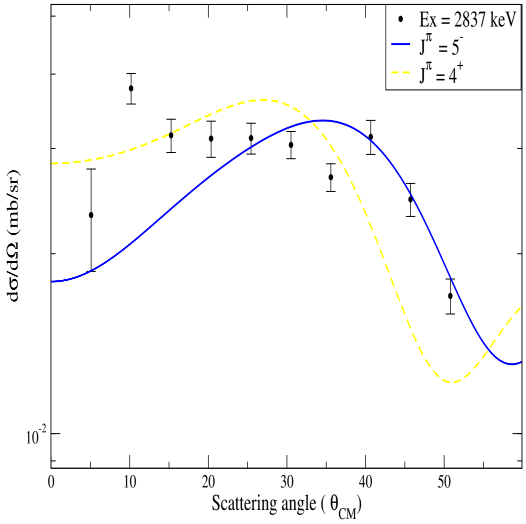
• Ex = 2837 keV
$J^\pi = 5^-$
$J^\pi = 4^+$
dσ/dΩ (mb/sr)
10^{-2}
0
10
20
30
40
50
Scattering angle (θ_{CM})

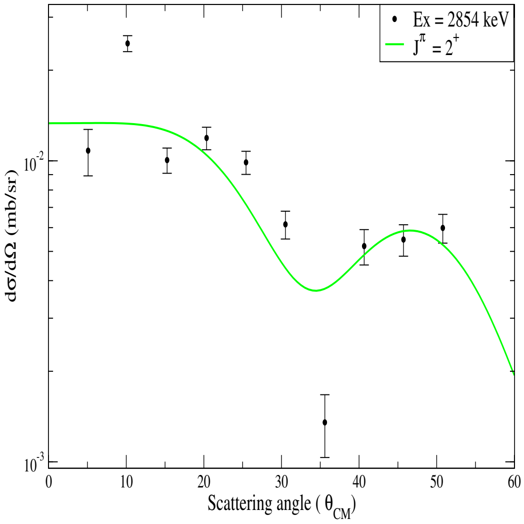
• Ex = 2854 keV
$J^\pi = 2^+$
dσ/dΩ (mb/sr)
10^{-2}
10^{-3}
0
10
20
30
40
50
60
Scattering angle (θ_{CM})

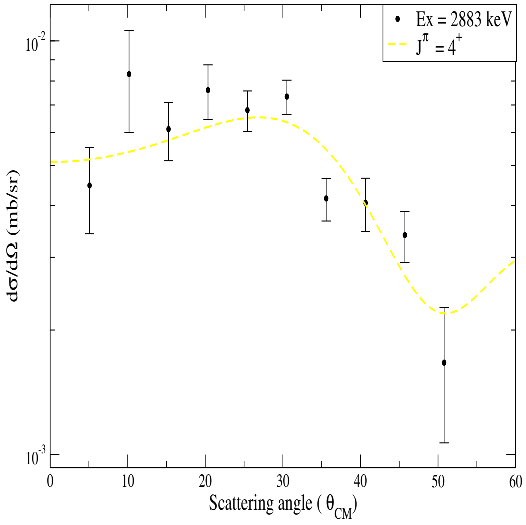
• Ex = 2883 keV
$J^\pi = 4^+$
dσ/dΩ (mb/sr)
10^{-2}
10^{-3}
0
10
20
30
40
50
60
Scattering angle (θ_{CM})

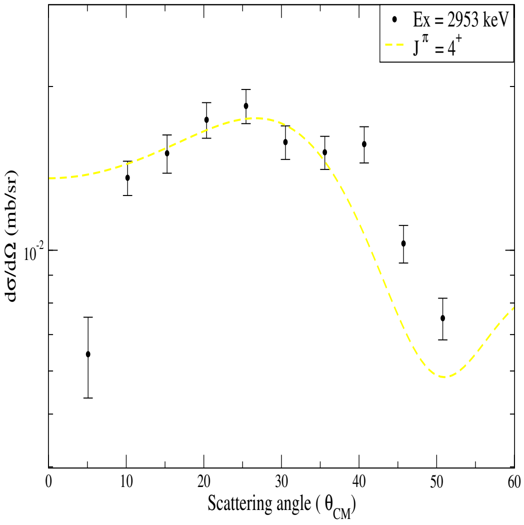
• Ex = 2953 keV
$J^\pi = 4^+$
dσ/dΩ (mb/sr)
10^{-2}
0
10
20
30
40
50
60
Scattering angle (θ_{CM})

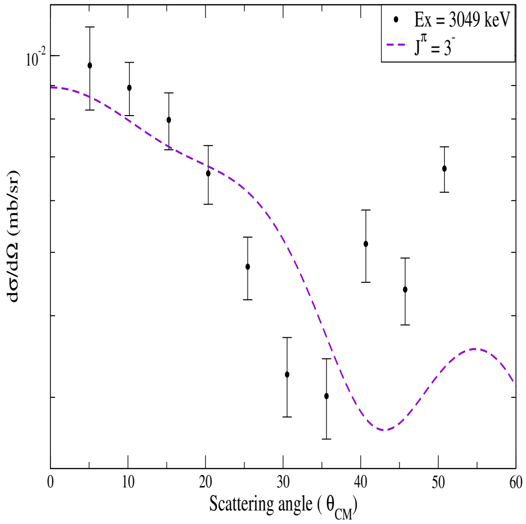

Ex = 3049 keV
$J^{\pi} = 3^{-}$
10^{-2}
dσ/dΩ (mb/sr)
0
10
20
30
40
50
60
Scattering angle (θ_{CM})

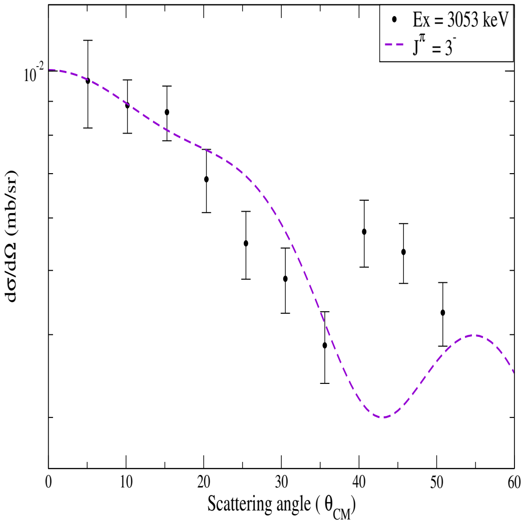

Ex = 3053 keV
$J^{\pi} = 3^{-}$
10^{-2}
dσ/dΩ (mb/sr)
0
10
20
30
40
50
60
Scattering angle (θ_{CM})

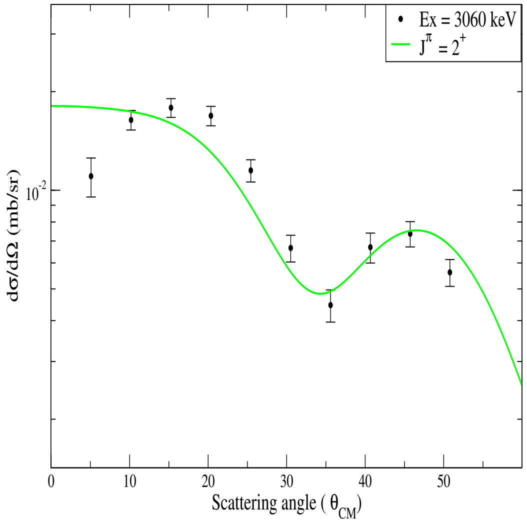

Ex = 3060 keV
$J^{\pi} = 2^{+}$
10^{-2}
dσ/dΩ (mb/sr)
0
10
20
30
40
50
Scattering angle (θ_{CM})

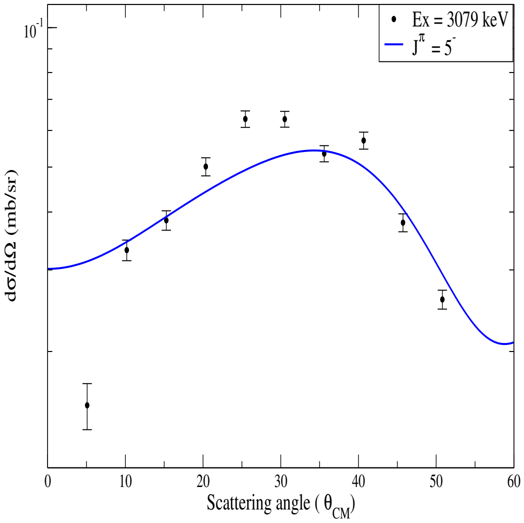

Ex = 3079 keV
$J^{\pi} = 5^{-}$
10^{-1}
dσ/dΩ (mb/sr)
0
10
20
30
40
50
60
Scattering angle (θ_{CM})

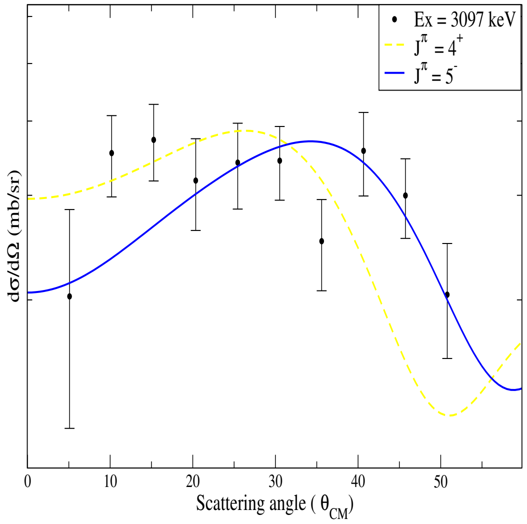

Ex = 3097 keV
$J^{\pi} = 4^{+}$
$J^{\pi} = 5^{-}$
dσ/dΩ (mb/sr)
0
10
20
30
40
50
Scattering angle (θ_{CM})

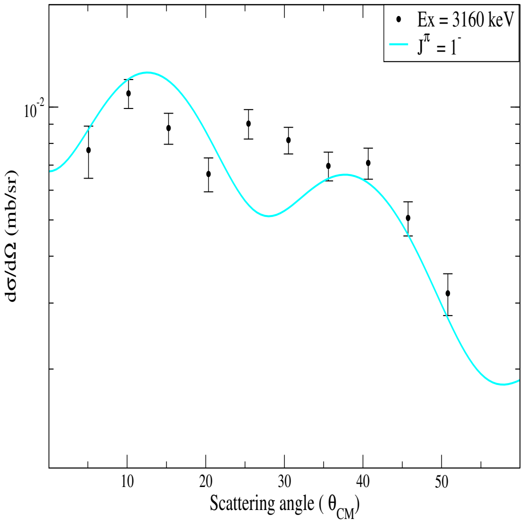

Ex = 3160 keV
$J^{\pi} = 1^{-}$
10^{-2}
dσ/dΩ (mb/sr)
10
20
30
40
50
Scattering angle (θ_{CM})

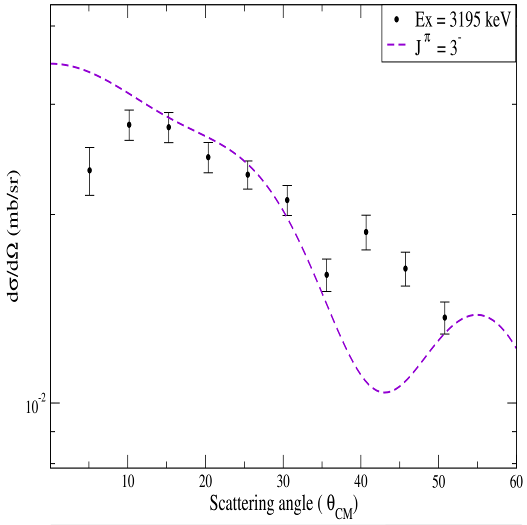
Ex = 3195 keV
J$^\pi$ = 3$^-$
10^{-2}
dσ/dΩ (mb/sr)
10
20
30
40
50
60
Scattering angle (θ$_{CM}$)

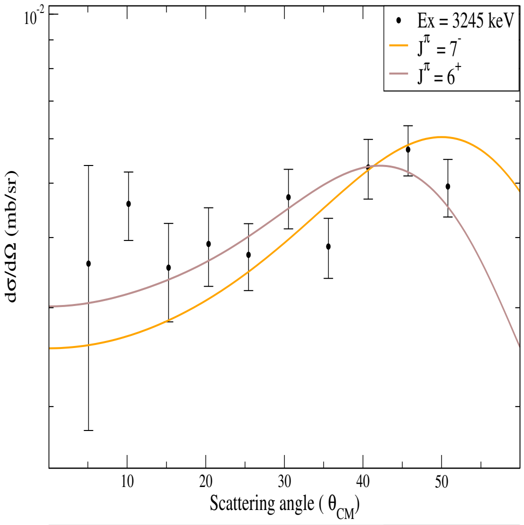
10^{-2}
Ex = 3245 keV
J$^\pi$ = 7$^-$
J$^\pi$ = 6$^+$
dσ/dΩ (mb/sr)
10
20
30
40
50
Scattering angle (θ$_{CM}$)

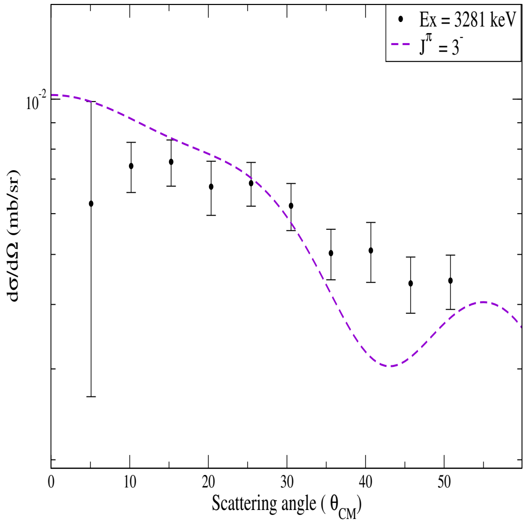
Ex = 3281 keV
J$^\pi$ = 3$^-$
10^{-2}
dσ/dΩ (mb/sr)
0
10
20
30
40
50
Scattering angle (θ$_{CM}$)

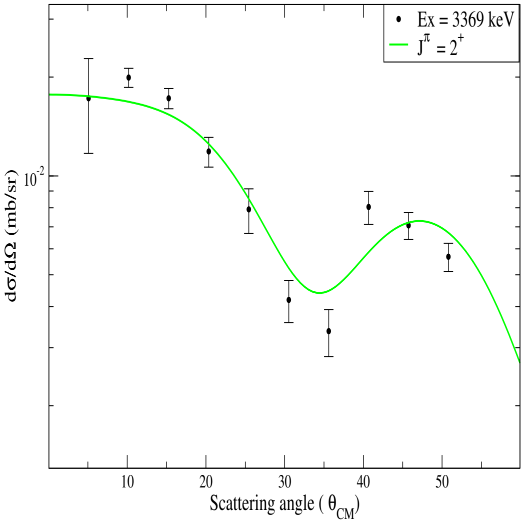
Ex = 3369 keV
J$^\pi$ = 2$^+$
10^{-2}
dσ/dΩ (mb/sr)
10
20
30
40
50
Scattering angle (θ$_{CM}$)

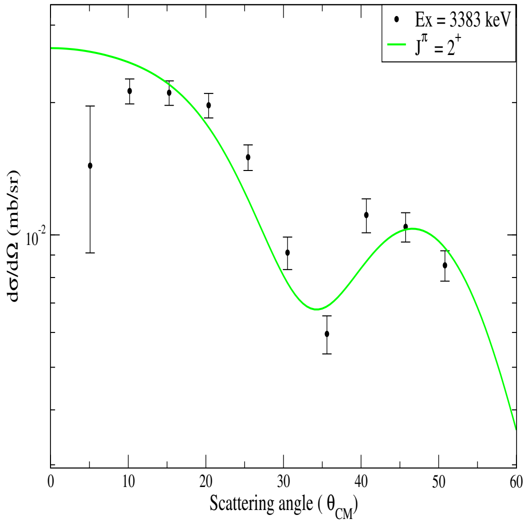
Ex = 3383 keV
J$^\pi$ = 2$^+$
10^{-2}
dσ/dΩ (mb/sr)
0
10
20
30
40
50
60
Scattering angle (θ$_{CM}$)

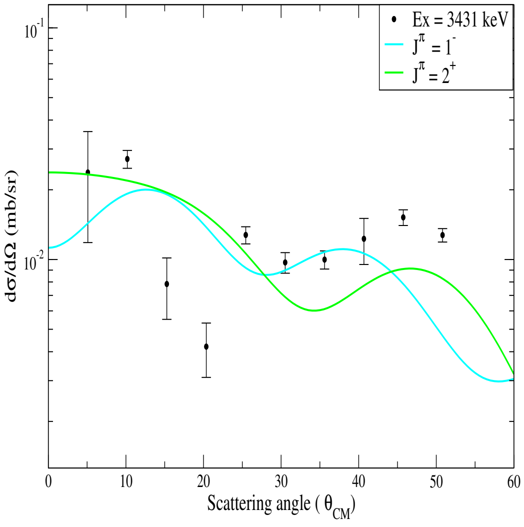
10^{-1}
Ex = 3431 keV
J$^\pi$ = 1$^-$
J$^\pi$ = 2$^+$
10^{-2}
dσ/dΩ (mb/sr)
0
10
20
30
40
50
60
Scattering angle (θ$_{CM}$)

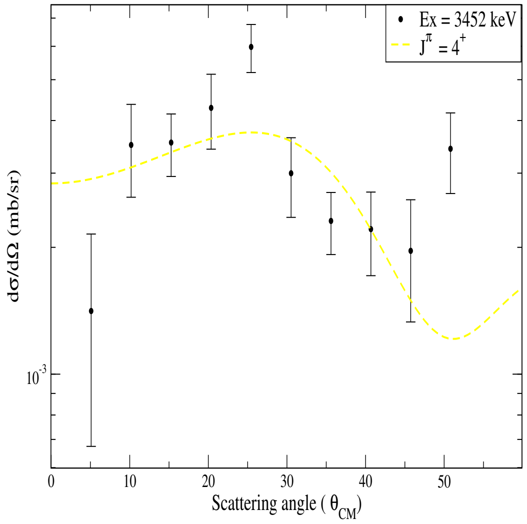
Ex = 3452 keV
$J^{\pi} = 4^{+}$
dσ/dΩ (mb/sr)
10^{-3}
0
10
20
30
40
50
Scattering angle (θ_{CM})

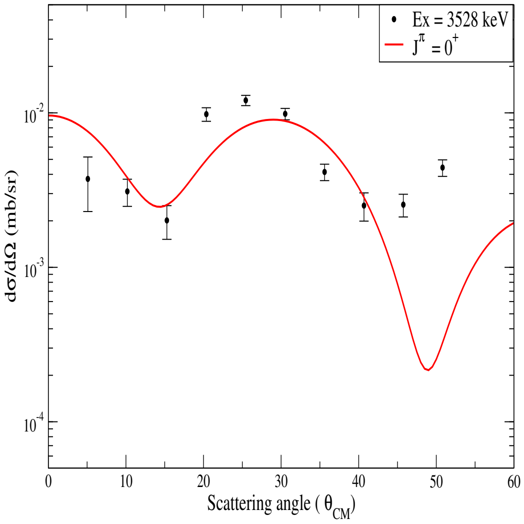
Ex = 3528 keV
$J^{\pi} = 0^{+}$
dσ/dΩ (mb/sr)
10^{-2}
10^{-3}
10^{-4}
0
10
20
30
40
50
60
Scattering angle (θ_{CM})

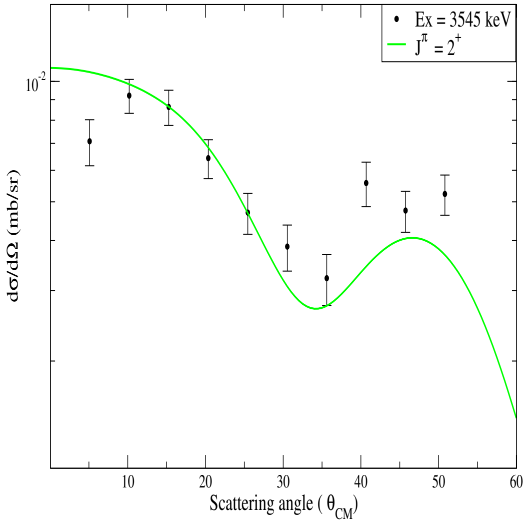
Ex = 3545 keV
$J^{\pi} = 2^{+}$
dσ/dΩ (mb/sr)
10^{-2}
10
20
30
40
50
60
Scattering angle (θ_{CM})

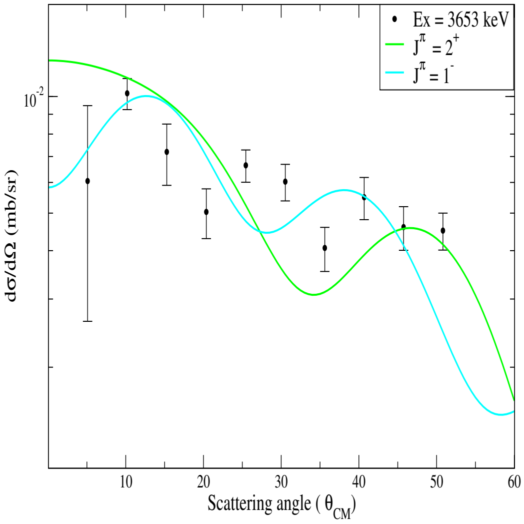
Ex = 3653 keV
$J^{\pi} = 2^{+}$
$J^{\pi} = 1^{-}$
dσ/dΩ (mb/sr)
10^{-2}
10
20
30
40
50
60
Scattering angle (θ_{CM})

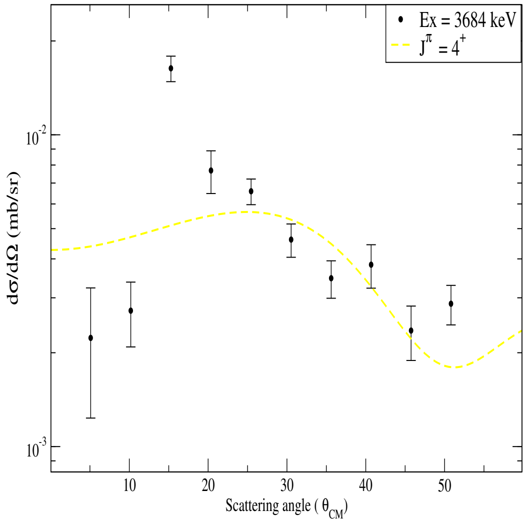
Ex = 3684 keV
$J^{\pi} = 4^{+}$
dσ/dΩ (mb/sr)
10^{-2}
10^{-3}
10
20
30
40
50
Scattering angle (θ_{CM})

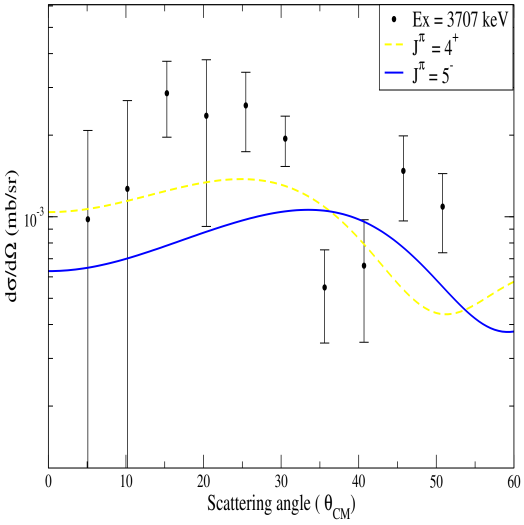
Ex = 3707 keV
$J^{\pi} = 4^{+}$
$J^{\pi} = 5^{-}$
dσ/dΩ (mb/sr)
10^{-3}
0
10
20
30
40
50
60
Scattering angle (θ_{CM})

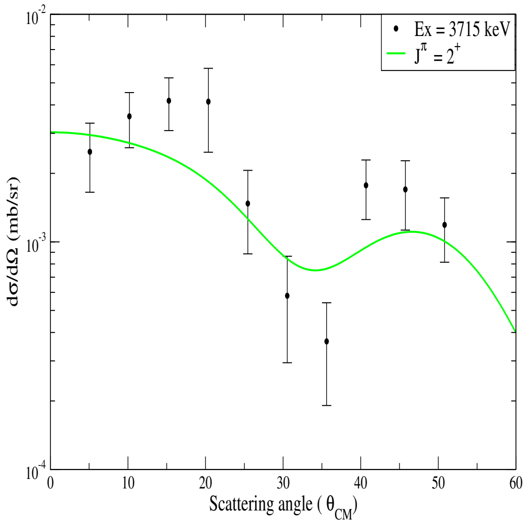
Ex = 3715 keV
$J^{\pi} = 2^{+}$
dσ/dΩ (mb/sr)
10^{-2}
10^{-3}
10^{-4}
0
10
20
30
40
50
60
Scattering angle (θ_{CM})

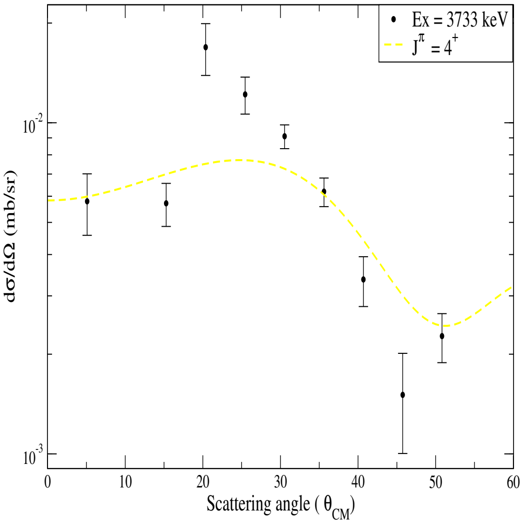
Ex = 3733 keV
$J^{\pi} = 4^{+}$
dσ/dΩ (mb/sr)
10^{-2}
10^{-3}
0
10
20
30
40
50
60
Scattering angle (θ_{CM})

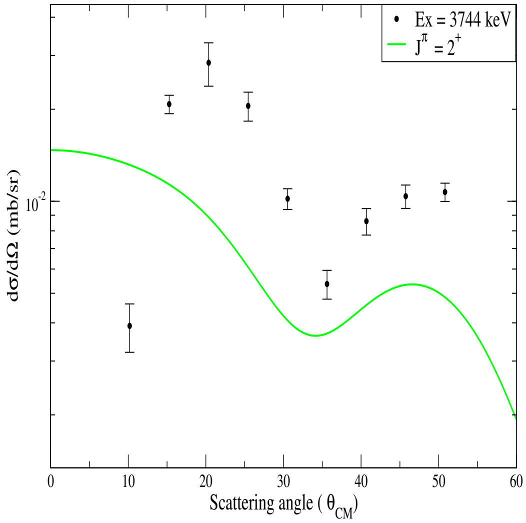
Ex = 3744 keV
$J^{\pi} = 2^{+}$
dσ/dΩ (mb/sr)
10^{-2}
0
10
20
30
40
50
60
Scattering angle (θ_{CM})

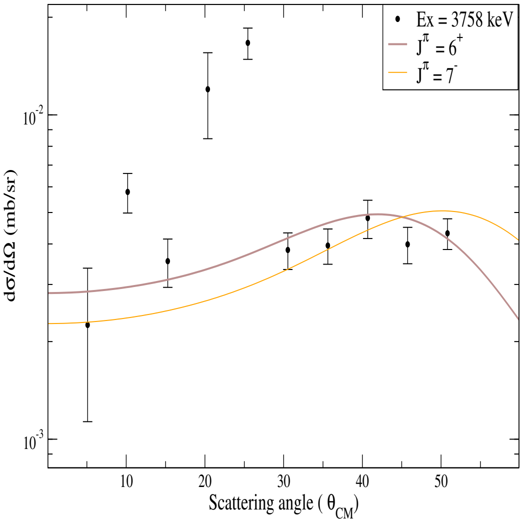
Ex = 3758 keV
$J^{\pi} = 6^{+}$
$J^{\pi} = 7^{-}$
dσ/dΩ (mb/sr)
10^{-2}
10^{-3}
10
20
30
40
50
Scattering angle (θ_{CM})

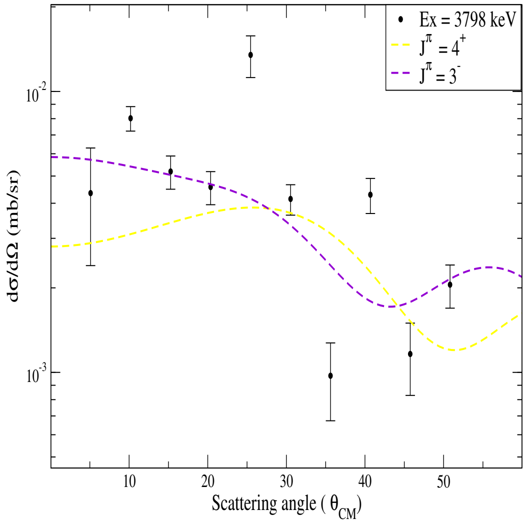
Ex = 3798 keV
$J^{\pi} = 4^{+}$
$J^{\pi} = 3^{-}$
dσ/dΩ (mb/sr)
10^{-2}
10^{-3}
10
20
30
40
50
Scattering angle (θ_{CM})

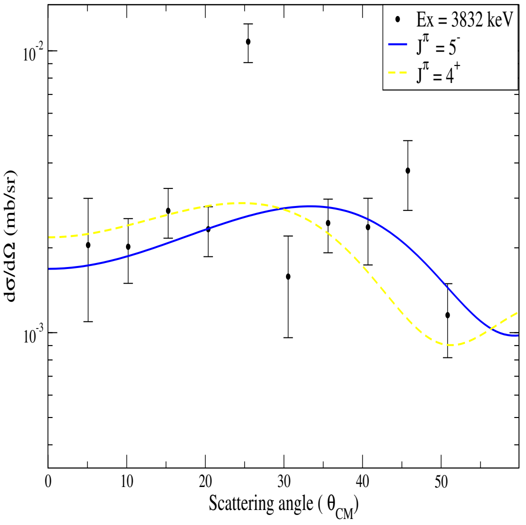
Ex = 3832 keV
$J^{\pi} = 5^{-}$
$J^{\pi} = 4^{+}$
dσ/dΩ (mb/sr)
10^{-2}
10^{-3}
0
10
20
30
40
50
Scattering angle (θ_{CM})

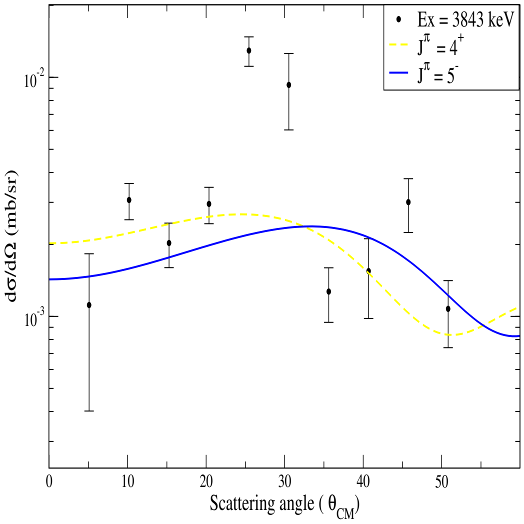
Ex = 3843 keV
$J^{\pi} = 4^{+}$
$J^{\pi} = 5^{-}$
10^{-2}
10^{-3}
dσ/dΩ (mb/sr)
0
10
20
30
40
50
Scattering angle (θ_{CM})

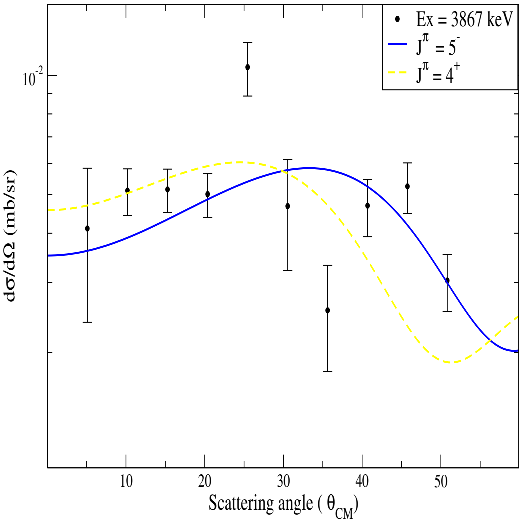
Ex = 3867 keV
$J^{\pi} = 5^{-}$
$J^{\pi} = 4^{+}$
10^{-2}
dσ/dΩ (mb/sr)
10
20
30
40
50
Scattering angle (θ_{CM})

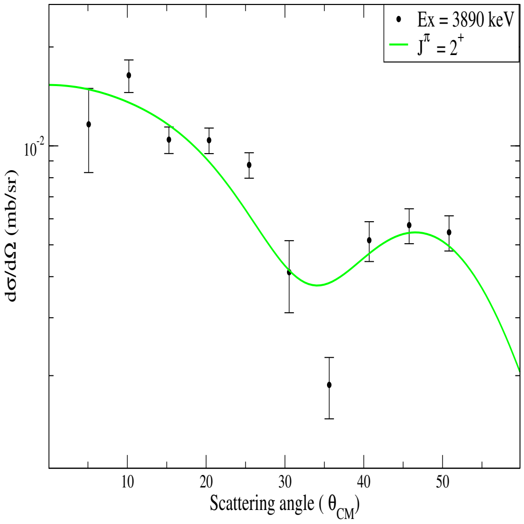
Ex = 3890 keV
$J^{\pi} = 2^{+}$
10^{-2}
dσ/dΩ (mb/sr)
10
20
30
40
50
Scattering angle (θ_{CM})

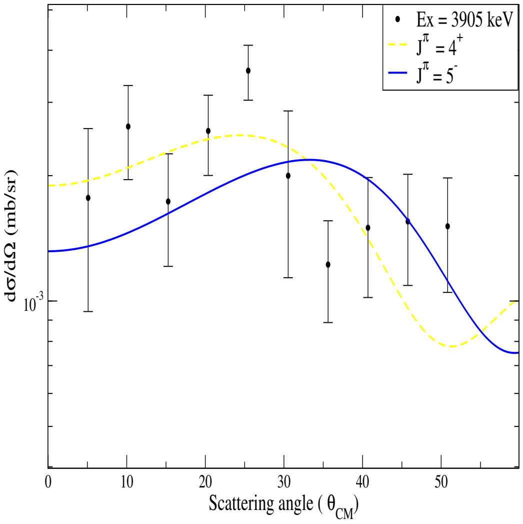
Ex = 3905 keV
$J^{\pi} = 4^{+}$
$J^{\pi} = 5^{-}$
10^{-3}
dσ/dΩ (mb/sr)
0
10
20
30
40
50
Scattering angle (θ_{CM})

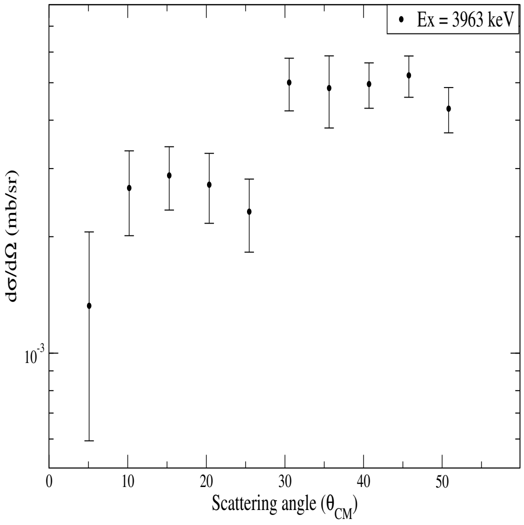
Ex = 3963 keV
10^{-3}
dσ/dΩ (mb/sr)
0
10
20
30
40
50
Scattering angle (θ_{CM})

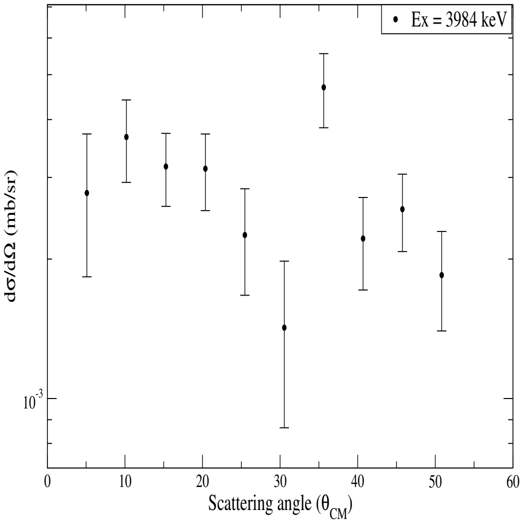
Ex = 3984 keV
10^{-3}
dσ/dΩ (mb/sr)
0
10
20
30
40
50
60
Scattering angle (θ_{CM})

Bibliography

[1] D. Griffiths. *Introduction to Elementary Particles*. John Wiley & Sons, 1987.

[2] `www.t2k-experiment.org/neutrinos/in-the-standard-model/`.

[3] E. M. Henley and A. Garcia. *Subatomic Physics, 3rd Edition*. World Scientific Publishing, 2007.

[4] `www.physics.stackexchange.com/questions/462674/spectrum-of-beta-decay`.

[5] Bahcall, N. John. Solar Neutrinos. I. Theoretical. *Phys. Rev. Lett.*, 12:300–302, Mar 1964.

[6] Davis, Raymond. Solar Neutrinos. II. Experimental. *Phys. Rev. Lett.*, 12:303–305, Mar 1964.

[7] F. Reines, H. S. Gurr, and H. W. Sobel. Detection of $\overline{\nu}_e - e$ scattering. *Phys. Rev. Lett.*, 37:315–318, Aug 1976.

[8] T. D. Lee and C. N. Yang. Question of parity conservation in weak interactions. *Phys. Rev.*, 104:254–258, Oct 1956.

[9] C. S. Wu, E. Ambler, R. W. Hayward, D. D. Hoppes, and R. P. Hudson. Experimental test of parity conservation in beta decay. *Phys. Rev.*, 105:1413–1415, Feb 1957.

[10] `www.aps.org/publications/apsnews/200112/history.cfm`.

[11] W. Greiner & B. Muller. *Gauge Theory of Weak Interactions*. Springer Heidelberg Dordrecht London New York, 1989.

[12] S. Bilenky. *Introduction to the Physic of Massive and Mixed Neutrinos,Lect. Notes Phys. 817*. Springer, Berlin Heidelberg, 2010.

[13] Y. Fukuda and (Super-Kamiokande Collaboration). Evidence for oscillation of atmospheric neutrinos. *Phys. Rev. Lett.*, 81:1562–1567, Aug 1998.

[14] A. McDonald. Evidence for Neutrino Oscillations I: Solar and Reactor Neutrinos. *Nuclear Physics A*, 751:53–66, 2005.

[15] Bahcall, N. John. Gallium solar neutrino experiments: Absorption cross sections, neutrino spectra, and predicted event rates. *Phys. Rev. C*, 56:3391–3409, Dec 1997.

[16] `www.hindawi.com/journals/ahep/2014/191960/`.

[17] P. Vogel. Nuclear structure and double beta decay. *Journal of Physics G: Nuclear and Particle Physics*, 39(12):124002, Nov 2012.

[18] F. Šimkovic, A. Faessler, V. Rodin, P. Vogel, J. Engel. Anatomy of the $0\nu\beta\beta$ nuclear matrix elements. *Phys. Rev. C*, 77:045503, Apr 2008.

[19] E. Caurier, J. Menéndez, F. Nowacki, and A. Poves. Influence of pairing on the nuclear matrix elements of the neutrinoless $\beta\beta$ decays. *Phys. Rev. Lett.*, 100:052503, Feb 2008.

[20] P. K. Rath, R. Chandra, K. Chaturvedi, P. K. Raina, and J. G. Hirsch. Uncertainties in nuclear transition matrix elements for neutrinoless $\beta\beta$ decay within the projected-Hartree-Fock-Bogoliubov model. *Phys. Rev. C*, 82:064310, Dec 2010.

[21] J. Barea and F. Iachello. Neutrinoless double-β decay in the microscopic interacting boson model. *Phys. Rev. C*, 79:044301, Apr 2009.

[22] R. Tomás and G. Martínez-Pinedo. Energy density functional study of nuclear matrix elements for neutrinoless $\beta\beta$ decay. *Phys. Rev. Lett.*, 105:252503, Dec 2010.

[23] J. Engel and M. Javier. Status and future of nuclear matrix elements for neutrinoless double-beta decay: a review. *Reports on Progress in Physics*, 80(4):046301, mar 2017.

[24] D. J. Rowe and J. L. Wood. *Fundamentals of Nuclear Models.* World Scientific Publishing, 2010.

[25] `inspirehep.net/record/1123941/plots`.

[26] `www.assignmentpoint.com/science/physics/definition-of-nuclear-shell-model.html`.

[27] H. J. krappe and K. Pomorski. *Theory of Nuclear Fission.* Springer Heidelberg Dordrecht London New York, 2011.

[28] S. Freeman and J. Schiffer. Constraining the $0\nu\beta\beta$ matrix elements by nuclear structure observables. *Journal of Physics G: Nuclear and Particle Physics*, 39, 07 2012.

[29] A. Gando *et al*. Search for Majorana Neutrinos Near the Inverted Mass Hierarchy Region with KamLAND-Zen. *Phys. Rev. Lett.*, 117:082503, Aug 2016.

[30] J. B. Albert *et al*. Search for Majorana neutrinos with the first two years of EXO-200 data. *Nature*, 510:229234, 06 2014.

[31] C. Alduino *et al*. First Results from CUORE: A Search for Lepton Number Violation via $0\nu\beta\beta$ Decay of ^{130}Te. *Phys. Rev. Lett.*, 120:132501, Mar 2018.

[32] C. E. Aalseth *et al*. Search for neutrinoless double-β decay in ^{76}Ge with the majorana demonstrator. *Phys. Rev. Lett.*, 120:132502, Mar 2018.

[33] M. Agostini *et al*. Improved limit on neutrinoless double-β decay of ^{76}Ge from GERDA Phase II. *Phys. Rev. Lett.*, 120:132503, Mar 2018.

[34] O. Azzolini *et al*. First result on the neutrinoless double-β decay of ^{82}Se with cupid-0. *Phys. Rev. Lett.*, 120:232502, Jun 2018.

[35] A. D. McDonald *et al*. Demonstration of Single-Barium-Ion Sensitivity for Neutrinoless Double-Beta Decay Using Single-Molecule Fluorescence Imaging. *Phys. Rev. Lett.*, 120:132504, Mar 2018.

[36] N. Ackerman *et al*. Observation of two-neutrino double-beta decay in ^{136}Xe with the exo-200 detector. *Phys. Rev. Lett.*, 107:212501, Nov 2011.

[37] `warwick.ac.uk/fac/sci/physics/research/epp/exp/detrd/czt/cobra/`.

[38] M Auger *et al.* The EXO-200 detector, part I: detector design and construction. *Journal of Instrumentation*, 7(05):P05010–P05010, May 2012.

[39] J Shirai *et al.* Results and future plans for the KamLAND-Zen experiment. *Journal of Physics: Conference Series*, vol.888, no. 1, p. 012031 2017.

[40] G. R. Satchler. *Itroduction to Nuclear Reactions.Second Edition.* Oak Ridge National Laboratory, Oak Ridge, Tennessee 37831.

[41] I. J. Thompson and F. M. Nunes. *Nuclear Reactions for Astrophysics.* Cambridge University Press, 2009.

[42] N. Austern. *Direct Nuclear Reaction Theories.* Interscience Monographs & texts in Physics and Astronomy, Volume 25.

[43] G. Ray Satchler. Outline of the development of the theory of direct nuclear reactions. *Rev. Mod. Phys.*, 50:1–10, Jan 1978.

[44] P.D. Kunz. *DWUCK4 DWBA Program.* University of Colorado, Unpublished (1978).

[45] R. E. Phillips & S. T. Thornton. *Kinematic calculations in two-body nuclear reactions.* Oak Ridge National Laboratory, U.S. ATOMIC Energy Commission, November 1967.

[46] R. A. Broglia, O. Hansen & C. Riedel. *Two-neutron transfer reactions and pairing model.* Springer US, Boston, MA, 1989.

[47] R. Hertenberger *et al*. *The Stern-Gerlach polarized ion source for the Munich MP-tandem laboratory, a bright source for unpolarized hydrogen and helium ion beams as well.* Nuclear instruments and Methods in Physics Research Section A: Accelerators, Spectrometers, Detectors and Associated Equipement, pp. 266-272, 2005.

[48] H. F. Wirth, H. Angerer, V. Egidy, Y. Eisermann, G. Graw, R. Hertenberger. New Q3D focal plane detector with cathode-strip readout became operational. *Maier-Leibnitz-Laboratorium Jahresbericht*, 71, 2000.

[49] W. T. Vetterling W. H. Press, S. A. Teukolsky and B. P. Flannery. *Numerical Recipes in FORTRAN (2nd Ed.): The Art of Scientific Computing.* New York, NY,USA:Cambridge University Press, 1992.

[50] S. Triambak. *The isobaric multiplet mass equation and ft value of the* $0^+ \rightarrow 0^+$ *Fermi transition in* ^{32}*Ar: two tests of isospin symmetry breaking.* PhD thesis, University of Notre Dame, Indiana, USA, 2007.

[51] Philip R. Bevington & D.Keith Robinson. *Data Reduction and Error Analysis for the Physical Sciences.Third Edition.* McGraw-Hill, 2003.

[52] E. Maguire, L. Heinrich & G. Watt. Hepdata: a repository for high energy physics data.

[53] F. James & M. Winkler. *C++ MINUIT User's Guide* . 2004.

[54] C. Iliadis. *Nuclear Physics of Stars.* WILEY-VCH, 2015.

[55] B. M. Rebeiro. *Nuclear structure studies in the A = 136 region using transfer reactions.* PhD thesis, University of the Western Cape, Soutrh Africa, 2018.

[56] R.L. Varner, W.J. Thompson, T.L. McAbee, E.J. Ludwig, and T.B. Clegg. A global nucleon optical model potential. *Physics Reports*, 201(2):57 – 119, 1991.

[57] F. D. Becchetti and G. W. Greenlees. Nucleon-nucleus optical-model parameters, $A > 40$, E $<$ 50 MeV. *Phys. Rev.*, 182:1190–1209, Jun 1969.

[58] A .J . Koning and J .P . Delaroche. Local and global nucleon optical models from 1 keV to 200 MeV. *Nuclear Physics A*, 713(3):231 – 310, 2003.

[59] J. J. H. Menet, E. E. Gross, J. J. Malanify, and A. Zucker. Total-reaction-cross-section measurements for 30-60-mev protons and the imaginary optical potential. *Phys. Rev. C*, 4:1114–1129, Oct 1971.

[60] G . F. Knoll. *Radiation Detection and Measurement.* John Wiley & Sons, Inc, 2000.

[61] Xiaohua Li, Chuntian Liang, and Chonghai Cai. Global triton optical model potential. *Nuclear Physics A*, 789(1):103 – 113, 2007.

[62] F. Jr. and G .W . Greenlees. *Rept. J.H. Willians Lab*, Univ. Minnesota, 1969.

[63] A. A. Sonzogni. Nuclear Data Sheet for ^{134}Ba . *Nuclear Data Sheet.*, 103, 2004.

[64] M. G. Stewart, R. P. Scharenberg, and M. L. Wiedenbeck. Angular correlation of the gamma rays of ^{134}Ba. *Phys. Rev.*, 99:691–694, Aug 1955.

[65] T. Morek, H. Beuscher, B. Bochev, D. R. Haenni, R. M. Lieder, T. Kutsarova, M. Müller-Veggian, A. Neskakis. Isomeric states in ^{134}Ba. *Zeitschrift für Physik A Atoms and Nuclei*, 298(4):267–271, 1980.

[66] H. Kusakari, K. Kitao, S. Kono, and Y. Ishizaki. Study of even-mass Ba nuclei by the (p, t) reaction. *Nuclear Physics A*, 341(2):206 – 218, 1980.

[67] B. Fazekas, T. Belgya, G. Molnr, . Veres, R.A. Gatenby, S.W. Yates, and T. Otsuka. Level scheme and mixed-symmetry states of ^{134}Ba from in-beam $(n,n'\gamma)$ measurements. *Nuclear Physics A*, 548(2):249 – 270, 1992.

[68] R. C. Greenwood, C. W. Reich, R. G. Helmer, R. J. Gehrke, and R. A. Anderl. ^{134}Ba level scheme as observed in the decay of ^{134}La. *Phys. Rev. C*, 14:1906–1924, Nov 1976.

[69] S. Pascu, G. Căta-Danil, D. Bucurescu, N. Mărginean, C. Müller, N. V. Zamfir, G. Graw, A. Gollwitzer, D. Hofer, and B. D. Valnion. Structure investigation with the (p, t) reaction on ^{132,134}Ba nuclei. *Phys. Rev. C*, 81:014304, Jan 2010.

[70] G. Cata-Danil, D. Bucurescu, L. Trache, A. M. Oros, M. Jaskola, A. Gollwitzer, D. Hofer, S. Deylitz, B. D. Valnion, and G. Graw.

Monopole transfer strength to ^{132,134}Ba in (p,t) reactions and the interacting boson approximation. *Phys. Rev. C*, 54:2059–2062, Oct 1996.

[71] M. Mller-Veggian, H. Beuscher, D.R. Haenni, R.M. Lieder, and A. Neskakis. Study of the level structure in ^{134}Ce. *Nuclear Physics A*, 417(2):189 – 208, 1984.

[72] H. Maser, N. Pietralla, P. von Brentano, R. D. Herzberg, U. Kneissl, J. Margraf, H. H. Pitz, and A. Zilges. Observation of the 1^+ scissors mode in the γ-soft nucleus ^{134}Ba. *Phys. Rev. C*, 54:R2129–R2133, Nov 1996.